CERATO-ULMIN HYDROPHOBIN-COATED AIR BUBBLES AND OIL DROPLETS: STABILITY, SHAPES, AND INTERFACIAL BEHAVIOR

A Dissertation
Presented to
The Academic Faculty

by

Xujun Zhang

In Partial Fulfillment
of the Requirements for the Degree
Doctor of Philosophy in the
School of Materials Science and Engineering

Georgia Institute of Technology
December 2018

CERATO-ULMIN HYDROPHOBIN-COATED AIR BUBBLES AND OIL DROPLETS: STABILITY, SHAPES, AND INTERFACIAL BEHAVIOR

Approved by:

Dr. Paul S. Russo, Advisor
School of Materials Science and Engineering
Georgia Institute of Technology

Dr. Zhiqun Lin
School of Materials Science and Engineering
Georgia Institute of Technology

Dr. Karl I. Jacob
School of Materials Science and Engineering
Georgia Institute of Technology

Dr. Victor Breedveld
School of Chemical and Biomolecular Engineering
Georgia Institute of Technology

Dr. Seung Soon Jang
School of Materials Science and Engineering
Georgia Institute of Technology

Date Approved: October 01, 2018

To my family

ACKNOWLEDGEMENTS

TABLE OF CONTENTS

LIST OF TABLES

LIST OF FIGURES

subtraction of two images taken 8 ms, 80 ms and 240 ms apart in time. The signal due to the particles is now visible from diffuse speckle patterns and has increased. The size of each panel corresponds to 51 μm in the sample.

LIST OF SYMBOLS AND ABBREVIATIONS

AFM	Atomic force microscopy
AIBN	Azobisisobutyonitrile
BSA	Bovine serum albumin
C18	Stearyl alcohol
CD	Circular dichroism
CMC	Critical micelle concentration
CTAB	Cetyltrimethylammonium bromide
CU	*Cerato-ulmin*
DDM	Differential dynamic microscopy
DLS	Dynamic light scattering
HOPG	Highly oriented pyrolytic graphite
MALDI-ToF	Matrix-assisted laser desorption/ionization-Time of Flight
MADLS	Multi-angle dynamic light scattering
MWCNT	Multi-walled carbon nanotube
NMR	Nuclear magnetic resonance
P3HT	Poly(3-hexylthiophene)
PS	Polystyrene
PS/DVB	Poly(styrene/divinylbenzene)
PSLG	Poly(γ-stearyl-L-glutamade)
PTFE	Poly(tetrafluoroethylene)
PVDF	Poly(vinylidene fluoride)
SAXS	Small-angle X-ray scattering

SDS-PAGE	Sodium dodecyl sulfate-polyacrylamide gel electrophoresis
SLS	Static light scattering
SMW	Small molecular weight
TFA	Trifluoroacetic acid
WCA	Water contact angle
D	Diffusion coefficient
D_{app}	Apparent diffusion coefficient
E	Dilatational modulus
E'	Elastic modulus
E''	Viscous modulus
$g^{(2)}(t)$	Intensity correlation function
$g^{(1)}(t)$	Electric field autocorrelation function
k	Boltzmann's constant
λ	Persistence length
γ	Surface tension
η	Solvent viscosity
T	Kelvin temperature
q	Wave vector magnitude
θ	Scattering angle
Γ	Decay rate
R_{CU}	Radius of single CU molecule
N_A	Avogadro's number
$\langle R^2 \rangle$	End-to-end distance
R_h	Hydrodynamic radius

R_g Radius of gyration

δ Phase lag

ΔP Pressure differece

SUMMARY

Hydrophobins are small amphipathic proteins: one side shuns water, the other seeks it. Unlike common amphipathic molecules (e.g., sodium dodecyl sulfate or SDS used in soap), hydrophobins are nearly rigid, thanks to an elaborate disulfide crosslinking network that stabilizes their compact globular structure. Hydrophobins have been called nature's Janus particles, and nature makes them by the ton in mushrooms and other forms of fungi. A particular hydrophobin in our possession, *Cerato-ulmin* or CU, stabilizes cylindrical microbubbles up simple agitation of its dilute suspension or sausage-like oil blobs in the presence of nonpolar solvents. No emulsifier or other polymer is required to trap either air or oil, suggesting that CU provides both emulsification and strength. Air or oil can be trapped directly without a fluid carrier. They are numerous and remain in suspension long enough for facile study. Application of the air pressure over CU aqueous dispersion in a prescribed sequence converts cylindrical bubbles to air-filled tori with ~100 μm outer diameters. Toroid formation is preceded by morphological transitions from cylindrical to spherical bubbles. Bending elastic energy and curvature model are used to explain the existence of toroidal CU bubbles and their stability. The toroidal bubbles may serve as encapsulation and reaction platforms or as delivery vehicles. The amphipathic property allows CU to adsorb to the hydrophilic-hydrophobic interface and the adsorption is irreversible. The resulting CU films at interfaces are rigid with high interfacial modulus. They are about ten times stronger than those formed by traditional surfactant molecules, although the CU-adsorbed squalane-water interface is not as rigid as the air-water interface. Introduction of a competing agent, such as SDS, both disrupts and displaces a preformed

CU film as well as contributes to a mixed surfactant-protein adsorption layer. In addition, differential dynamic microscopy, an alternative to dynamic light scattering, has been validated to measure diffusive dynamics of colloidal particles in fluid. It has been further extended to study local dynamics of CU bubble debris that is under overpressure or explosion in region of interest, as well as particles' dynamics in the toluene-filled CU confined droplet. Potential uses of hydrophobin biofilms include oil spill clean-up, anti-fouling coatings, personal care products, protection of proteins on sensors, textile coatings, and separations.

CHAPTER 1.   HYDROPHOBINS

1.1   General Background

Hydrophobins are small proteins secreted by filamentous fungi. A common example of such fungi is the bottom mushroom, *Agaricus bisporus*. In the early 90s, Wessel et al.[1] found the first hydrophobin gene during the development of highly expressed *Schizophyllum commune*.[2] About 70 hydrophobins have been found to date. Among all hydrophobins, their typical molecular weights are about 8-14 kDa containing around 100 amino acids.[3] Even though hydrophobins have small similarity in the amino acid sequences, they all surprisingly share one unifying feature which is the presence of eight conserved cysteine residues. Hydrophobins are surface active; indeed, they are among the most surface active proteins known. They are globular in shape, containing both hydrophilic and hydrophobic patches in the molecular structures. This Janus-like formation induces them to be amphiphilic and exhibit strong tendency to self-assemble both in solutions and at hydrophilic-hydrophobic interfaces, such as air-water interface and oil-water interface, where they form amphipathic films. Thanks to these characteristics, hydrophobins show the potential to play specific roles in the formation of aerial structures and the development of aerial growth. They help the fungi to survive in and adapt to the environment. Hydrophobins are also related to different surface phenomena. They enable lowering the surface tension, interacting with surfaces and coating the surfaces. These

properties give them with great potential for a wide range of applications. A few examples are anti-fouling, foams, emulsions, sensors and detectors.[4-6]

1.2   Biological Roles

Hydrophobins are known to play a specific role in a broad range of processes in the formation of the aerial structure of fungi and the development of aerial growth (Figure 1.1).[3] Generally the processes involve the following steps. In nature, the hydrophobin proteins are released into the surroundings of the growing, submerged hyphae and diffuse into the aqueous environment. They are then free to accumulate as monomers or in some cases dimers or tetramers. These small units tend to accumulate at the interfaces and form an amphiphilic monolayer through self-assembly. Upon self-assembly at the interface, hydrophobins orient and attach themselves to the hydrophilic cell wall while the hydrophobic sides are exposed to hydrophobic environment. The self-assembled monolayer is efficient in lowering the surface tension of water. The hydrophobin SC3, expressed from *Schizophyllum commune*, reduces the water surface tension from 72 mN/m to as low as 24 mN/m, as reported by Wösten et al.[7] This significant reduction in surface tension caused by the presence of amphiphilic film allows the hyphae to escape from the aqueous environment, breach the medium-air interface and grow into the air. Apart from allowing hyphae to escape from the aqueous environment, hydrophobins play other biological roles. They may act as toxins and/or attach fungal structures to the host surface in pathogenicity or formation of fruit-body and conidia.[3, 8-10]
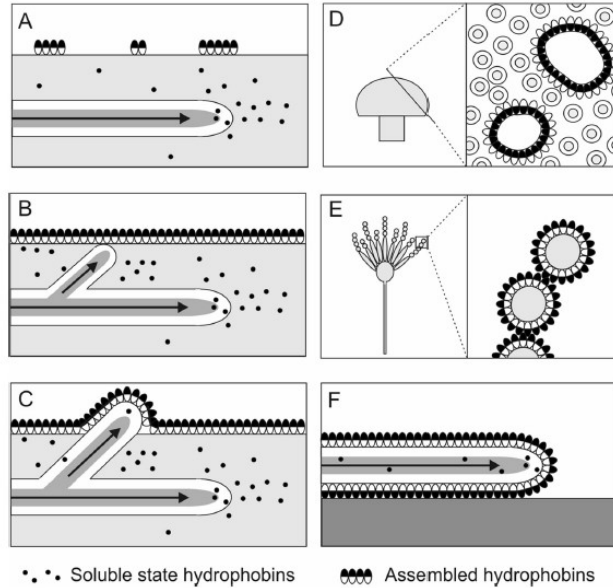
Figure 1.1. Model of the biological role of hydrophobins during growth and development of filamentous fungi.[6] Soluble hydrophobin is secreted at the tip of the growing, submerged hypha and diffuses into the aqueous environment (A). The water surface tension is lowered due to the assembly of hydrophobins into an amphipathic membrane at the medium-air interface (B), allowing the hypha to breach the medium-air interface and grow into the air. The hydrophobin protein molecules secreted by emerging aerial hyphae cannot diffuse into the environment and assemble at the cell wall-air interface (C). Aerial cavities in fruiting bodies are lined with an assembled hydrophobin layer preventing water from filling these cavities (D). Hydrophobins also play a role in the dispersal of spores by coating them with an amphipathic hydrophobin layer (E). Via assembly at the interface between the cell wall and a hydrophobic surface, hydrophobins mediate attachment to the surface, for example, during infection of host tissue (F). (Adapted from reference 6)

1.3   Structures of Hydrophobins

The sequences and structures in molecular level have been elucidated and unlocked by extensive research in the past decades. The primary length of hydrophobin sequences

3

varies from 75 to 125 amino acids. Hydrophobins have shown a very low level of similarity between the amino acid sequences, but one important characteristic feature they all share is eight conserved cysteine residues.[11] Figure 1.3 shows the chemical structure of cysteine amino acid. These eight conserved cysteine residues all occur in a specific order. The second and third cysteine residues follow each other immediately in sequence and create a pair. The sixth and seventh also pair adjacently in the primary structure of hydrophobins.[12] Eight cysteine residues form intramolecular disulfide bridges that is in their secondary structures.
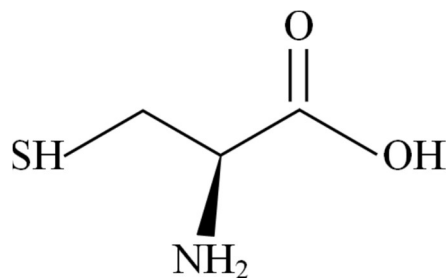
Figure 1.2. Chemical structure of cysteine amino acid.

Hydrophobins are categorized into two classes, Class I and Class II, depending on the hydropathy patterns of the amino acid sequences.[13] The classification appears to be consistent with some properties of hydrophobins, such as the solubility of their self-assemblies. Figure 1.3 shows examples of Class I and Class II hydrophobins, having the

same order of eight cysteine residues and the formation of four intramolecular disulfide bridges. Class I hydrophobins such as SC3 from *Schizophyllum commune* form insoluble aggregates, which can only be dissolved in strong acids such as trifluoroacetic acid or formic acid.[14] In contrast, the assemblies of Class II hydrophobin can be readily dissociated by agents such as ethanol or sodium dodecyl sulfate (SDS). Russo et al. characterized the stability of assembled *Cerato-ulmin* (CU) and found CU to be dissolved in 70% ethanol and in 2% SDS. CU is also known to dissociate through the application of pressure or lowering of temperature.[15] Table 1.1 lists the hydrophobins mentioned in this chapter.
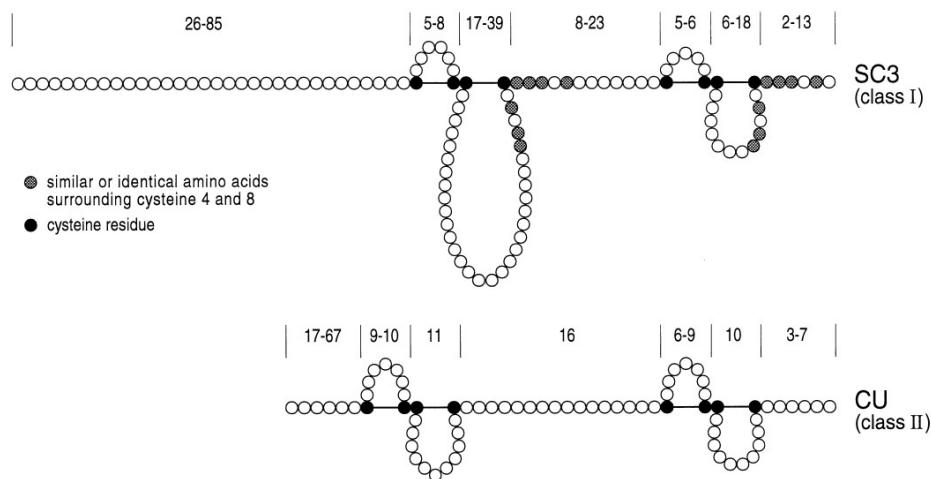
Figure 1.3. Examples of amino acid sequences and disulfide bridges of Class I and Class II hydrophobins.[11]

Table 1.1. Lists of Class I and II hydrophobins mentioned in this chapter.

Gene names	Organism	Hydrophobin Classes
CU	*Ophiostoma ulmi*	II
HFBI	*Trichoderma reesei*	II
HFB II	*Trichoderma reesei*	II
SC3	*Schizophyllum commune*	I
EAS	*Neurospora crassa*	I
DewA	*Aspergillus nidulans*	I
MPG1	*Magnaporthe grisea*	I
RodA	*Aspergillus fumigatus*	I
Vmh2	*Pleurotus ostreatus*	I
ABH1	*Agaricus bisporus*	I
HGF1	*Grifola frondosa*	I
CFT1	*Clayulinopsis fusifomis*	I

It is important to know the three-dimensional structures of hydrophobins in order to better understand their functions. Some important breakthroughs have been made in the past decades. Hakanpää et al.[16] have successfully crystalized a Class II hydrophobin, HFB II from *Trichoderma reesei*, and determined its three-dimensional structure at 1.0 Å resolution.[17] HFB II has a compact single domain structure with the approximate dimensions of 24×27×30 Å. The structure contains one stretched α-helix and four antiparallel β-sheets (S1, S2, S3, and S4) as shown in Figure 1.4A. S1 and S2 β-sheets form

one β-hairpin linked to the α-helix (blue, Figure 1.4A) that is linked to the second β-hairpin (S3 and S4). The four intramolecular disulfide bridges are colored in yellow in Figure 1.4A.

The most notable and unique feature of the HFBII structure is that instead of having hydrophobic residues buried in the core of the protein, about half of all hydrophobic residue in the protein are exposed at the protein surface. This remarkable structure is probably stabilized by the disulfide network mentioned above. This part of the surface consists of hydrophobic aliphatic side chains forming a flat area and it is called the hydrophobic patch shown in Figure 1.4B (green).[18] The rest of HFBII surface is mainly hydrophilic and thus the protein surface is segregated into a hydrophilic and hydrophobic part. This amphiphilic structure has led some writers to describe hydrophobin as Janus particles.[18]
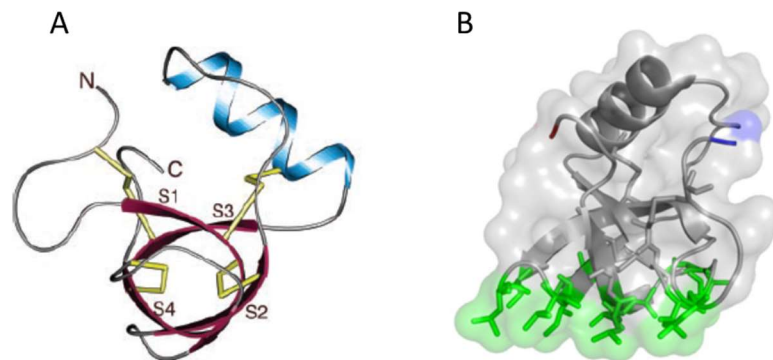
Figure 1.4. Three-dimensional structure of HFBII showing β-barrel and four disulfide bridges in yellow (A). The hydrophobic patch is shown in green, the hydrophilic surface is in grey. N- and C- terminal are colored in blue and red (B). Adapted from references[17-18].

Hydrophobins are normally compared by aligning the amino acid sequences. The amino acid residues that form the hydrophobic patch in HFBII comprises residues Val-18, Leu-19, Leu-21, Ile-22 and Val-24 of the first beta hairpin loop, Ala-55, Val-57, Ala-61, Leu-62 and Leu-63 of the second beta hairpin loop and Leu-7.[12] When comparing the sequence of HFBII to other class II hydrophobins, the residues forming the hydrophobic patch are conserved, that is similar residues are found in the corresponding positions in the other sequences.[18] This suggests they all share a similar amphiphilic protein surface.

A well-studied of the structure of Class I hydrophobin is EAS protein from *Neurospora crassa*. Its structure has been studied by nuclear magnetic resonance (NMR) spectroscopy, reported by Kwan et al.[19] The authors found EAS structure comprises a four-stranded β-barrel with an additional two-stranded antiparallel β-sheet as shown in Figure 1.5A (blue). Two of the four intramolecular disulfide bridges (yellow, Figure 1.5A) exist in the center of the fold, whereas the other two connect the outside of the barrel fold to the additional β-sheet and a loop. In comparison with the structure of the Class II hydrophobin HFBII, both EAS and HFBII have a similar core fold despite the very low level of similarity in amino acid sequence.[19] In addition, the Class I hydrophobin EAS has two large disordered loops (indicated by arrows in Figure 1.5A) which are not seen in Class II HFBII structure. The additional antiparallel β-sheet from outside of the center core in EAS is replaced with an α-helix in HFBII. The superposition of structures of HFBII and EAS is shown in Figure 1.5B.[18-19]
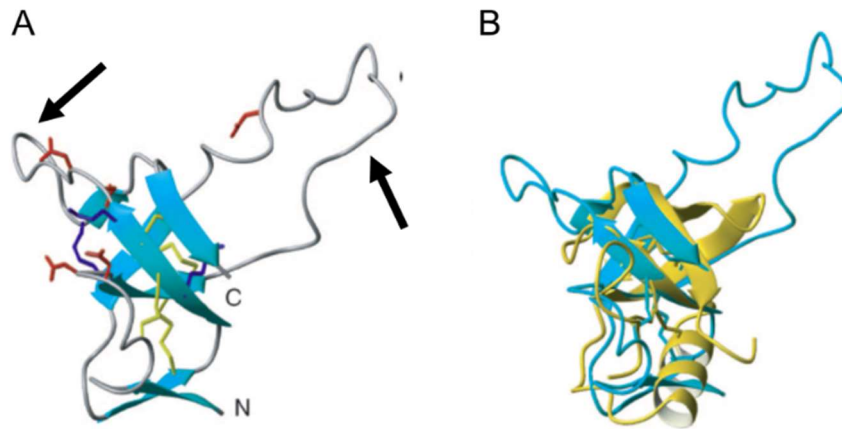
Figure 1.5. Ribbon structure of EAS (A) and a structure overlay of EAS (blue) and HFBII (yellow). [18-19]

The 3D structures of the soluble state of some other Class I and Class II hydrophobins have been explored too. These include SC3 (*Schizophyllum commune*),[20] DewA (*Aspergillus nidulans*),[21] MPG1 (*Magnaporthe grisea*),[22] RodA (*Aspergillus fumigatus*),[23] HFB I (*Trichoderma reesei*),[24] and NC2 (*Neurospora crassa*).[25] In general, both Class I and Class II hydrophobins have a four-stranded β-barrel core and one additional structure, either α-helix or β-sheet (Figure 1.6). The small differences in structures between Class I and Class II hydrophobins may affect their functions or even the way individual hydrophobin molecules pack together.
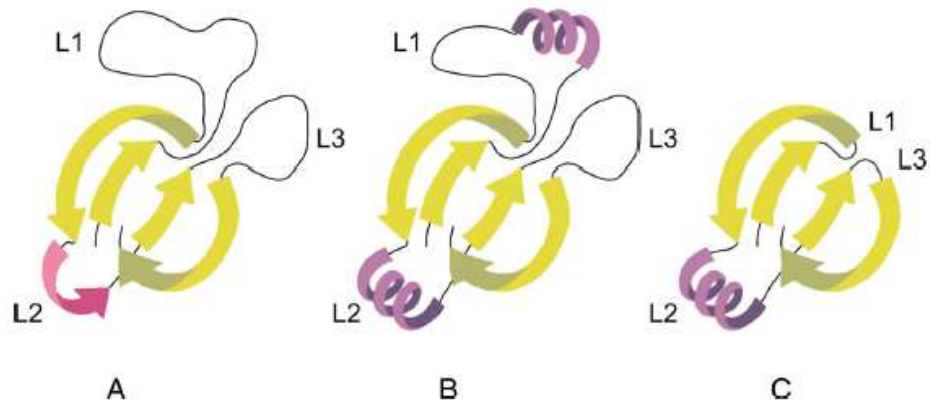
Figure 1.6. Examples of the 3D structures of Class I (A, B) and Class II (C) hydrophobins.[6] Both hydrophobin types contain a four-stranded β-barrel core (A-C, in green) and either an α-helical (B, C) or a β-sheet structure in loop 2 (L2). Loops 1 and 3 are larger in Class I hydrophobins than in Class II hydrophobins.

1.4   Self-assembly of Hydrophobins

1.4.1   In Water

Due to the amphiphilic structure having the hydrophilic and hydrophobic patch on the protein surface, hydrophobins are surface active and self-assemble in aqueous solution. Torkkeli et al. used small-angle X-ray scattering (SAXS) to study the solution state of both Class II hydrophobins HFBI and HFBII.[26] They found HFBI and HFBII have the same radius of gyration of 2.4 nm in monomeric form. The SAXS data also indicated the maximum dimension of assemblies, which is 6.5 nm. This could be corresponding to the size of a tetramer. Kisko et al. and others continued to study the association of HFBI and HFBII in aqueous solution.[17, 27-28] They showed the tetramers of HFBII dissociate more easily than those of HFBI by changing the value of pH from 3 to 9 and by changing the

temperature in the range of 5 – 60 °C. Adding ethanol to the solution can break tetramers into monomers. In the presence of surfactants, such as cetyltrimethylammonium bromide (CTAB) or sodium dodecyl sulfate (SDS), the HFBII binds to the outside surface of surfactant micelles to form complexes.[29] The Class I hydrophobin SC3 was found to exist as a dimer mainly, accompanied with a small amount of monomer and tetramer in solution.[30] Mackay et al. reported another Class I hydrophobin, EAS, which has been proposed to occur as monomers.[31] Monomers, dimers and tetramers are normally formed in aqueous solution through associations of the hydrophobins (Figure 1.7). Other examples are Vmh2 from *Pleurotus ostreatus*,[32] DewA from *Aspergillus nidulans*,[21] ABH1 from *Agaricus bisporus*[33] and recombinant hydrophobins H*Protein B produced by BASF.[34]
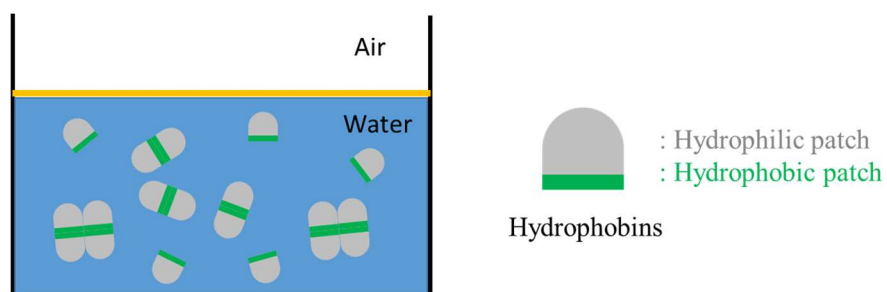
Figure 1.7. Cartoon representations of monomers, dimers, and tetramers of hydrophobins in aqueous solution.

In addition to monomer, dimer and tetramers, large aggregates formed by some hydrophobins are also observed in solution. Takai et al. reported "Rods" and "fibrils" are easily formed under gentle shaking or applying shear force upon mixing.[35] And the *Cerato-ulmin* solution from *Ceratocystis ulmi* appears to be milky. HFBII forms similar needle-like structures.[26] The assembly mechanism inducing formation of large aggregates structures is not known.

1.4.2 At Interfaces

Hydrophobins not only self-assemble to form multimers in aqueous solution, but also form self-assembled monolayer at the hydrophilic-hydrophobic interfaces. The most commonly described structures are observed at the air-water interfaces. The self-assembled structures exhibit distinct features for Class I and Class II hydrophobins. Early studies by Wösten et al.[36] showed the SC3 hydrophobins spontaneously assemble into a membrane on a hydrophilic surface. The dried surface was characterized under electron microscopy and was found to consist of nanometer-sized rods with diameter of 10 nm and length of hundreds of nanometers.[10] These rods packed together in a mosaic pattern, as shown in Figure 1.8. The similar pattern was also observed from another Class I hydrophobin, EAS, as reported by Mackay et al.[31] The form of rodlet layer is also very similar to that of the wild-type spore surface.[37] Gebbink et al.[38] described these rodlets have to do with amyloid fibrils due to the same spectroscopy change when hydrophobins bond to the dyes Thioflavin T and Congo Red.[39] The formation of amyloid fibrils is only limited to Class I hydrophobin.[40]
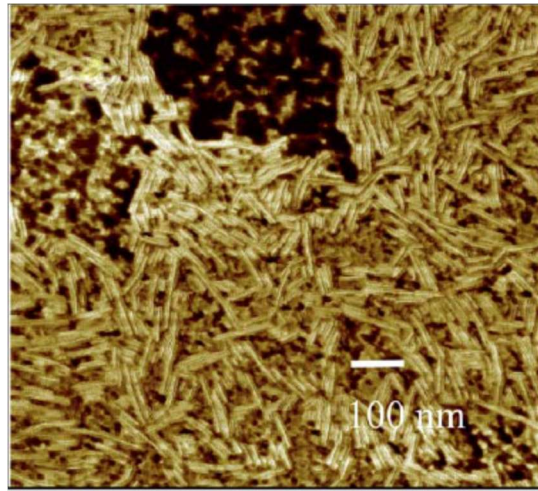
Figure 1.8. An example of rodlet layer of Class I hydrophobin SC3 observed under atomic force microscopy (AFM).[12]

Unlike the rodlet layer seen from Class I hydrophobins, Class II hydrophobins have not been observed to form rodlets. Instead, they exhibit highly organized surface layers at the air-water interface. Mica substrates were covered by Langmuir-Blodgett films of the hydrophobin HFBI.[41] The films showed highly ordered two-dimensional crystalline structures (Figure 1.9). The crystalline domain had a regular arrangement of holes.
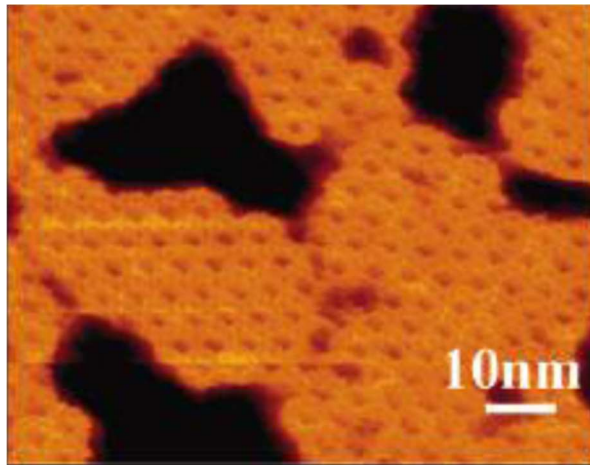
Figure 1.9. An atomic force image of Class II hydrophobin HFBI Langmuir-Blodgett films on mica.[41]

Adsorption and self-assembly of hydrophobins at the water-air, water-oil, and solid-air interfaces are attributed to their amphiphilic feature. Conformational changes are involved. The secondary structure undergoes conformation change during self-assembly (Figure 1.10).[6] Self-assembly of SC3 is accompanied by a conformational change from an α-helical structure to an intermediate β-sheet I state and eventually to a β-sheet II end state.[42] These rodlets resist detergent, ethanol and pressure.[36] In contrast, Class II hydrophobins do not form bundles of rodlets at interfaces. They assemble at the water-air interface with a conformation similar to that in their soluble state. The monolayer formed by Class II thus can be dissociated readily by pressure or detergent.[11, 41]
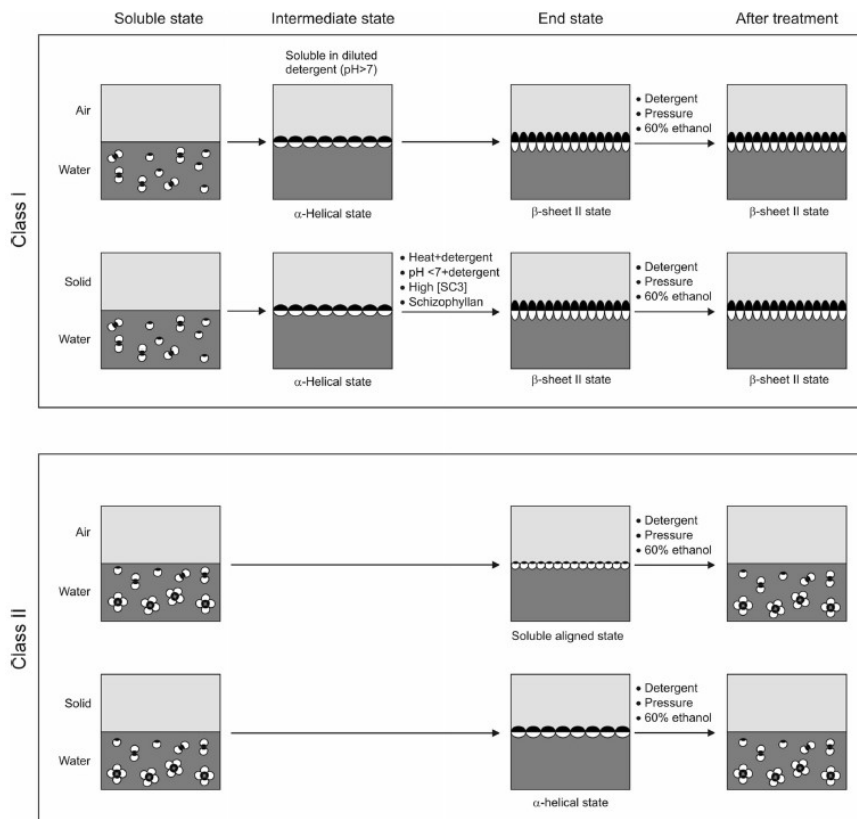
Figure 1.10. Conformational changes of Class I and Class II hydrophobins through self-assembly (adapted from reference 6).

When hydrophobins bind to a solid surface, they can switch its hydrophobicity. A glass surface coated with hydrophobin turns hydrophobic with a 110° water contact angle (WCA),[11, 36] which is similar to that observed on poly(tetrafluoroethylene), PTFE, surfaces. When a PTFE surface is coated with hydrophobin, its water contact angle drops to between 22° and 63°.[11] Binding to polar surface causes significant change in the water contact angle.[43] The highest contact angles were obtained on cationic surfaces where the

15

hydrophobin HFBI, HFBII, and HFBIII have average WCA of 62 - 69° in the range of pH 8 - 9. These profound alterations in water contact angle are driven by surface activity.

1.4.3   Surface Activity of Hydrophobins

Hydrophobins are among the most surface-active protein known.[12] As already mentioned, one important role of hydrophobins is lowering the surface tension of water during the development of aerial growth. In general, proteins the reduce surface tension of water because they have both hydrophilic and hydrophobic residues. The degree of surface tension reduction depends on the types of hydrophobins and their concentrations. As described on Page 2, the Class I hydrophobin SC3 can lower the surface tension from 72 mN/m to 24 - 34 mN/m.[7] The difference in final surface tension is due to the variant conditions, such as liquid composition, concentrations or temperature. CFT1 of *Clavulinopsis fusiformis* has a surface tension of 33.5 mN/m at 0.1 mg/mL.[44] HFBII can reduce the surface tension of water to 28 mN/m at a concentration of 0.02 mg/mL.[45] Russo et al. reported Class II hydrophobin *Cerato-ulmin* shows surface activity at concentrations as low as 30 ng/mL.[15, 46] Traditional small molecular weight surfactants are able to lower the surface tension within seconds, while it takes minutes or hours for hydrophobins. This is because of the conformational change during self-assembly at the interfaces.[3] Another interesting observation is their ability to form and stabilize air bubbles[15, 47] or foams[48] because of surface-active property. Some other examples are air vesicles produced by shaking a solution of SC3 hydrophobin[36] and non-spherical bubble stabilized by HFBI and HFBII hydrophobins.[49]

1.5   Applications

Due to the intriguing properties of hydrophobins, they have shown a wide range of applications, which have been comprehensively reviewed.[4-6, 12, 18, 50-52]

1.5.1 Dispersants

A commercial hydrophobin H*Protein B was used to encapsulate quantum dots and was able to phase transfer quantum dots from organic solvent to water.[53] Further taking advantage of using a biological molecule with available functional groups, the authors explored their use in imaging application, such as imaging cancer cell in vivo. Rosu et al. showed *Cerato-ulmin* dispersion facilitated improved alignment and organization of the semi-conductive polymer poly(3-hexylthiophene) (P3HT) chains into highly ordered crystalline structures in an aqueous suspension process.[54] The authors claimed this opens the door to latex-like processing of semiconducting polymers into crystalline, high-performance thin films for device applications. Other examples of hydrophobins as dispersants include hydrophobin-stabilized dispersion of partially crystalline poly(vinylidene fluoride) (PVDF) nanoparticles in water,[55] and improvement of the incorporation of insoluble flavor compounds in beverages.[56] Single-walled carbon nanotubes coated by the Class I hydrophobin EAS results in a stable dispersion in aqueous solutions.[57] The Class I hydrophobin HGFI from *Grifola frondosa* was used to disperse multi-walled carbon nanotube (MWCNTs) in water. Wang et al. claimed that the HGFI-coated MWCNTs can work as linkers to immobilize target proteins.[58]

1.5.2 Binding and Immobilization

Researchers reported Vmh2 from *Pleurotus ostreatus* is able to bind molecules like glucose, thus offering the possibility of using Vmh2 as a surface functionalization tool in

bio-hybrid devices.[59-60] Vmh2 and HFBI hydrophobins are also found to immobilize graphene oxide.[61-62] [63] HFBI can interact with a graphite surface in water too.[64] Binding with hydrophobin-polymer conjugated can also been achieved by Kostiainen et al.[65] Gazzera et al. used HFBII hydrophobin to improve the efficiency of binding of a phosphate-terminated perfluoropolyether onto polystyrene, polypropylene and low-density polyethylene surfaces.[66] Varjonen et al.[67] and others[68] demonstrated the interaction between a genetically engineered HFBI and cellulose nanofibrils enhanced self-assembly of nanocellulose at the air/water interface and formation of thin layers of tightly packed fibrils.

1.5.3   Coatings

Highly oriented pyrolytic graphite (HOPG) electrodes coated with HFBI were tested electrochemically.[69-70] A matrix-assisted laser desorption/ionization (MALDI) steel sample-loading plate was coated with Vmh2 and this allowed for a simple and effective desalting method suitable for development of lab-on-plate platforms focused on proteomic applications.[71] Mixture of caseins and hydrophobins have been deposited on cotton fabrics. The surface treatments have enhanced the flame retardancy of the fabrics.[72]

1.5.4   Foams and Emulsions

Emulsions made from hybrid capsules containing hydrophobin and hydroxyapatite mineral are stable in an aqueous environment.[73-74] The hybrid capsules can serve as microreactors. Foam stability were of interest in the presence of HFBII hydrophobin[48] and another surface-active agent such as β-casein[75] or milk proteins.[76] Hydrophobins could even affect the mouthfeel of ice cream by reducing the amount fat in ice cream[48] and

become useful for design capability of ice cream.[77] Hydrophobins also play roles during beer gushing in the brewing industry.[78-79] The explosion of hydrophobin-coated CO_2 nanobubbles provokes the gushing effect of a beverage when opening a bottle.[80] Hydrophobins as novel functional ingredients in terms of formation and stability of food foams and aerated emulsions has been reviewed.[50]

1.5.5 Drug Release

Hydrophobic drug molecules can be dispersed by hydrophobins to improve their bioavailability. For example, water-insoluble drug particles coated with the Class II hydrophobin HFB II are stable for at least 5 hours in suspension, and they could be stored for longer periods after freeze-drying.[81-82] Other examples are use of hydrophobins in formation of water-insoluble drugs for oral administrations,[83] and delivery of hydrophobin-functionalized porous silicon nanoparticles by altering the hydrophobicity of the particles.[84]

1.6 Cerato-ulmin

Cerato-ulmin was first identified and discovered by Takai and Richards in 1973 long before the term hydrophobin was coined.[85] It has been extensively characterized by Richards and Takai et al. due to its phytotoxicity.[35, 85-91] It is believed that Cerato-ulmin is a wilting toxin of Dutch elm disease.[88-89] Takai and Richards were able to isolate the Cerato-ulmin using the bubbling technique, which blows the gas through the culture filtrate. Cerato-ulmin has unusual characteristics. Microstructures were observed in the

liquid shake cultures where single "units" assemble into "rods", "fibrils" and even "membrane". Takai first described how *Cerato-ulmin* is associated with the Dutch elm disease and proposed it as the causal agent to produce the symptoms of the disease when the pure protein is introduced to elm seedlings.[35] Researchers made little progress in characterizing *Cerato-ulmin* until 1979. Takai and Richards[86] developed isolation techniques and were able to partially purify *Cerato-ulmin*. The partial structures of *Cerato-ulmin* were characterized.[87] It was reported (wrongly) that *Cerato-ulmin* is a small protein having 128 amino acids with a molecular weight of 13000 g/mol. A part of the amino acid sequences was determined by that time. Russo et al. studied the surface activity and solubility of *Cerato-ulmin*. They described that *Cerato-ulmin* can lower the surface tension at concentrations as low as 30 ng/mL and assemblies of *Cerato-ulmin* can be dissociated with 70% ethanol or by pressuring or cooling.[15, 46] The mechanism by which *Cerato-ulmin* causes the Dutch elm disease is still not fully understood but evidence was shown *Cerato-ulmin* plays an important role.[88-90]

More recent studies have improved our understanding of molecular structure of *Cerato-ulmin*. The complete amino acid sequence of *Cerato-ulmin* was determined, showing it has 8 cysteine and 75 residues overall compared to the 128 reported earlier.[91] The molecular weight calculated from amino acid sequences is 7618.7 g/mol compared to 13,000 g/mol estimated earlier, which is consistent with our mass spectroscopy result. The infrared and Raman data indicated the secondary structure and all eight cysteine residues formed disulfide bonds.[91] These are very important to understand the structure-function relationship of *Cerato-ulmin*. Temple et al. studied the biological roles of *Cerato-ulmin* hydrophobin.[92-93] *Cerato-ulmin* is not as easy to obtain as HFB II, and it has not caught a

lot of attentions from materials science stand point of view although it is heavily studied in the phytopathology field.[35, 86-90, 92, 94] Recently Rosu et al.[54] took advantage of the dispersal capability to align and organize semiconductor polymer such as poly(3-hexylthiophene). They found the sensor device has a better performance on transporting the electrons and charges.

CHAPTER 2. STABILITY OF HYDROPHOBIN *CERATO-ULMIN* AIR-ENCAPSULATE BUBBLES OR OIL-ENCAPSULATED DROPLETS

2.1 Introduction

Surfactants play significant roles in forming and stabilizing foams, emulsions and bubbles.[95-97] They can be used as foaming agents, emulsifiers and stabilizers. As natural surfactant-like proteins, hydrophobins have shown the ability to stabilize foams and bubbles for a long period of time. Cox et al.[49] studied the surface properties of Class II hydrophobin HFB I and HFB II and found these proteins have a significant impact on the stability of air bubbles as well as the process of coalescence and disproportionation (bubble shrinkage). The protein-coated air bubbles were stable for more than 1 hour, but other protein-coated bubbles such as β-casein or sodium dodecyl sulfate (SDS) are very unstable to disproportionation. The bubbles tend to shrink and disappear eventually after a few minutes. Even more remarkably, Basheva et al.[47] used a specific cell to show that blown bubbles formed in HFB II hydrophobin solutions preserved the non-spherical shape in micrometer size. Wrinkles with periodic undulations were seen on the bubble surfaces indicating mechanical strength not common to other protein-stabilized bubbles. Cox and coworkers further studied the foam stability of aerated solutions containing HFB II hydrophobin.[48] HFB II has been found to form remarkably stable foams under different pH

conditions at a concentration of 0.1 wt%. Moreover, the foams stabilized by HFB II were very stable over a period of at least 4 months. No such studies have been performed on *Cerato-ulmin* hydrophobin, although CU efficiently forms foams and bubbles in the process of purification. The observations of microstructures like rods, fibrils and membranes demonstrate that *Cerato-ulmin* has good stabilizing ability. Therefore, it is intriguing to study and understand the behavior of *Cerato-ulmin* as a stabilizing agent.

Cerato-ulmin (CU) is known to produce an especially wide variety of unusual structures in aqueous solution. It has been proposed that they are air bubbles which are not nominally spherical but in cylindrical shape. Not only can *Cerato-ulmin* form air bubbles, it is also capable of entrapping various gases into unique shapes. In the case of presence of immiscible liquids in CU aqueous solution, CU is able to encapsulate them into cylindrical bags or drops. CU's ability to stabilize gas bubbles and oil drops are of interest under different conditions.

The objective of this chapter is to investigate the ability of CU to entrap air in aqueous solution as well as to entrap immiscible oil in aqueous solution. Then different conditions, for example, vacuum, heat, and solvent variations have been used to manipulate the CU-stabilized structures while observing their remarkable stability.

2.2 Materials and Methods

2.2.1 Reagents and Chemicals

A commercial hydrophobin H*Protein B from BASF was used as a study model. The early-stage of the study was to characterize the commercial hydrophobin. H*Protein B hydrophobin is in the appearance of brownish granulates. The amount of the active content is not known.

Cerato-ulmin was a gift from Wayne Richards of the Canadian Forest Service. It was produced by an aggressive strain of C. ulmi (RDT2) and purified by the methods of Takai and Richards[86] and Stevenson et al.[87] The purified sample was stored in a sealed vial and placed in a jar filled with Drierite® ($CaSO_4$) at ambient temperature and pressure. The water used to prepare CU aqueous stock solutions was supplied by a Barnstead Nanopure® purification system. The stock solution of CU was prepared at a concentration of 0.02 mg/mL.

2.2.2   Isolation and Purification of Hydrophobin H*Protein B

As the active content in hydrophobin H*Protein B is unknown, the purification is needed. The general procedure is shown in Figure 2.1 according to other research papers.[36, 98] In brief, the brownish H*Protein B granulates were dissolved in deionized water at the desired concentration. The suspension was mixed and the H*Protein B granulates started swelling after a few minutes. The suspension was stirred with a stirring rod for a few hours (except that sometimes overnight stirring was needed) to ensure the protein fully dissolved. Insoluble impurities were seen and remained in the suspension. After removing the insoluble impurities by centrifugation (step 1 in Figure 2.1), supernatant was distributed into two vials (labeled as A and B in Figure 2.1). One portion of supernatant was freeze-

dried and then treated with/without trifluoroacetic acid or TFA (step 2, labeled as C and D). TFA was removed from the supernatant C with a stream of nitrogen and 60% v/v ethanol was added to the residue (step 3). Supernatant C1 was collected by centrifugation one time and freeze-dried. Sample A, C1, C2, and D were kept for later characterization.
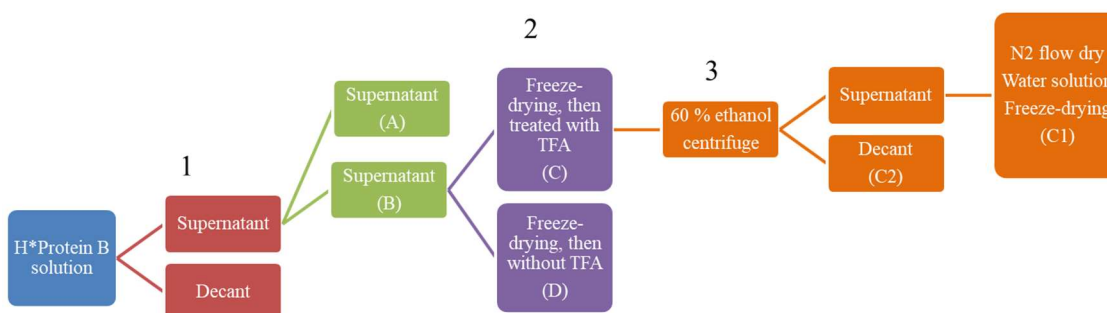
Figure 2.1. Purification procedure of commercial hydrophobin H*Protein B (step 1: centrifuge; step 2: TFA treatment; and, step 3: ethanol treatment).

2.2.3 *Sodium Dodecyl Sulfate-Polyacrylamide Gel Electrophoresis (SDS-PAGE)*

The SDS-PAGE was performed in Professor Vince J. Licata's laboratory at Louisiana State University. The general procedure was followed by the one provided by Thermo Scientific. In brief, electrophoresis was performed to identify hydrophobin H*Protein B present in both raw materials as received and our isolation product. A 12% separating protein polyacrylamide gel was prepared in 0.375 M Tris at pH 8.8 and a 4%

stacking protein polyacrylamide gel was prepared in 0.125 M Tris at pH 6.8. The run voltage was set at 175 V and running time was 45 minutes. 1 mg/mL of hydrophobin H*Protein B solutions were dissolved in sample buffer (a mixture of 0.5M Tris-HCL, Glycerol, 10% w/v sodium dodecyl sulfate, β-mercaptoethanol and 0.05% w/v bromophenol blue) and then were loaded into the wells to determine purity and to approximate molecular mass. Polypeptide bands were visualized by staining with Silver Stain Plus (Bio-Rad).

2.2.4 *Matrix-Assisted Laser Desorption/Ionization-Time of Flight Mass Spectrometry (MALDI-ToF MS)*

MALDI-ToF mass spectrometer was used to determine the mass and identity of hydrophobin H*Protein B and *Cerato-ulmin* (CU). The matrix used was 2,5-dihydroxybenzoic acid (DHB) dissolved in 0.1% TFA. A total of 1 µL of the hydrophobin sample (1-2 mg/mL for H*Protein B and 0.2 mg/mL for CU) was spotted on a MALDI target and mixed with DHB (1 µL of 10 mg/mL).

2.2.5 *Circular Dichroism Spectroscopy (CD)*

CD spectroscopy was performed to identify secondary structure organizations of hydrophobin H*Protein B and CU. The effects of alcohol, temperature and pH were investigated. CD spectra were obtained for wavelength of 185-250 nm using a quartz cuvette with 0.1 cm path length and the Jasco J-185 spectropolarimeter in continuous scanning mode. Acquisition parameters included a scanning speed of 50 nm/min, 1 nm bandwidth, and 0.5 nm or 1 nm data pitch. Data sets were averaged over three scans and preceding solvent blank were subtracted.

2.2.6   UV-Vis

UV-Vis spectra were collected with Agilent 8510 UV-Vis spectrometer with a cuvette path length of 1 mm.

2.2.7   Contact Angle Goniometry

Contact angle measurements were conducted to monitor the surface modification behavior of assembled hydrophobin. The sessile drop technique was employed using a Rame-Hart goniometer coupled with DROP-image data analysis software. The static contact angle formed by drops of deionized water was measured on each surface immediately after deposition.

2.2.8   Optical Microscopy

The optical images were observed with a Leica DMR optical microscope equipped with a Canon EOS6D digital camera (1920×1080 pixels) or a high speed scientific pco.edge sCMOS camera (1920×1080 pixels). Various objective lenses (10×, 20×, 40×, and 50×) were used for different purposes. A Linkam PE120 Peltier heating stage (-25 °C to 120 °C) was used for temperature control. The experimental set up consists of a rectangular glass tubing (Vitrocom, Inc.), a syringe pump (Harvard Apparatus) and a standard optical microscope (Leica DM2500P) with a digital camera (Canon EOS6D). A volume of CU solution (10 µL to 200 µL) were transferred to a modified VitroCom rectangular cell with 1 mm thickness and 1 cm width. Tygon tubing was used to connect the glass vial, syringe pump and differential pressure meter (Extech, model 407910). Microscopy images were taken using bright-field illumination.

2.2.9   Atomic Force Microscopy

CU solution (a concentration of 0.02 mg/mL) was agitated by hand shaking to generate air bubbles. An aliquot of CU air bubble solution was drop-cast onto silicon wafers that have been cleaned with isopropanol and air-dried. The protein solutions are allowed to dry the bubbles on the substrate for imaging. AFM probe MPP-11100-10 was selected (cantilever length, 125 μm; nominal force constant, 40 N/M, and resonance frequency, 300 kHz). Height, phase, and amplitude images were collected simultaneously. The image size ranged from 4×4 μm^2 to 50×50 μm^2, while the resolution was held constant at 512×512 data points.

2.2.10   Simultaneous Multi-Angle Multi-Correlator Dynamic Light Scattering

The instrument was originally home-built by former group alumnus Dr. Grigor Bantchev.[99] In general, HeNe red laser (632.8 nm) was used for the set-up. Single-mode fiber optic detectors were housed in the sample holder and separated by every 15°. The scattering angle ranges from 15° to 175°. The number of angles that can be measured simultaneously is limited to 8 by the correlator and software. The scattering signals were detected by PMT devices. The detected signals were fed in and analyzed with a multi-tau Correlator.com Flex01/08Ch. The device's channels are arranged in a series of blocks. In the first block of 16 channels, each channel is separated by 200 ns. In the next block of 8 channels, the interchannel time doubles to 400 ns. In subsequent blocks, the sample time again doubles. The software was written in LABVIEW 7.0 by Dr. Grigor Bantchev for collecting data. The software is capable of providing the intensity trace, the correlation curves for all angles and cumulant data analysis.

For the present work, the fiber optics aligning system has been modified and updated to improve instrument performance. New optical fiber positioners have been designed and built, which are similar to those used in Wyatt Dawn EOS model for DLS detection. The PMT detectors were also upgraded to Excelitas single photon counting modules. The newest simultaneous 8-angle 8-correlator DLS was further combined with Wyatt Dawn EOS 8-angle static light scattering. Taking advantage of Wyatt Dawn EOS sample holder, one can measure both DLS and SLS simultaneously with batch mode. This is one of the first instruments of its kind.

2.3   Results and Discussion

2.3.1   H*Protein B Isolation and Characterization

SDS-PAGE and MALDI-ToF MS analysis were used to determine the identity of the isolated H*Protein B hydrophobin. Figure 2.2A shows SDS-PAGE of raw H*Protein B hydrophobin suspension. The column 1 and 2 is lysozyme as a reference. The column 3 is the marker from broad molecular weight standards. The rest of the columns in Figure 2.2A represent raw H*Protein B hydrophobin suspension filtered with 0.45 μm PVDF membrane and without further purification. In silver stained gels, two heavy bands are observed for the first two columns and several heavy bands are also seen for column 3. The lysozyme bands are horizontally aligned with the one from the molecular weight maker, which represented the lysozyme with molecular weight of 14 kDa. The raw H*Protein B shows much fainter bands at an apparent molecular mass of 40 kDa from column 4 to 8. Heavier bands are seen and remain at the loading wells. This indicates the raw H*Protein

B may contain different states of aggregation of the protein in the suspension. Even the bands near 40 kDa can be possibly attributed to aggregates, such as dimers or tetramers. Such aggregation appears to be characteristic of hydrophobin proteins and has been reported previously.[30] Very similar SDS-PAGE results were obtained from H*Protein B treated with TFA. In Figure 2.2B, column C1 represents TFA-treated H*Protein B and column D is non-TFA treated. There is no significant difference in SDS-PAGE bands. Overall, fainter bands for all four columns are observed near 40 kDa, which is consistent with previous results. TFA is believed to dissociate the oligomers of hydrophobin. Non-TFA treated bands (column A and D) show residues from the top of wells to the end band. TFA-treated H*Protein B (column C1 and C2) bands are not obvious. This could be due to loss in protein during centrifugation.

A   B
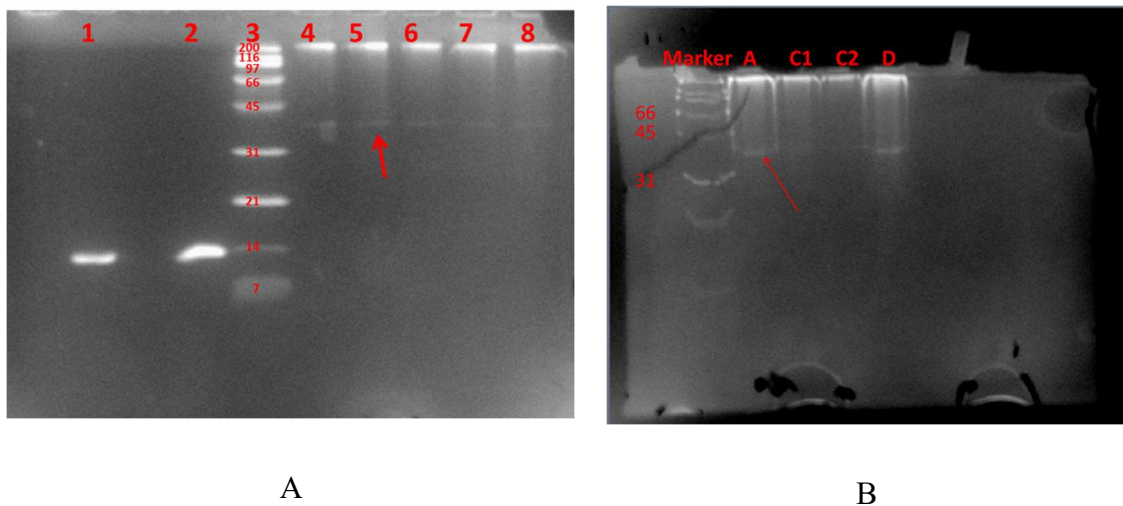
Figure 2.2. SDS-PAGE results. Column 1-2 is lysozyme, 3 is the marker, and column 4-8 are 1 mg/mL H*Protein B filtered with 0.45 µm PVDF membrane and without

further purification. Column A, C1, C2 and D are purified H*Protein B samples following the procedure shown in Figure 2.1.

MALDI-ToF analysis (Figure 2.3) further confirms the impurity of H*Protein B hydrophobin. Two large peaks are observed at 6436 Da, 9320 Da, and a minor peak is visible at approximately 18931 Da which could be attributed to other components in the protein or dimer or trimer aggregates. After filtering and freeze drying, H*Protein B protein appears to be white and fluffy. The MALDI-ToF signal is much smoother after freeze drying. Several small peaks near 8729 Da become broad and merge together. To figure out the amount of active content and further purify the H*Protein B protein, more sophisticated characterization such as using HPLC is required. This is out of scope of the thesis. Nevertheless, MALDI-ToF of CU in Figure 2.4 shows a large peak at 7623 Da without residual peaks, indicating the raw white CU powders are pure and do not contain impurities. Further purification is not needed for CU and the protein is used as received. The complete amino acid sequence of *Cerato-ulmin* was reported to have 8 cysteine and 75 residues.[91] The molecular weight calculated from amino acid sequences is 7618.7 g/mol, which is consistent with MALDI-ToF molar mass analysis.
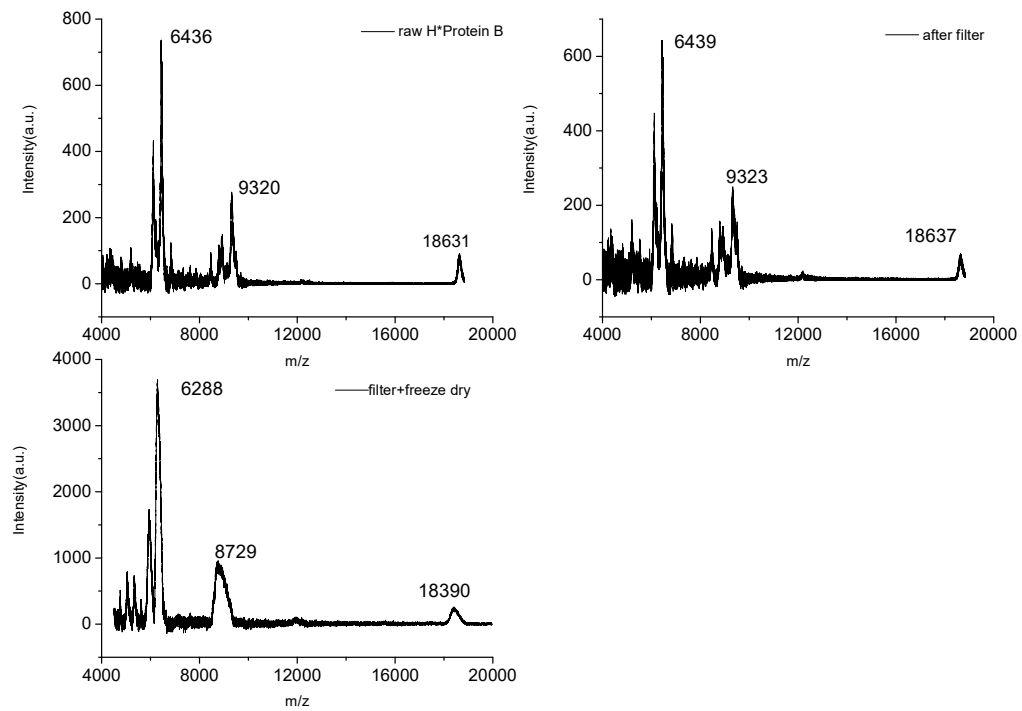
Figure 2.3. MALDI spectrum obtained from H*Protein B w/o filtering and freeze-dry treatment.
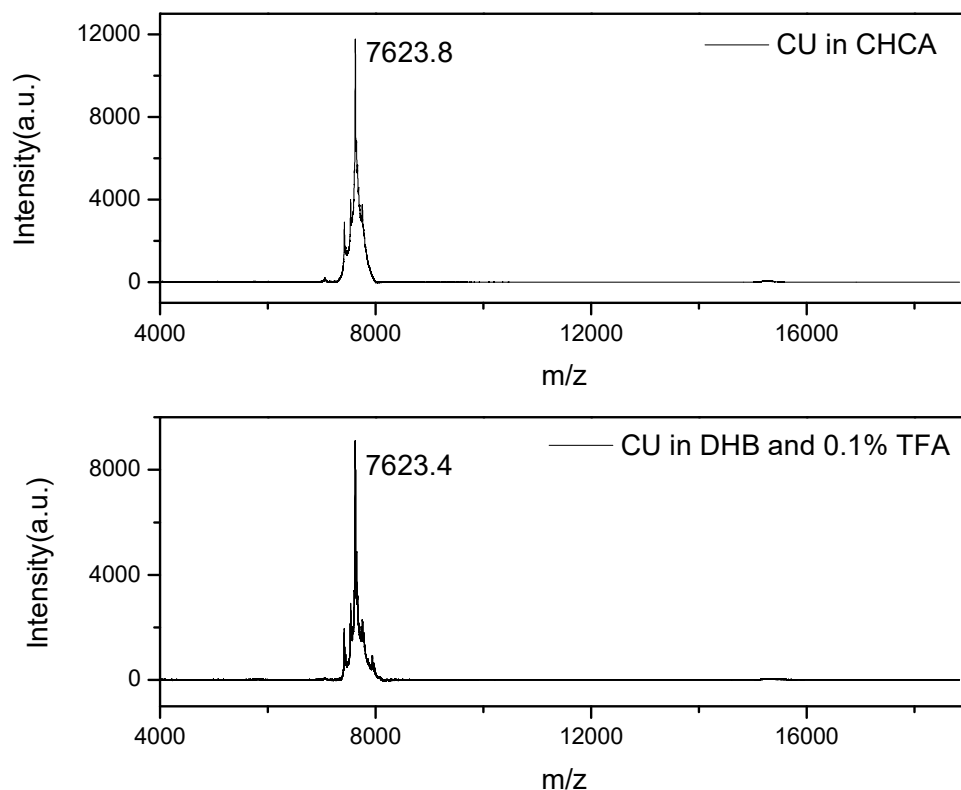
Figure 2.4. MALDI spectrum of CU showing a single broad peak.

Circular dichroism was performed to identify secondary structural changes that occur in the bulk hydrophobin H*Protein B solution. Bovine serum albumin or BSA was first measured to test the instrument, as shown in Figure 2.5A. BSA samples were raw proteins, and either treated with TFA or not. CD spectra of BSA protein solution show characteristic peaks in the far infrared wavelength. The peaks at 205 nm and 225 nm indicate the BSA remained in a predominantly α-helical conformation in the bulk solution. In Figure 2.5B, similar CD spectra were obtained from H*Protein B hydrophobin solution,

suggesting H*Protein B is rich in α-helix. Introducing TFA to H*Protein B solution is believed to dissociate aggregates or self-assemblies. TFA treatment seems not to have an effect on secondary structure of hydrophobin H*Protein B in bulk solution. It is reported that for other hydrophobin such as SC3, no secondary structural changes result from TFA treatment too.[42] Adding alcohol improves the solubility of hydrophobins. The CD spectra of H*Protein B dissolved in 60% v/v ethanol is shown (Figure 2.6A). Again, two characteristic peaks for α-helix structure were observed, indicating no significant secondary structural changes occur in the H*Protein B bulk solution by the effect of alcohol. Heating the H*Protein B bulk solution during CD measurements can cause secondary structural changes. Figure 2.6B depicts CD spectra changes under heat treatment. By increasing the solution temperature (indicated by red arrow), the peak at 223 nm gradually disappears and merges with the peak at 205 nm to become a single broad band. It means α-helix is the dominant structure for H*Protein B at low temperature (between 20 °C and 50 °C). Then the secondary structure turns into β-sheets conformation at high temperature, characterized by the broad peak at 205 nm. Potassium phosphate buffer solutions made at different pH (4.20, 5.88, 8.31, and 9.71) were used to determine whether secondary structural changes occur under pH conditions. As shown in Figure 2.6C, α-helical conformation exists in the bulk solution at moderate pH condition. The peaks at 205 nm shifted to 200 nm and peaks at 225 nm are gone as pH value increased. It suggests the secondary structure has changed from α-helix to β-sheets.

CD measurements on CU as a function of concentration of proteins, temperature, alcohol, and oil presence have been conducted and will be discussed in Chapter 4.
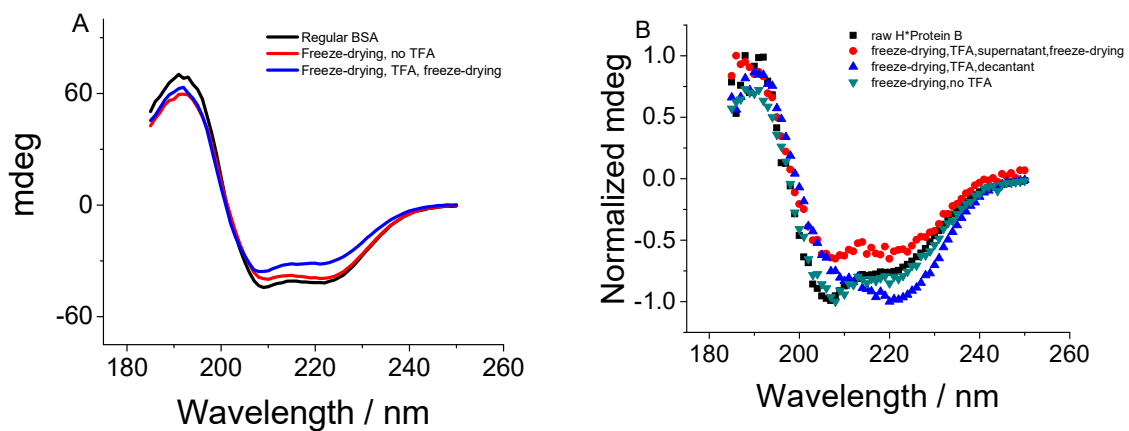
Figure 2.5. CD spectrum of H*Protein B sample A, C1, C2, and D in Figure 2.2 and BSA w/o TFA treatment.
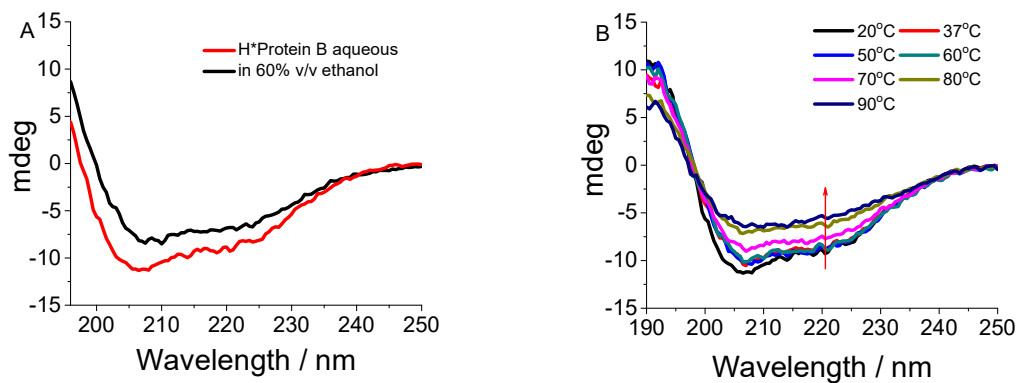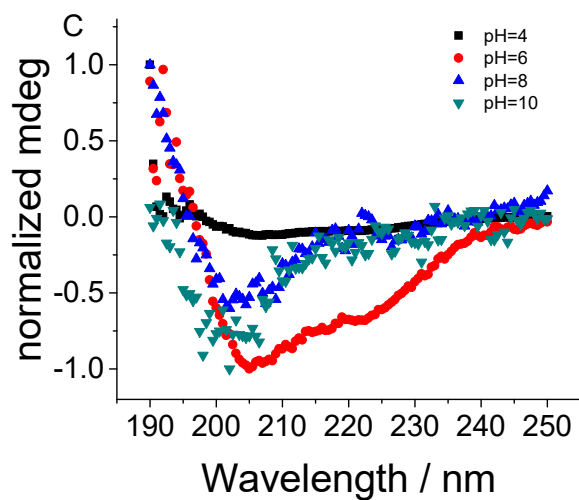
Figure 2.6. Alcohol, temperature and pH effect on secondary structure of H*Protein B.

Takai reported the UV absorption of 2 mg/mL of CU in 60% aqueous ethanol exhibited peaks at 269 nm, 278 nm and 285 nm (shoulder).[86] Due to the limited amount of CU, 0.2 mg/mL CU aqueous solution was prepared. Weak UV absorption peaks were observed at 285 nm (Figure 2.7). It is believed that increasing the concentration of CU can improve the signal/noise of the absorption peak. This is true in the case of H*Protein B. Solutions with higher H*Protein B concentrations were made for UV-Vis, such as 3 mg/mL and 30 mg/mL. For example, the maxima wavelength of 297 nm and 325 nm (shoulder peak) were shown.
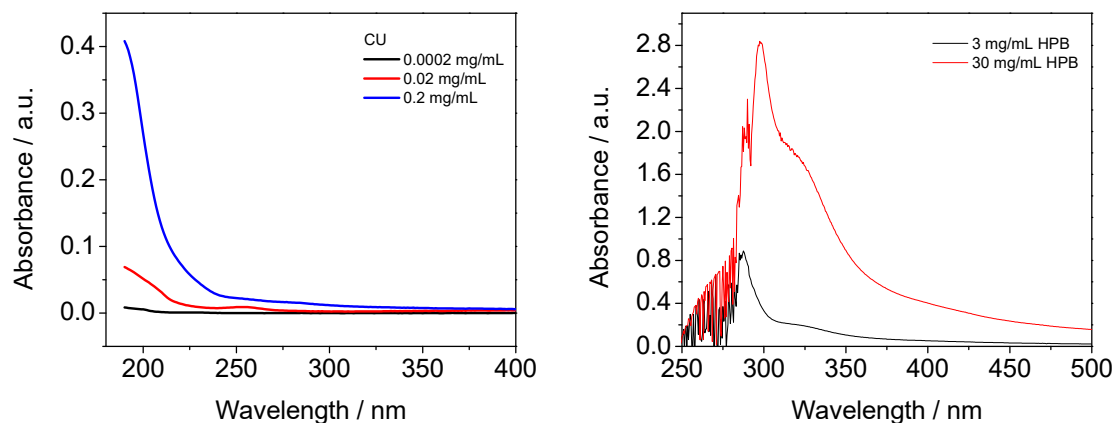
Figure 2.7. UV-Vis spectra of CU and H*Protein B.

The contact angles were measured on both microscope cover slip (VWR) and Teflon PTFE sheets (McMaster-Carr, Catalog #:8545K18, 3/8" thickness with tolerance of -0.0019" to +0.038"). The glass cover slip and Teflon were submerged in ethanol for 5 min and rinsed with 18 mΩ milliQ water and then air-dried. Another set of clean glass cover slips and Teflon were submerged in 0.02 mg/mL CU aqueous solution and incubated for 4 hours. After the protein was allowed to assemble at the substrate interface, the substrate was removed from the solution, rinsed with milliQ water, and dried with air. The hydrophilic glass substrate has a water contact angle of 48.8° and beads up with an increase of 7.1° after treatment with CU (Figure 2.8). The hydrophobic Teflon substrate displayed opposite behavior. The water contact angle decreased from 115° to 93°. It suggests CU-coated Teflon substrate has turned hydrophobicity to hydrophilicity. The wetting and de-wetting behavior confirms CU has both hydrophilic and hydrophobic side in the monomeric molecules. When hydrophobins bind to a hydrophilic surface, the hydrophobic

side is exposed to the outside, and vice versa. The amphiphilic properties of hydrophobins allow hydrophobins to self-assemble at the hydrophilic/hydrophobic interface.

Teflon
115° ± 2°

CU-coated Teflon
93° ± 12°

Glass
48.8° ± 0.1°

CU-coated Glass
56° ± 6°
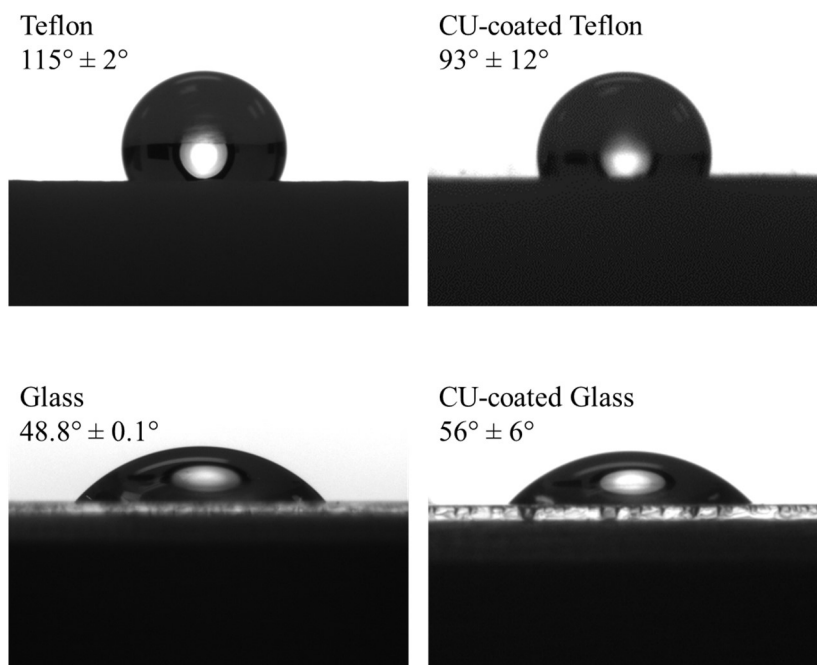
Figure 2.8. Water contact angle of glass and Teflon surface with and without CU (0.02 mg/mL) coating. Measurements were taken at various locations on the surfaces.

The impact of concentration of CU on contact angle is illustrated in Figure 2.9. Instead of coating the substrate with CU, a microliter of CU drop was directly deposited. Table 2.1 summarizes the contact angle measurements. CU reduces the contact angle on bare Teflon substrate from 124° ± 3° to 89° ± 5° with an increase in concentration from 0.02 mg/mL to 0.5 mg/mL, whereas H*Protein B has changed hydrophobicity much less at a concentration of 2 mg/mL. CU seems to be more efficient. As CU concentration increases, the shape of CU drop changes too from round to irregular. The irregular drop

shrinks after 10 min. It is an indication of strong membrane has formed at the air-water interface. The 0.5 mg/mL CU drop exhibit a flat surface atop at long times. The observation of the flat surface has also been found from HFBI and BslA hydrophobin by other researchers. [100-101]
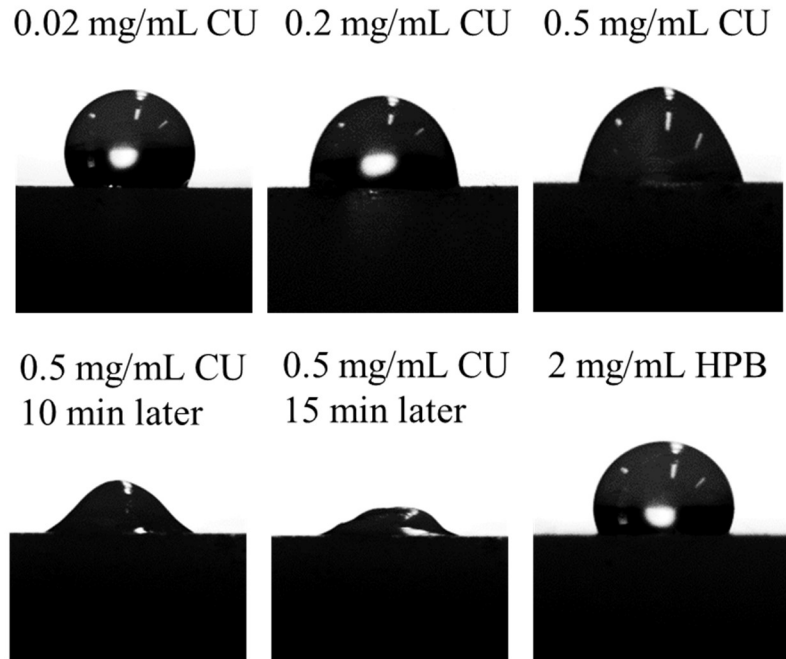
Figure 2.9 Contact angle of CU and H*Protein B droplet on bare Teflon substrates.

Table 2.1 Summary of contact angle measurements by depositing CU and H*Protein B drop directly on bare glass and Teflon substrates.

Sample	Glass (°)	Teflon (°)
Water	10 ± 1	115 ± 1
H*Protein B (mg/mL)		
0.02	37 ± 3	117 ± 2
0.2	31 ± 1	121 ± 2
0.5	25 ± 4	116 ± 2
1	36 ± 2	117 ± 5
2	37 ± 1	118 ± 4
CU (mg/mL)		
0.01	45 ± 3	124 ± 3
0.2	38 ± 4	102 ± 10
0.5	31 ± 5	89 ± 15

2.3.2   The Stability of Air Bubbles and Oil Droplets

2.3.2.1   Air Bubbles and Oil Droplet Structures

The early stage of this research was focused on phenomenological study. CU hydrophobin can very efficiently form air bubbles and oil droplets under small agitations. The resulting air bubbles and oil droplets are non-spherical in shape. In comparison, the H*Protein B hydrophobin is less likely to form non-spherical air bubbles. The typical

experiments were carried out using an optical microscope and digital or high-speed camera. A 0.02 mg/mL CU stock solution was prepared by dissolving the dry CU powder into nanopure water. The solution turns opaque when the solution vial is gently shaken, and some millimeter-scale particles are seen by the unaided eye. They are like particles suspended in water. It is clear that these particles are in various structures from optical microscopy images. For microscopy experiments, ~ 50 µL of CU solution is transferred into a Starna$^©$ cell where the path length is 1 mm. The cell containing the CU solution is immersed into a sonication bath for a few seconds before gently shaking the cell or slowly giving a shear force. Figure 2.10 shows typical images seen under the microscope. Figure 2.10A and B are rod-like structures and fiber-like ones made by bare CU solution. The differences in controlling the agitation by hands gives arise to the structures in different length scales. Nevertheless, these rods and fibers are more or less in the micron size range. The ability to control the agitation and size distribution may be challenging but still can be accomplished. One approach could be using a wave tank to generate steady waves instead of hand shaking. It is proposed that these cylindrical structures have entrapped air inside. Further study has confirmed this idea and will be discussed later. When the cell containing cylindrical structures is bath-sonicated for a few seconds again, the structures disappear. Amazingly, the process of forming and destroying structures can be repeated many times. Adding a thin layer of oil (a few microliters) to CU solution can make oil droplets in unusual shapes by agitation as well. CU is able to entrap the oil into these long tails or fat bags as shown in Figure 2.10C and D. A variety of hydrocarbon oils, hexane, cyclohexane, dodecane, squalane, benzene, toluene and Macondo oil (from the Gulf of Mexico oil spill incident of 2010), have been tried; all show similar phenomena. The size ranges of oil

droplets are much bigger than the rods or fiber-like structures. Membranes and wrinkles are also seen on the surfaces of oil droplets.
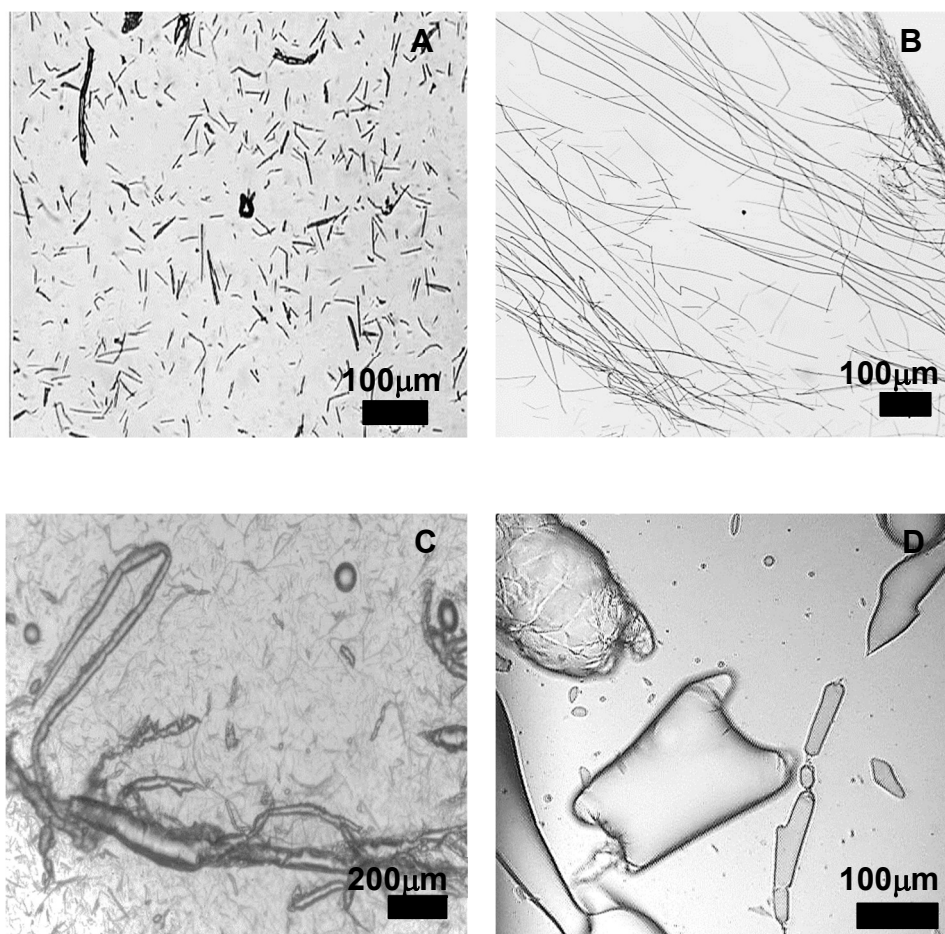
Figure 2.10. Typical optical microscopy images of CU dispersion after agitation in the absence (A and B) and presence of benzene (C) and cyclohexane (D).

2.3.2.2   Physical Effects on the Stability of Bubbles and Droplets

One way to characterize the stability of air bubbles and oil droplets is their response to physical effects such as pressure and temperature. They behave differently in the case of air-filled bubbles and oil-filled droplets (see video S2.1&S2.2). For this purpose, a vacuum system was constructed. The solution cell was connected with a syringe pump and a differential pressure manometer by a three-valve connector though PVC tubing. Figure 2.11 demonstrates the behavior of CU air bubbles under pressure change conditions. Agitation of CU solution forms cylindrical bubbles before any further process (Figure 2.11A). Applying a vacuum to the system, the cylindrical structures are in tension and expand into spherical structures (Figure 2.11B). Further increase in tension (up to -760 mbar) causes formation of a few large spherical structures. As the tension is subsequently lowered, the surface of the spheres starts to crinkle and wrinkles are seen. When the tension is removed, the structures begin to break up (Figure 2.11C). This sequence of events suggests that these "rods" are cylindrical air bubbles. When overpressure is applied, the "rods" and "fibrils" disappear (Figure 2.11D); they tend not to reappear after the pressure is released, indicating the air bubbles are present in submicron size (Figure 2.11).
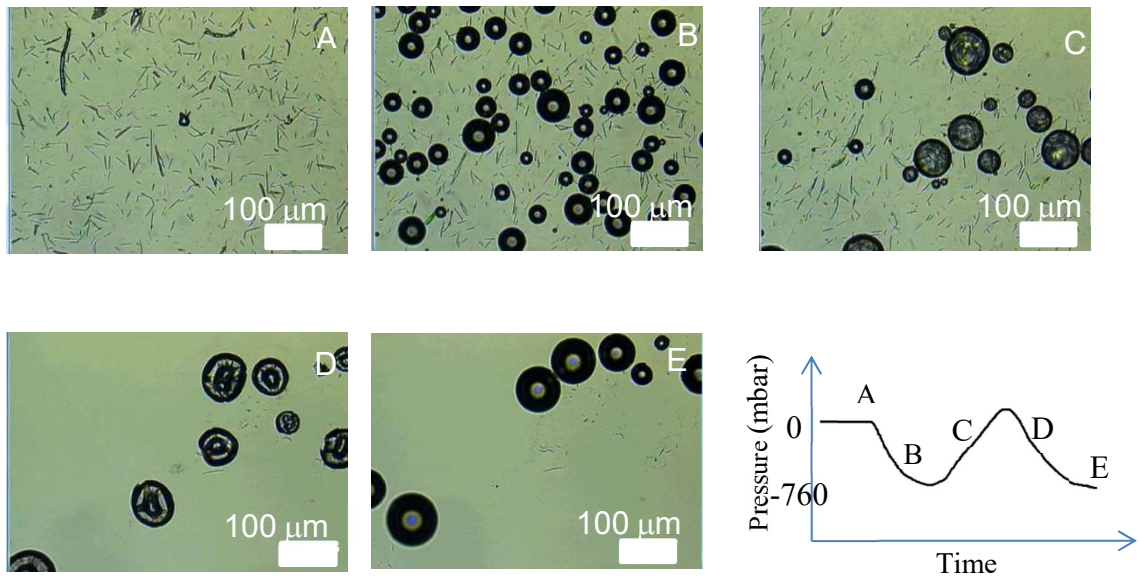
Figure 2.11. Unique behavior of CU air bubbles under pressure change conditions.

Oil-filled droplets behave differently; they maintain their structures or shapes when they are either exposed to the vacuum or after releasing vacuum as shown in Figure 2.12. One possible reason is the virtual incompressibility of oil. The pressure change in the system here is still relatively small. Another explanation for this phenomenon is correlated with the thickness of membrane on the surfaces. The thickness for air bubbles and oil droplets can be estimated through image processing and mass balance. Knowing the molecular weight of single CU molecules and using the typical partial specific volume of proteins, the thickness of air bubble and oil droplets is single and multilayers.
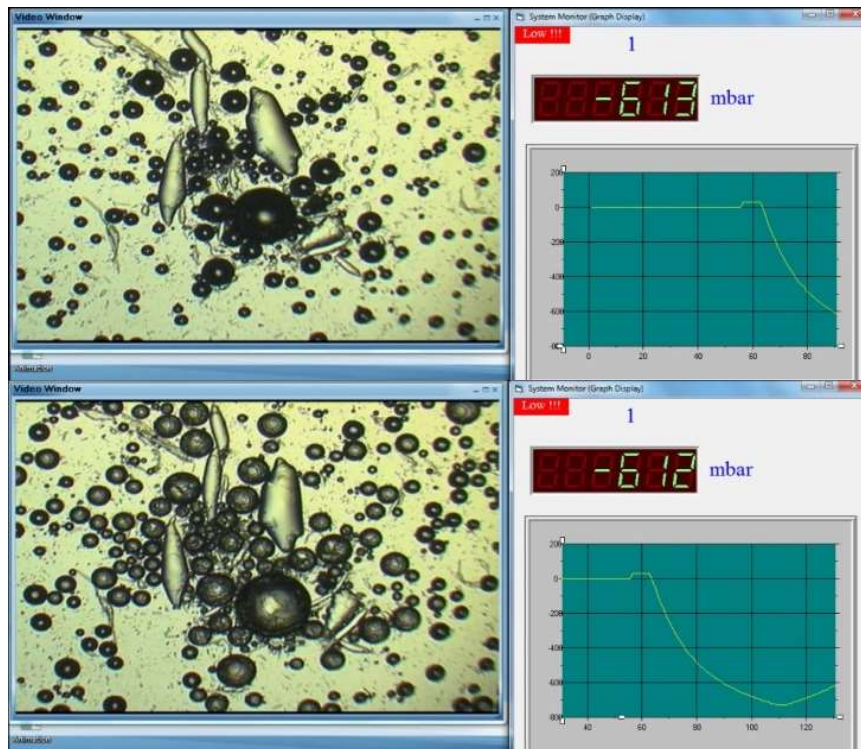
Figure 2.12. Oil droplets (sausage-like structures) remains their shapes under vacuum and removal of vacuum, whereas air bubbles (spheres) do not.

Temperature influences the stability of air bubbles. Increasing the temperature causes a similar effect on them as reduction in pressure (Figure 2.13). The cylindrical structures of bubbles turned into spheres as the solution warmed. The spherical bubbles did not collapse as the temperature further increased until very high temperature (100 °C) was reached. Meanwhile small cylindrical bubbles dissolved into the solution and disappeared. The collapsed bubbles eventually left membranes; over time, these continued dissolving into solution. The cylindrical bubbles behaved similarly instead of skipping the transition

to spherical structure when cooling from room temperature. The visible debris indicated by arrows in Figure 2.13D will be revisited; their diffusivity and corresponding hydrodynamic radius will be determined using a particle sizing technique in Chapter 5. The effect of temperature increase on toluene-filled droplet in CU solution was investigated. The temperature was raised to 70 °C and the droplets are very stable to the temperature change and retained their structures. Benzene-filled capsules also behave similarly as the system was cooled to freeze the water (and presumably the benzene). The stability of CU-encapsulated oil droplets must be correlated with the boiling and freezing point of the hydrophobic solvent.
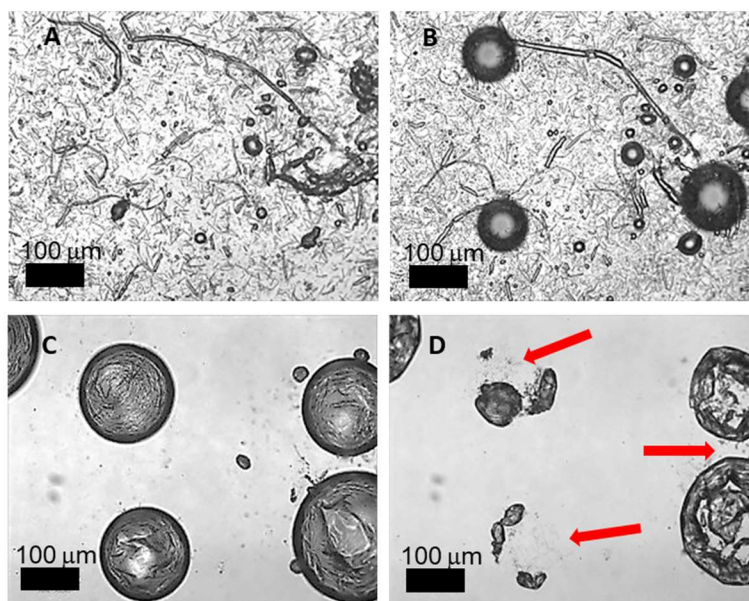
Figure 2.13. Temperature effect on bubbles (A) at 25 °C, (B) at 55 °C, (C) at 100 °C and 3 min after 100 °C.

2.3.2.3 AFM of Air Bubbles

From the turbidity of the agitated stock solution, the air bubbles are seen to stay stable for minutes or hours in dispersions that are allowed to stand, undisturbed. A solution containing air bubbles is drop-cast on the glass slide and left open to the ambient environment. After the evaporation of water in the solution, large bubbles remain and their shapes and shells or membranes are left behind. Small rod-like bubbles are also seen (Figure 2.14). In Figure 2.15, AFM images provide more features of air bubbles after drying on the glass slide. The bubbles size decrease from micrometer to nanometer scale.
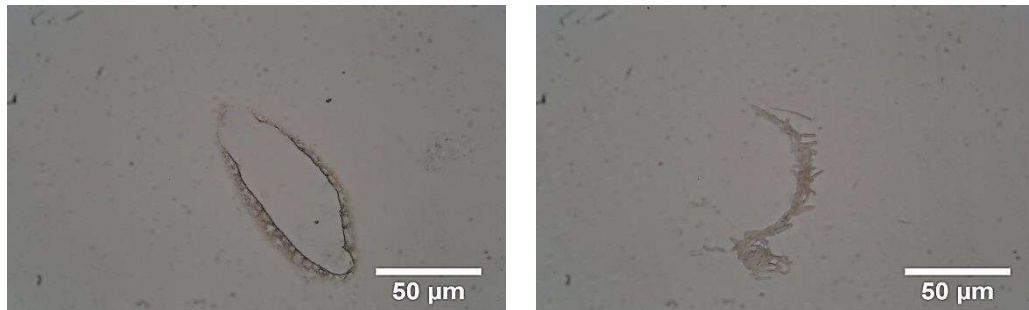
Figure 2.14. Optical microscope images of bubbles after drop-cast drying on the glass slide.

Figure 2.15. AFM amplitude images of bubbles after drop-cast drying on the glass slide.

2.3.2.4   Thickness of CU Membrane

The stability of air-encapsulated CU bubbles and oil-filled CU droplets could be attributed to the thickness of CU membrane at air-water and oil-water interfaces. Knowing the thickness of CU membrane will help to explain the strength and stability of the membranes. As the crystallography structure of CU has not been resolved, the dimension of single CU molecule can be estimated by $\frac{4}{3}\pi R_{CU}^3 = \frac{M}{\rho} \times \frac{1}{N_A}$ assuming CU is in globular spherical shape, where R_{CU} is the radius of a single CU molecule, M is the molecular weight of CU, ρ is the density of CU, and N_A is Avogadro's number. ρ is unknown here but equals

inverse of partial specific volume of CU, which can be replaced with a value for regular protein. As a result, the radius of single CU molecule is estimated to be 1.32 nm, which is similar to HFB II's value of 1.5 nm.[17] Using the ImageJ image analysis tool, the surface areas for air bubbles and oil droplets from optical microscopic images are measured. Under assumptions that CU molecules fully occupy the bubble and droplets surface, CU membrane has a thickness of made up of 1 - 9 molecules. It seems to be thicker for oil droplets than air bubbles. More sophisticated techniques have been tried to figure out CU membrane thickness, such as small-angle X-ray scattering and small-angle neutron scattering. It seems to be challenging to get useful data due to extremely weak scattering signal, even though the concentration of CU solution has been increased to 3 mg/mL and the entire solution become very viscous and gel-like after agitation at this concentration.

2.3.2.5   Free Energy of CU Molecule Detachment from Interfaces

Here, using the simplest model enables to compute the free energy of CU molecule detachment from interfaces, assuming the CU single molecule is a solid, spherical particle with a radius of r and contact angle of θ, as shown in Figure 2.16.
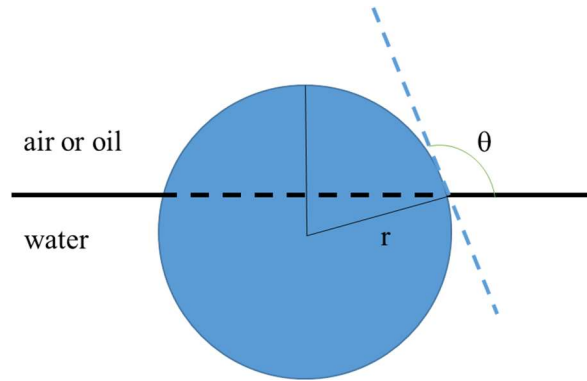
Figure 2.16. Small solid particle with radius of r and contact angle θ attached to a planar oil-water or air-water interfaces.

The energy required to remove one CU molecule from the interface is expressed by ΔE_{do} or ΔE_{da} (eqn 2.1), ΔE_{dw} (eqn 2.2) and ΔE_d (eqn 2.3), where ΔE_{do} or ΔE_{da} is the free energy of particle detachment into oil or air, ΔE_{dw} is the free energy of particle detachment into water and ΔE_d is the minimum energy for detachment into the bulk phase. Using the value of $r = 1.32$ nm, the surface tension of clean air-water interface of 72 mN/m and oil-water interfacial tension of 50 mN/m, the free energy of CU detachment is calculated as a function of contact angle θ and shown in Figure 2.17. The free energy required for CU detachment is at least 100 kT when $\theta = 90°$, indicating irreversible particulate adsorption at interfaces. The irreversibility of CU adsorption could contribute to the stabilization of CU air bubbles,[102] and yet eventually CU goes back into solution (or glass-water interface) after the bubbles disappear.

$$\Delta E_{do} \text{ or } \Delta E_{da} = \pi r^2 \gamma_{ow/aw}(1 - \cos\theta)^2 \qquad (2.1)$$

$$\Delta E_{dw} = \pi r^2 \gamma_{ow/aw}(1 + \cos\theta)^2 \qquad (2.2)$$

$$\Delta E_d = \pi r^2 \gamma_{ow/aw}(1 - |\cos\theta|)^2 \qquad (2.3)$$
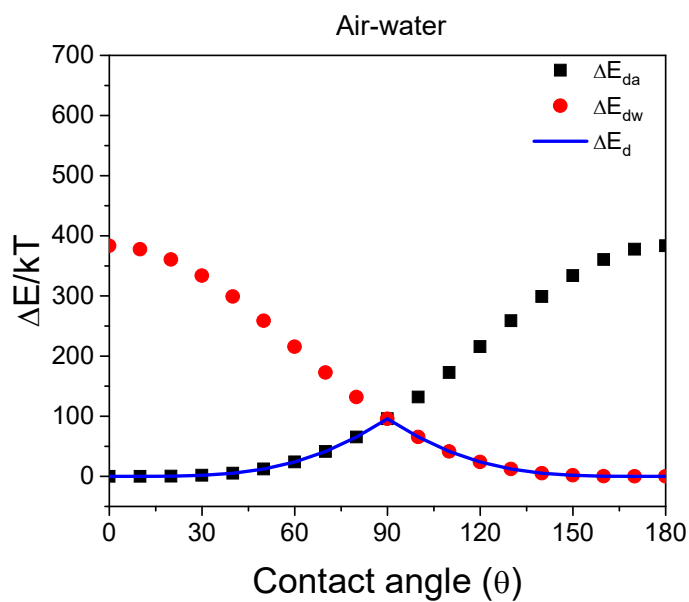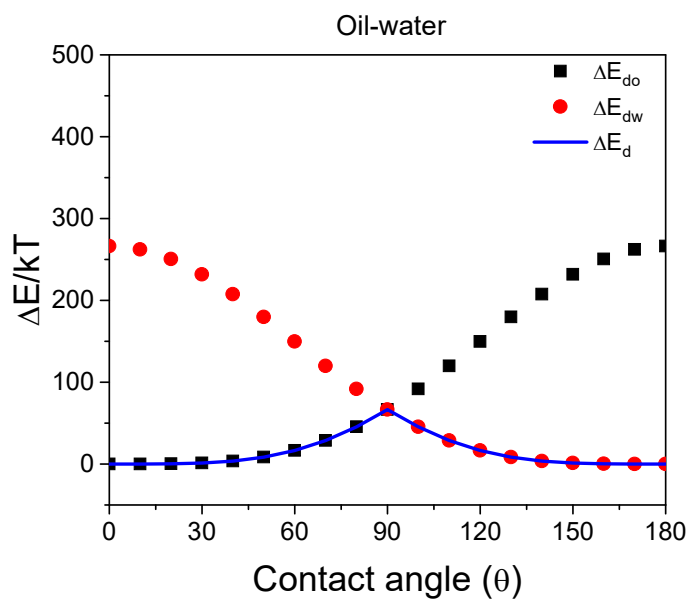
Figure 2.17. Free energy of CU molecule detachment into water (ΔE_{dw}) and into oil (ΔE_{do}) or air (ΔE_{da}) calculated by equations 2.1 and 2.2 with r = 1.32 nm, γ_{aw} = 72 mN/m and γ_{ow} = 50 mN/m versus contact angle θ. The line is drawn based on equation 2.3.

2.3.2.6   Dynamic Light Scattering of H*Protein B and CU

In dynamic light scattering, the particle size is characterized by hydrodynamic radius (R_h). For a true solid sphere, R_h equals the actual radius R. When the object has some other shape, such as cylinder and cube, then R_h is the radius of some hypothetical sphere that diffuses as fast as the measured non-spherical objects do. R_h is determined from the diffusion coefficient D, according to the Stokes-Einstein equation $R_h = kT/6\pi\eta D$, where k is Boltzmann's constant, T is the Kelvin temperature, and η is the solvent viscosity. D is measured by DLS, which measures the intensity autocorrelation function, $g^{(2)}(t)$, of light scattered by the object in solution or suspension. One must extrapolate to zero scattering vector magnitude q. In general, the intensity autocorrelation function is converted to the electric field autocorrelation function, $g^{(1)}(t)$, using Siegert relation $g^{(2)}(t) = B + f\left|g^{(1)}(t)\right|^2$, where B is the baseline, f is the parameter related to coherence. For a single scattering species, $g^{(1)}(t) = e^{-\Gamma t}$ shows a single exponential decay rate Γ. The decay rate is directly proportional to the diffusion coefficient, with a slope equivalent to the square of the magnitude of the scattering vector q^2, $\Gamma = q^2 D$.

First, three H*Protein B aqueous solutions were prepared at 3 mg/mL, 0.3 mg/mL and 0.03 mg/mL. Next, a conventional DLS with rotating-arm allows to measure DLS signal at desired scattering. The H*Protein B may form aggregates by agitating although it does not form micrometer structures, which was not observed from optical microscopy study. The DLS of H*Protein B over time appears in Figure 2.18. The H*protein B aggregates (possibly nanobubbles) indicates polydisperse radii ranging from 100 to 200 nm with respect to scattering angles. The size slightly decreases over aging time for both

0.3 mg/mL and 3 mg/mL samples (Figure 2.18A and B). The lowest concentration of H*Protein B (0.03 mg/mL) shows the opposite trend, in which the aggregates becomes bigger at long time. The results of measurements at 0.03 mg/mL are questionable. One possible explanation could be the active H*Protein B content is even lower (the actual percentage of active content is unknown for H*Protein B). And at such low concentration of H*Protein B (0.03 mg/mL), the amount of H*Protein B aggregates could also be low. Any dust or impurity present in the solution can cause the failure of DLS measurement. Thus the data fluctuates over time and do not indicate a clear trend.
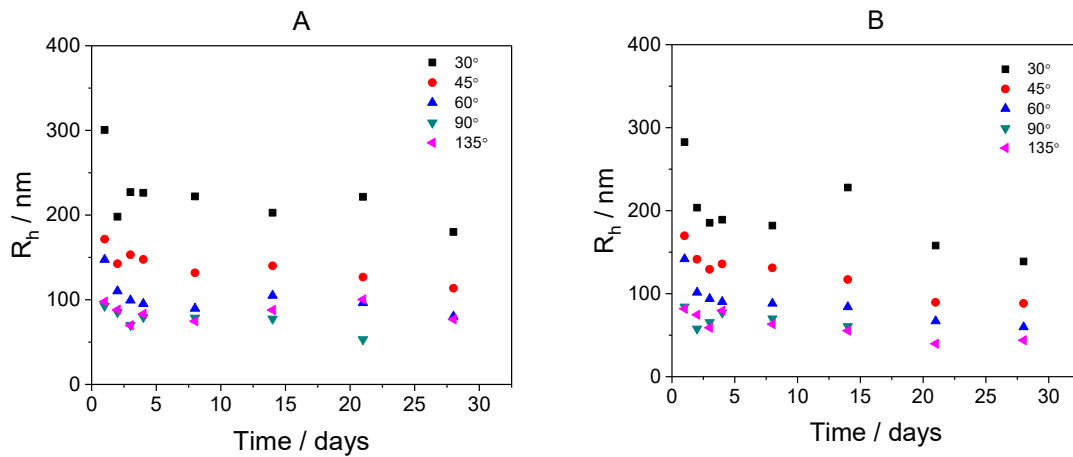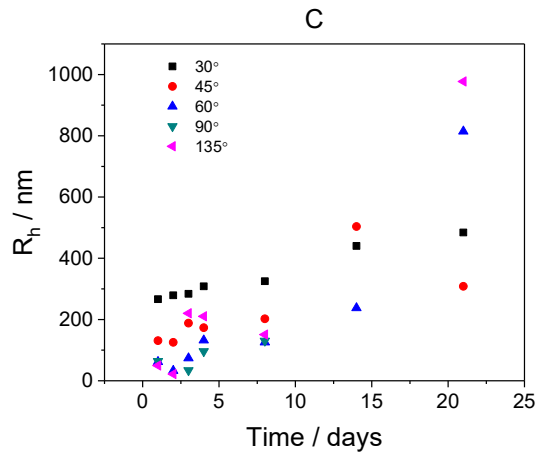
Figure 2.18. Aging time dependence on the aggregates size in H*Protein B aqueous solutions as a function of H*Protein B concentration. (A) 3 mg/mL, (B) 0.3 mg/mL and (C) 0.03 mg/mL. The DLS data were collected from the conventional rotating-arm system.

CU is more likely to form micron-sized air bubbles compared to H*Protein B. The bigger ones rise quickly and smaller remain in the suspension for a long time (28 days). Even the bubbles that remain are large scatterers that should ideally be measured at multiple scattering angles. It is challenging to characterize such a quick-evolving system by collecting DLS at each angle one at a time. Therefore, simultaneous multi-angle multi-correlator dynamic light scattering has the advantage of doing DLS quickly within one minute for multiple scattering angles and has been used to monitor the stability of CU air bubbles as a function of aging time.

In this study, CU solution dispersed in a scintillation vial at a concentration of 0.02 mg/mL was agitated by shaking. DLS measurements were made at different aging time after CU solution being agitated. Typical autocorrelation functions are shown in Figure

2.19 for CU air bubbles suspension. Figure 2.19A and C are in a format of linear y-axes and logarithmic x-axes for 0 h and 3 h dispersion. Several features are directly evident. First, all autocorrelation functions show reasonable single exponential decay patterns at seven different scattering angles, which means all systems have relatively narrow size distributions at each angle. They shift to faster lag time as scattering angle increases because of a small detection volume. Second, all autocorrelation functions shift to faster lag time at 3 h aging time in comparison with those at 0 h aging time. This suggests the air bubbles being measured have become smaller at long aging time. Third, the data quality is greater at the tail of autocorrelation functions with less noise as aging time become longer. This is even more evident in the semi-logarithmic representation, Figure 2.19B and D, which exhibit considerable noise at long lag times. This is because the correlation function approaches zero after baseline subtraction and $\log(0)$ equals $-\infty$. As seen from the smoothly curved semi-log representations, the correlation functions are unimodal, despite the non-uniformity nature of the CU air bubble dispersion. This demonstrates the "invisibility" of the very small objects, such as aggregates or clusters, relative to the scattering from the huge air bubbles. The corresponding decay rates and the polydispersity indices are retrieved from linear slopes and curvatures from the semi-log autocorrelation functions.
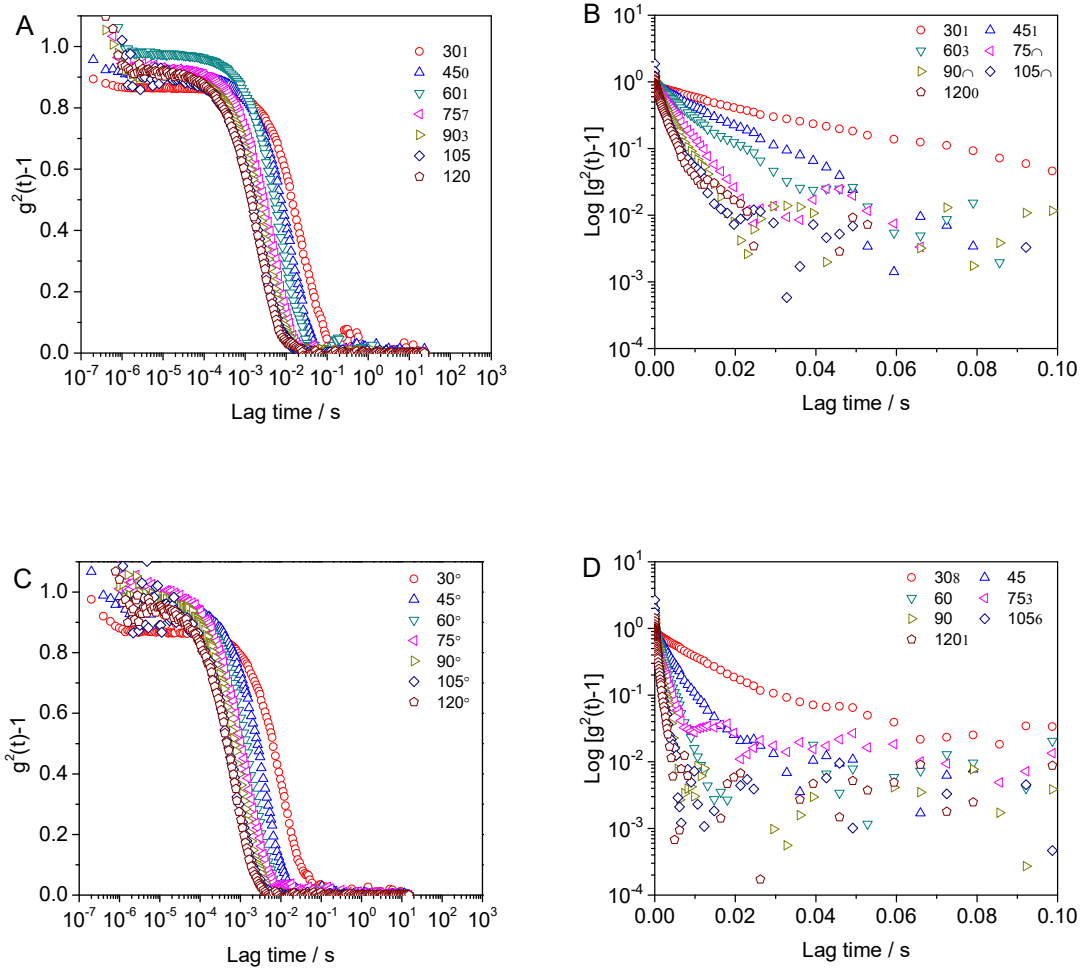
Figure 2.19. Linear-log and log-linear plots of autocorrelation functions for CU air bubbles suspension at 0 h (A and B) and 3 hours (C and D) of aging time. All symbols denoting scattering angles. All measurements were made at room temperature.

One expects a plot of Γ vs q^2 to be linear with a zero intercept and slope D. And this often appears to be the case, the quantity $D_{app} = \Gamma/q^2$ is computed to highlight any deviations. A plot of $D_{app} = \Gamma/q^2$ should be flat. Failure of Γ vs q^2 to rise linearly, or a

slanted $D_{app} = \Gamma/q^2$ plot, indicates particle heterogeneity and/or large particles with a non-spherical shape. This is not evident from DLS results obtained for CU air bubbles at short and long time after agitation shown in Figure 2.20. As can be observed, decay rates at both 0 h and 3 h were proportional to the scattering vector with R^2 of 0.99, as expected for uniformly sized particles. The $D_{app} = \Gamma/q^2$ plots, which are more sensitive than Γ vs q^2 for detecting small deviations from the uniformity, were flat for 0 h. The diffusion coefficient extrapolated to $q = 0$ is D_{app} $(q = 0) = 0.41 \pm 0.02 \times 10^{-8}$ cm^2/s. As shown in Figure 2.20B, the bubbles exhibit correspondingly low linear correlation coefficient, R^2, as expected when the primary plots (Γ vs q^2) pass through the origin with a very high correlation coefficient. The D_{app} vs q^2 plots for 3 h directly indicate fast mode, D_{app} $(q = 0) = 1.33 \pm 0.05 \times 10^{-8}$ cm^2/s. Apparent hydrodynamic radii for air bubbles were calculated from the Stokes-Einstein law (Figure 2.20C). At short aging time, air bubbles have a mean size of 600 nm. Minor size deviation is observed at different scattering angles. Air bubbles are smaller at high scattering angle. Figure 2.20D shows the polydispersity parameter as a function of scattering angle. The high value of polydispersity is not surprising. It could be attributed to the various aspect ratio of the bubbles, which is hard to control during the bubble formation while agitating the CU solution. The rotational diffusion of cylindrical bubbles could also play a role at short aging time, but its contribution is not dominant at long time because the bubbles are prone to monodisperse resulting in the decrease in the slope of μ_2/Γ^2. It is tempting to consider other fitting model, such as CONTIN when μ_2/Γ^2 is greater than 0.3.
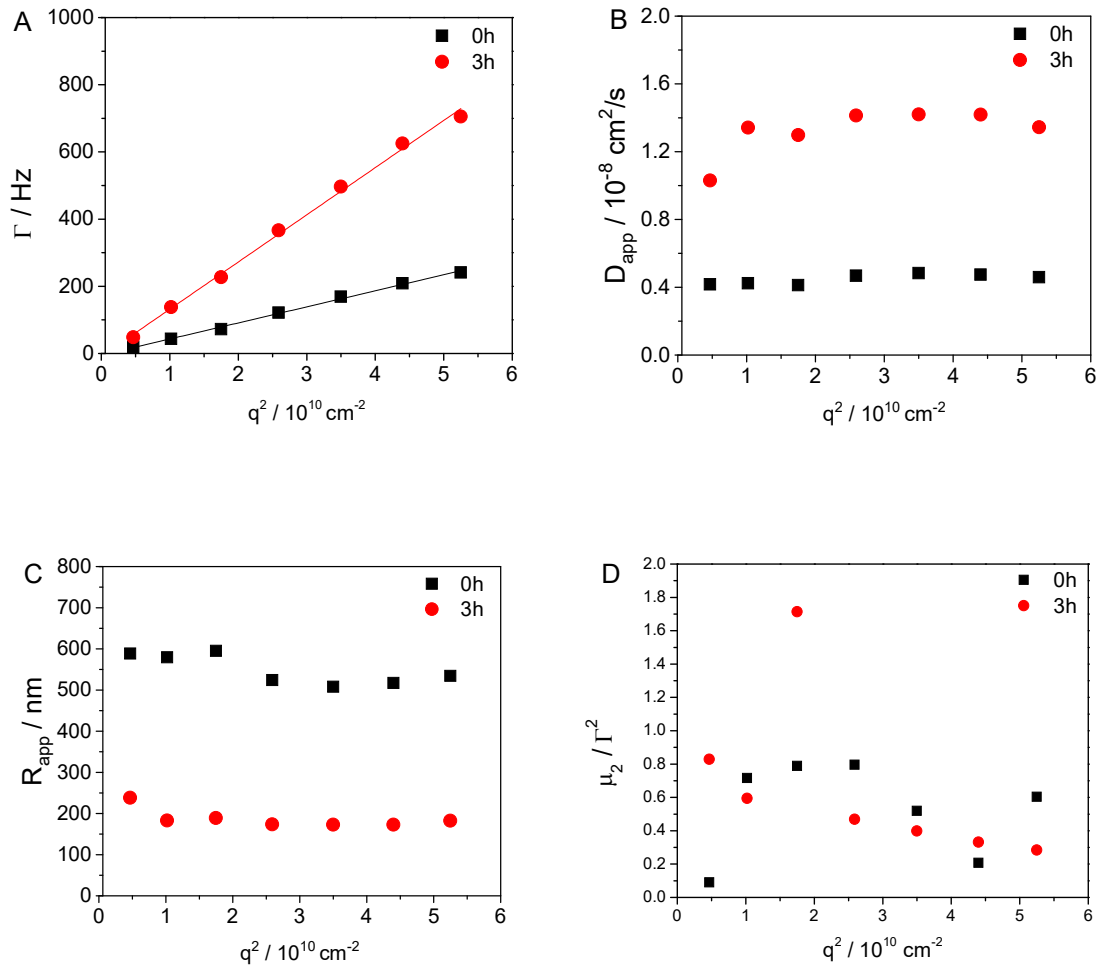
Figure 2.20. (A) Decay rate (Γ) plotted against squared scattering vector (q^2), showing good linear fits for air bubbles at 0 h and 3 h aging time (solid line is line of best fit). (B) Apparent diffusion coefficient (D_{app}) plotted against q^2. (C) Apparent hydrodynamic radius (R_h) plotted against q^2. (D) The polydispersity parameter (μ_2/Γ^2) vs q^2 plots.

Figure 2.21 summarizes the changes in size of air bubbles over time. Bubbles

became smaller with time. Starting at 600 nm, the size and decreased quickly for the first

2 hours and reached a steady value of 200 nm. The value for each angle at each measuring time varied because of the wide size distribution. The trend towards decreased size was reproduced in another run, as shown in Figure 2.22. The measurements were kept for a month this time. The size of the air bubbles became around 100 nm and stayed stable after 28 days. Diluting the original concentration of solution to 10 µg/mL while taking care not to disturb it, the submicron-sized bubble size remained constant. Even after another dilution to 6.7 µg/mL, the size was unchanged. This shows the submicron bubbles are stable to dilution.

These 200 nm large aggregates are submicron bubbles stabilized by a membrane formed by CU hydrophobin aggregates with high elasticity. Deckers and co-workers studied strong interaction between CO_2 and hydrophobin HFBI resulting in formation of stabilized bubbles is required for the beer gushing phenomenon.[103-104] DLS analysis revealed the presence of particles with a diameter of approximately 100 nm in the gushing beer.[105] Although these particles could have been large hydrophobin HFBI assemblies, this is highly unlikely because they would also have been present in noncarbonated beverage, which was not the case for mineral water containing hydrophobin.
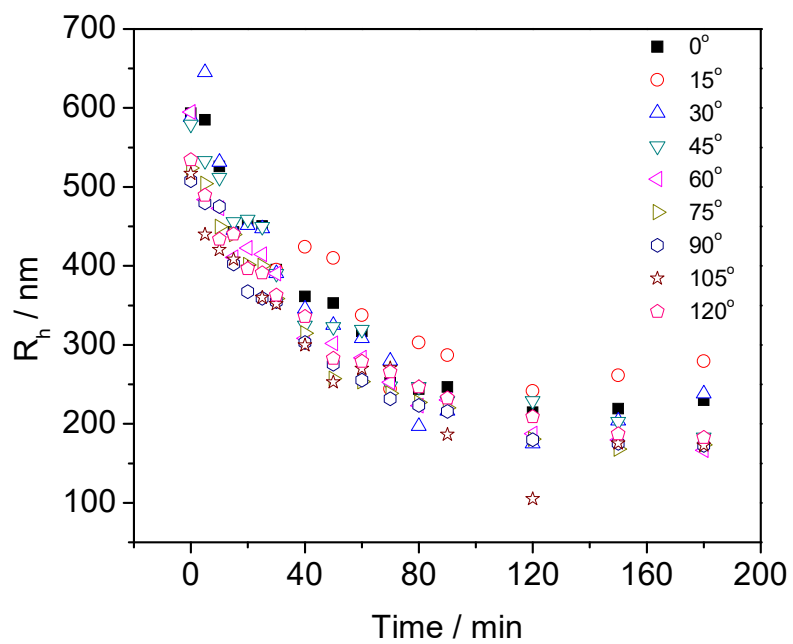
Figure 2.21. Aging time dependence on the size of air bubbles. All open and solid symbols denoting apparent R_h and solid symbols $R_{h(q=0)}$, respectively.
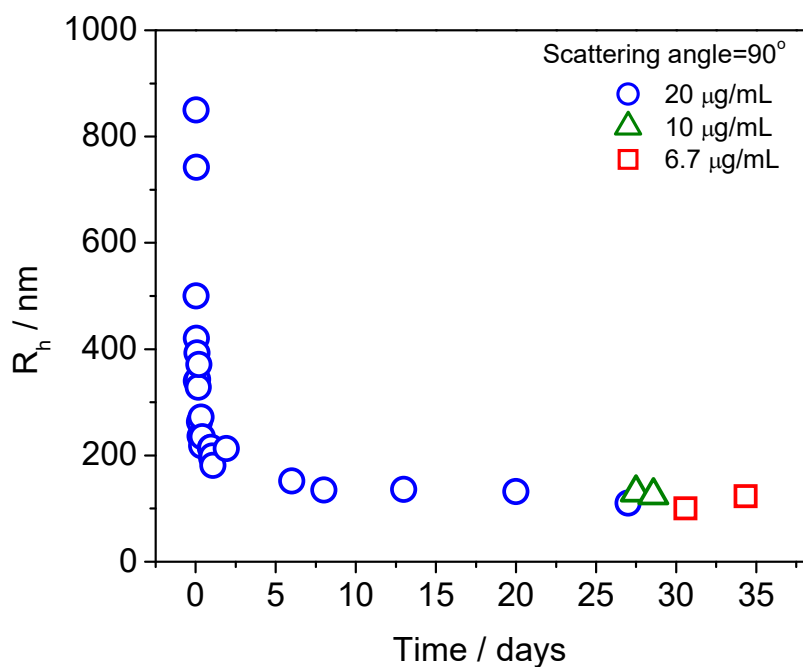
Figure 2.22. Dilution effects on stability of air bubbles at scattering angle of 90°. Triangle and square symbols denote dilution with deionized water to 10 µg/mL and 6.7 µg/mL, respectively.

2.4 Conclusion

Physicochemical properties of two hydrophobins, H*Protein B and *Cerato-ulmin*, have been characterized. In particular, the ability of CU to form non-spherical air bubbles and oil droplets was examined. CU is much more efficient to encapsulate air or oil intro micrometer vesicles. Optical microscopy results show unique structures, such as cylindrical and sausage-like shapes. These non-spherical structures coated by CU were stable and characterized by simultaneous multi-angle multi-correlator DLS and other techniques. The existence of strong membranes of these non-spherical structures led to understand their stiffness and interfacial mechanical properties.

CHAPTER 3.   TOROIDAL MICROBUBBLES STABILIZED BY

CERATO-ULMIN

3.1   Introduction

Bubbles and droplets are often stabilized by films enclosing gases or liquid. They usually adopt a spherical shape in order to minimize surface energy at the liquid/vapor interface.[106] Micron-size bubbles have shown incredible applications in medical imaging as contrast agents.[107] Droplets generated by microfluidic systems have been shown to provide novel solutions to biomedical engineering challenges for advanced diagnostics and therapeutics.[108] These bubbles and droplets are always in equilibrium shape, nominally spheres, but an adsorbed film can stabilize other shapes if it is strong enough. Non-spherical structures are prized for their high surface area relative to volume, and may be exploited for the production of materials for directed strength, acoustic imaging, micro-manufacturing, encapsulation and delivery vehicles, and transport/reaction platforms. Additionally, some shapes, such as torus, offer intriguing topological features.

Subramaniam et al. reported ellipsoidal bubbles created by covering or armoring gas bubbles with a close-packed monolayer of particles and then fusing them.[109] Russo et al. showed that a surface-active protein has been found to generate and stabilize cylindrical and fibrilliform air bubbles by forming a thin monolayer of protein at an air-water interface.[46] Non-spherical liquid droplets can also be achieved by introducing external forces. Cui et al. discovered that applying an electrical field can induce droplet deformation

and self-assembly and jamming of nanoparticles at the interface can remain non-spherical deformation and arrest further shape change.[110] Further examples are provided by generation of toroidal droplets in a viscous liquid[111] and mass production of vortex ring-derived particle through freezing.[112] Other toroidal-like structures have been reported through self-assembly of biomolecules, such as DNA,[113-114] and block copolymers.[115-117] A search for a molecular, rather than particulate, approach to stabilizing non-spherical structures might be expected to begin with small surfactants such as sodium dodecyl sulfate (SDS) or cetyl trimethyl ammonium bromide, but these amphiphiles fail to stabilize non-spherical bubbles. The smallest molecular surfactants capable of supporting stable, non-spherical bubbles seem to be proteins. Johnson and Cooke attributed the crinkling of bubbles in sea water to the adsorption of unknown proteins at the air-water interface.[118] Using a highly purified protein called *Cerato-ulmin* (CU), Miller and co-workers[46] demonstrated not only crinkled bubbles but sub-millimeter cylindrical and fibrilliform bubbles with length:width ratios up to ~35. Their CU protein, excreted from the fungus Ophiostoma ulmi,[2] had been extensively characterized by Richards, Takai and coworkers due to its reported phytotoxicity.[35, 86, 91]

Cerato-ulmin, as a protein surfactant, strongly stabilizes bubbles, foams and emulsions like other hydrophobins do.[50, 119] They can form viscoelastic thin films on oil droplets or air bubbles. For example, Cox et al. reported that non-spherical bubbles stabilized by a hydrophobin from *Trichoderma reesei* can persist for 4 days of storage.[49] Wrinkles appear on the adsorbed surface when the bubbles are under compression.[47] Adsorbed hydrophobin layers can be so robust that alcohols or potent surfactants, such as SDS above its critical micelle concentration,[120] are required to disrupt them. The

dilatational modulus of hydrophobin films well exceeds that of the interfacial layers formed by other common proteins,[75, 102, 121-122] suggesting that these proteins may be able to stabilize even more complex shapes than cylinders or crinkled spheres.

In this chapter, a facile method that takes advantage of CU's robust films was developed to make stable sub-millimeter toroidal bubbles. The structures can exhibit one hole (donut-shaped, genus 1 toroid) or two (button-shaped, genus 2). No special apparatus is required; one merely controls gas pressure above the solution. the possible mechanism of formation of toroidal microbubbles are also discussed.

3.2   Materials and Methods

CU aqueous dispersion at a concentration of 0.2 mg/mL was loaded into a cell constructed of rectangular glass tubing (2 mm ×10 mm), which was connected to a syringe pump (Harvard Apparatus PHD 2000) and a differential pressure meter (Extech, model 407910) as shown in Figure 3.1. Microscopy images and videos were taken by a standard optical microscope (Leica DM2500P) or a Motic inverted microscope with Canon EOS 6D or PCO.edge camera. Z-directional images were obtained using a Nikon A1R confocal microscope, courtesy of Prof. Peter Yunker (Georgia Tech, Physics). Excitation of the sample was achieved by a 488 nm laser.
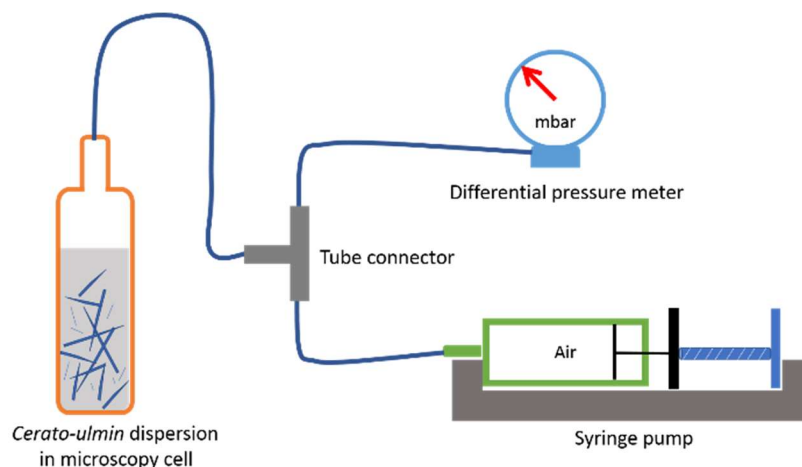
Figure 3.1. A diagram of pressurized system.

3.3 Experimental Results

Agitation of clear CU dispersions resulted in a slightly turbid sample containing abundant cylindrical bubbles (Figure 3.2A and video S2.1 & S3.1 - S3.3). After applying vacuum to the system, the cylindrical structures are in vacuum tension, which causes the larger of them to expand into nominally spherical bubbles (Figure 3.2B). When the tension is subsequently lowered, the surfaces of the spheres start to crinkle and the remaining small cylindrical structures disappear (Figure 3.2C). With application of slight overpressure, the crinkled bubbles tend to become toroidal in shape and retain this shape when returned to the original atmospheric pressure (Figure 3.2D). This sequence of events suggests that the rods are cylindrical air bubbles, as previously identified.[46] The entire process can be repeated many times.
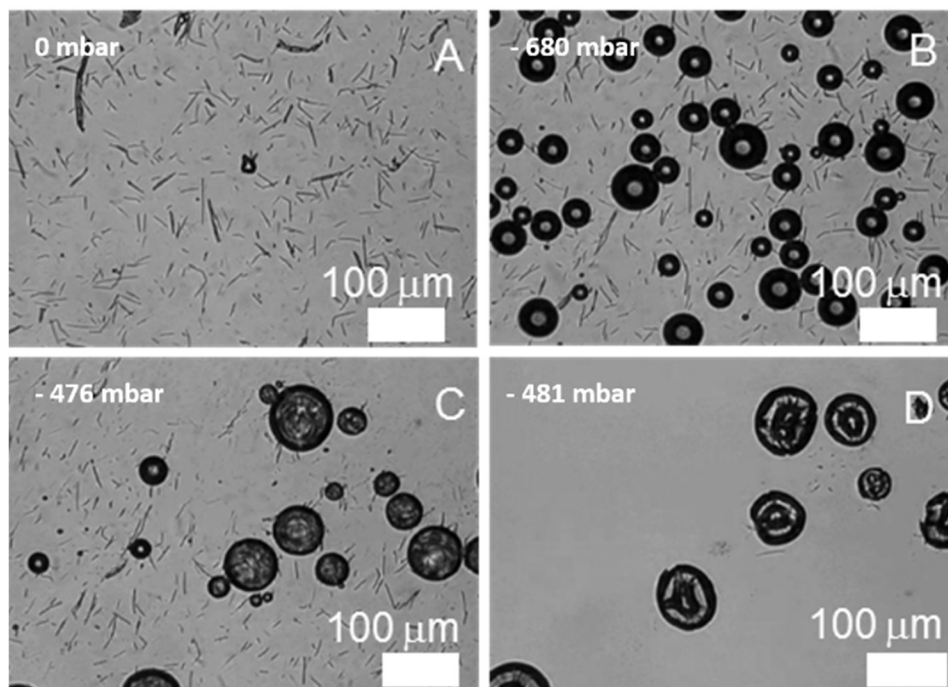
Figure 3.2. A typical process to produce toroidal bubbles. (A) Fibril microstructures from after gently shaking the glass vial containing 0.2 mg/mL CU solution. (B) Spherical bubbles are generated under vacuum. (C) Wrinkles are seen on the surface of spherical bubbles after releasing the vacuum. (D) Applying vacuum to the bubbles induces toroidal bubbles.

Although viewing a simple bubble with improper focus can result in an artefact that resembles a hole, the holes appearing in Figure 3.2 are real. As shown in the videos S3.1 – S3.3 the toroidal shapes of genus 1 and 2 emerge without any change in focus (Figure 3.3A&B). Additionally, Brownian motion of submicron particles shed by the bubbles as they undergo shape changes can be observed through the holes. Static images using dark-field illumination confirms the presence of the toroidal bubbles (Figure 3.3C). Wrinkles appear on the toroid's surface, indicating the formation of CU film.
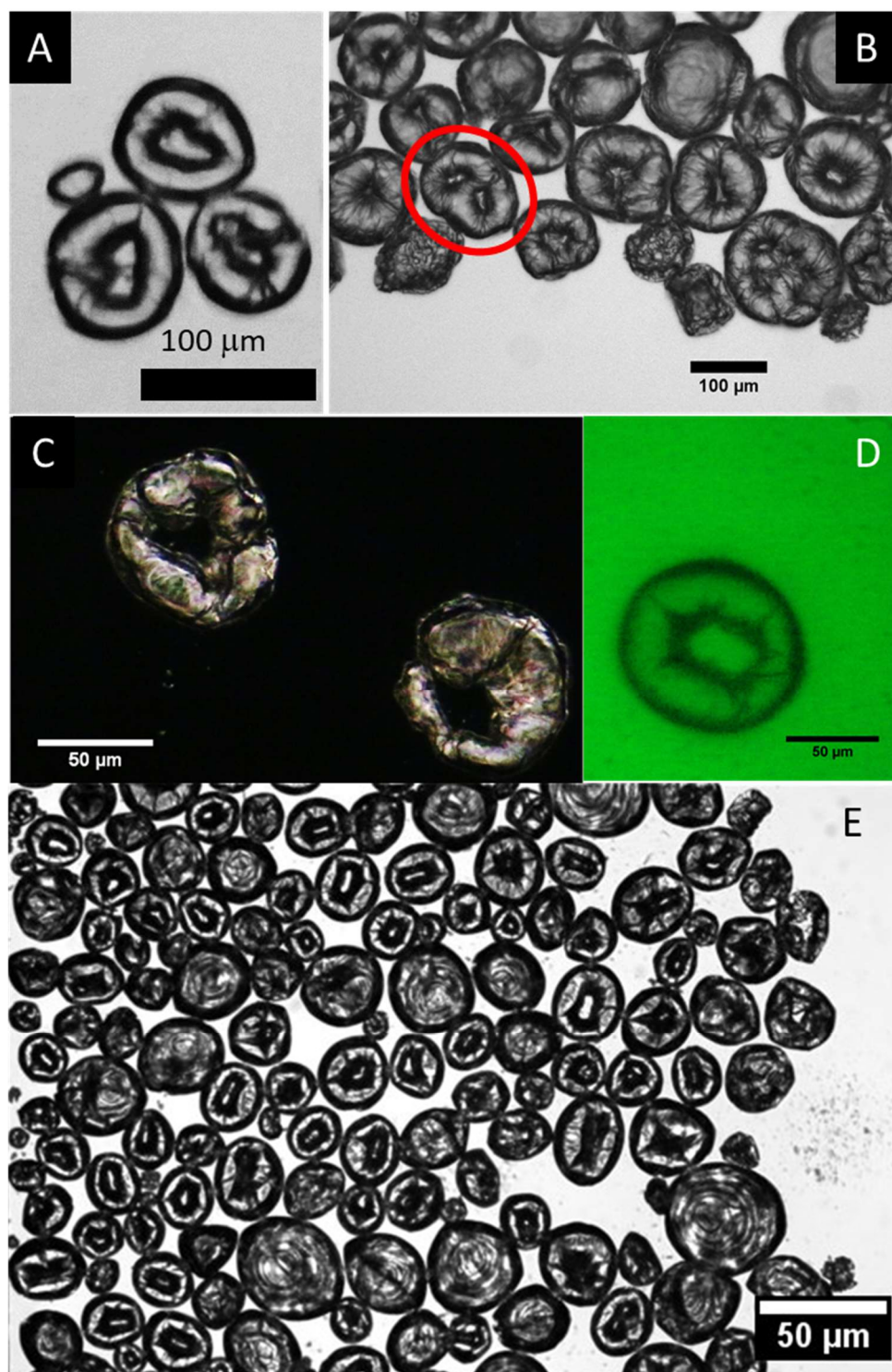
Figure 3.3. Bright-field (A, B and E), dark-field (C) and negative-fluorescent (D) microscope images of toroidal microbubbles with wrinkles stabilized by CU.

A fluorescent dye, 5-(4,6-Dichlorotriazinyl) Aminofluorescein, known as 5-DTAF, was prepared in a carbonate-bicarbonate buffer (pH 9.2) and then used to label CU. Attempts to add 5-DTAF label to CU for fluorescence imaging proved unsuccessful. Instead, free dye (sodium fluorescein) was added to the dispersions (Figure 3.3D). In confocal images, the toroidal bubbles appear dark against a fluorescent solvent (Figure 3.4A). The projected views of bubbles also confirm the formation of torus (Figure 3.4C). As a control, spherical bubbles (Figure 3.4B) do not have holes, and complete spherical structures are generated from their 3D reconstruction. The holes are clearly seen from more confocal z-stack images (Figure 3.5). The toroidal bubbles are stable for at least five days (Figure 3.6).
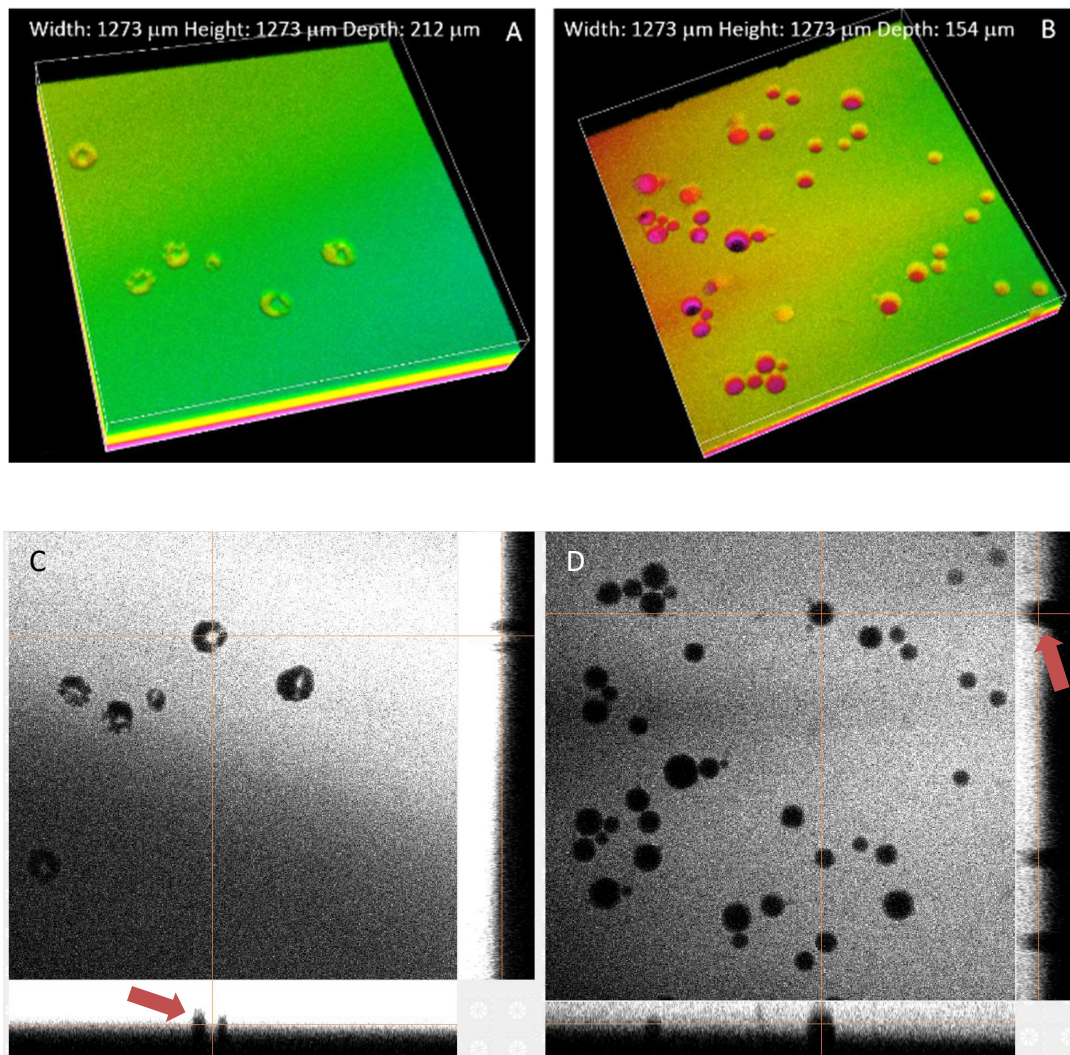
Figure 3.4. Z-stack confocal fluorescent images of toroidal bubbles (A) and spherical bubbles (B). XY (square), XZ (lower rectangle) and YZ (right rectangle) projective views (C and D) of confocal images of toroidal (A) and spherical (B) bubbles. The side-views of a toroidal bubble show two sides of its ring. Side-views of the spherical bubbles show a solid particle. Scale of images is 1273 μm in width, 1273 μm in height, and 212 μm (left) and 154 μm (right) in depth.
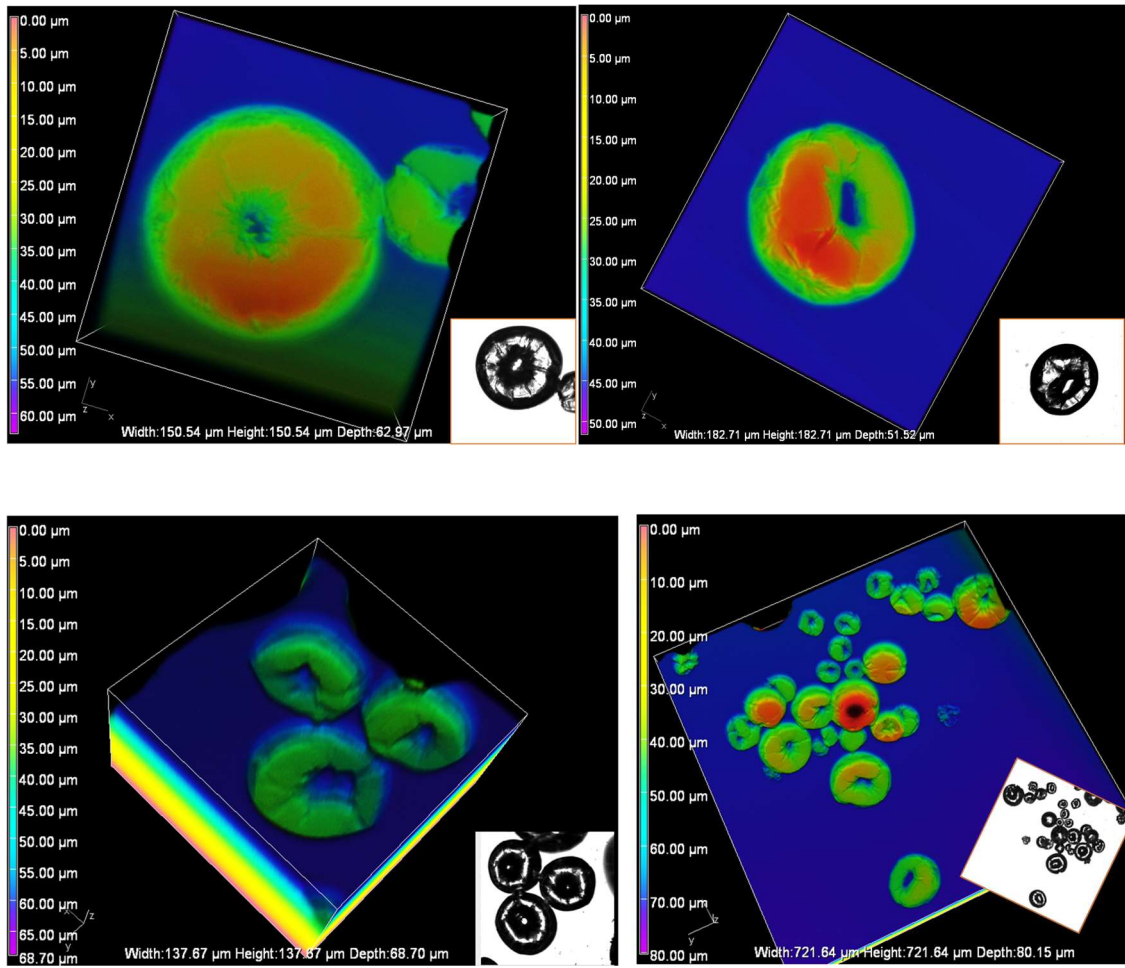
Figure 3.5. Z-stack confocal images of negatively labeled toroidal bubbles. Insets are bright-field microscopic images.
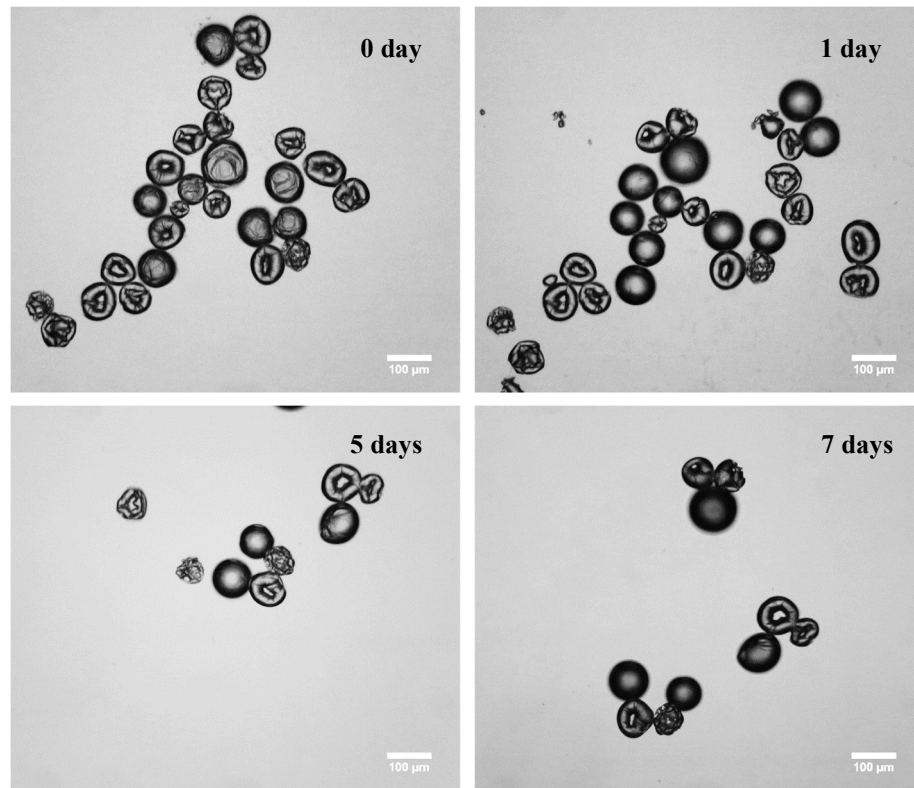
Figure 3.6. The toroidal microbubbles are stable for at least five days (scale bar is 100 μm).

3.4   Discussion

Various processes to form toroidal gas bubbles have been reported.[121, 123, 124] For example, toroidal bubbles were generated by pushing a specially shaped object through water with a laser.[124] Large toroidal bubbles can be generated by injecting air into a fluid, a fact not lost on certain sea mammals, but these bubbles are unstable[125-126] and the turbulent process bears no relation to the slow pressure changes applied here. Squeezing

two particle-armored bubbles between plates resulted in a genus-1 toroid that remained stable after the plates were separated due to the jamming of the colloidal particles on the closed interface.[2]

Here, simply manipulating the pressure in the system has a significant impact on the bubble shapes. Two major shape transitions are involved during the formation of toroidal microbubbles (Figure 3.7). After agitation, the initial CU aqueous dispersion contains cylindrical bubbles with various aspect ratios. Intermediate spherical bubbles are obtained by reducing the pressure above the dispersion. Following with the manipulation of pressure, spherical bubbles transform to toroidal ones. The shape transition between sphere and torus is repeatable and reversible for many times (video S3.4), whereas the transition from cylinder to sphere is irreversible.
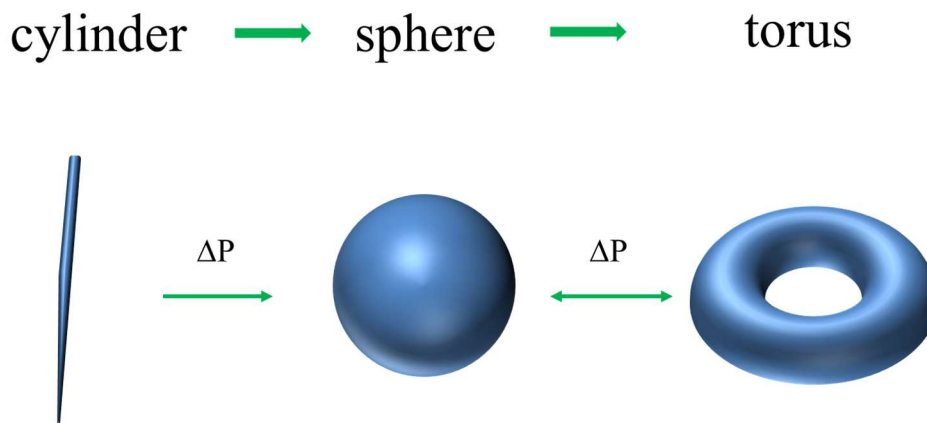
Figure 3.7. A cartoon depicts three air-bubble shapes stabilized by CU through pressure manipulation.

3.4.1   Stage 1: Formation of Cylindrical Bubbles

Formation of air bubbles in CU hydrophobin dispersion, both the micron-sized cylindrical bubbles and spherical ones, is attributed to strong interaction between air gas and CU hydrophobin. The mechanism of formation of air bubbles stabilized by CU hydrophobin is proposed as follow. First, CU hydrophobins are present in the aqueous solution. Air exists above the air-water interface and a tiny amount of air also dissolves in the liquid. Second, the CU hydrophobin molecules migrate to the hydrophilic-hydrophobic liquid-gaseous interface and contact with gas atmosphere due to their amphiphilic property in nature. Then, CU hydrophobin self-assembles at the interface, forming a crystalline-like monolayer[49] when the critical concentration is reached.[18] Applying energy, such as shaking or shearing, will disturb the equilibrium and the hydrophobin films enter the liquid.[85] This results in the attraction between the hydrophilic glass wall of the vial and the hydrophilic part of the hydrophobin layer. The hydrophobic part acts as an anchorage place for the bubbles formation by accumulation of gaseous air molecules.[103] Because of CU's ability to reduce surface tension from 72 to 30 mN/m,[127] and the elasticity of their structure,[102] CU hydrophobins are able to accumulate gaseous air molecules and finally form a stabilized microbubbles and nanobubbles closed by the lateral force. CU films exhibit both fluid and solid interface properties (will be discussed in next chapter), depending on whether CU molecules form a two-dimensional lattice or not. Therefore the Young-Laplace's Law is not applicable to CU membranes but a fluid interface.   A similar mechanism is used to explain formation and stabilization of CO_2 nanobubbles in brewery products (Figure 3.8).[104]
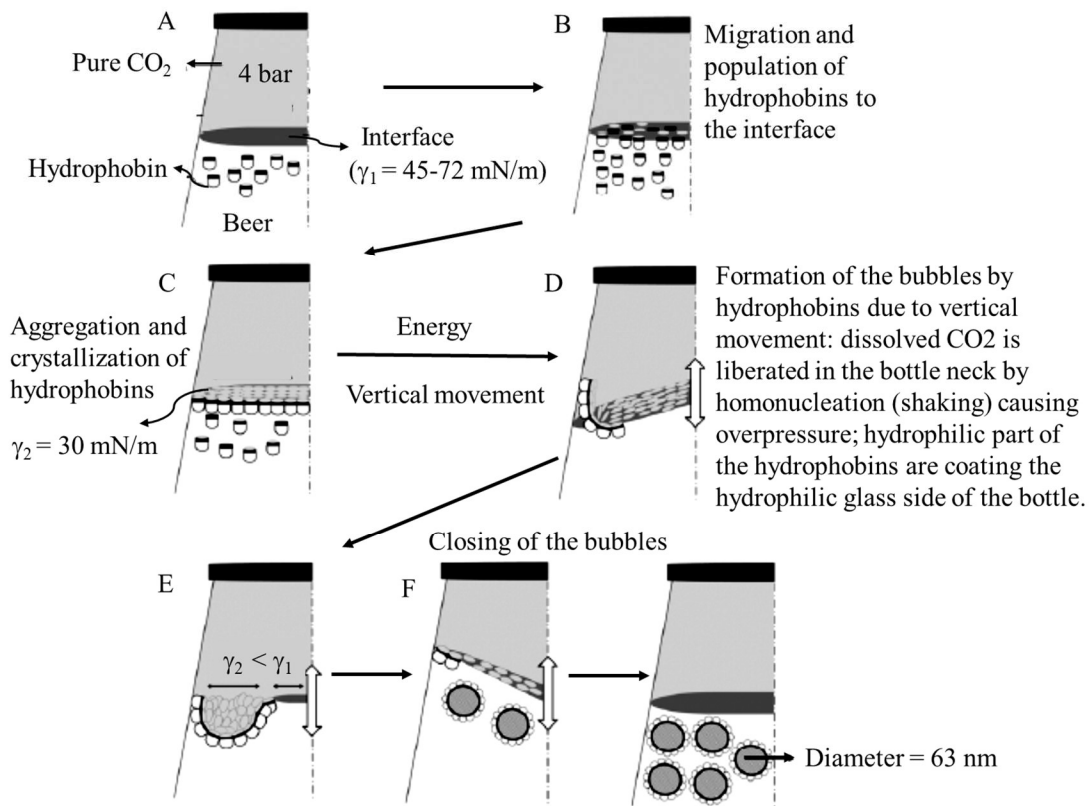
Figure 3.8. Schematic description of the formation and stabilization of CO₂ nanobubble by elasticity of the Class II hydrophobin film in successive phases. (A) Hydrophobins are present in the liquid. (B) Hydrophobins migrate to the interface where they will populate. (C) The concentration/accumulation at the interface results in the formation of the crystalline layer. (D) Disturbance of the equilibrium by energy incorporation. (E) Return to equilibrium by nanobubble formation. (F) Closing of the nanobubbles. Adapted from reference [104].

3.4.2 Stage 2: Cylinder to Sphere

The next stage involving the shape transition from cylinders to spheres is recorded in video S3.5. Figure 3.9 summarizes the shape evolution from cylinder to sphere under the reduction of external pressure. Here, the underlying assumption for the possible mechanism is that the CU hydrophobin is initially at high concentration at the air-water interface rendering a highly viscoelastic surface, *i.e.* high interfacial shear and dilatational moduli. At step A, the cylinder (indicated by arrow) is a smoothly bending rod. By step B, two distinct kinks are visible. These probably signify surface defects. At step C, one of these spawns a spherical nodule. Because the surface is fluid in this vicinity but elsewhere the rod is still a rigid solid. As the nodule grows, it pushes the two stiff ends closer (step D). The pressure in this local region is high since ΔP is inversely proportional to the radius of curvature and hence the defect grows in area. In the local defect, the interface of the defect cap increases, reducing the surface density of CU hydrophobins, thus reducing the effecting surface pressure, and consequently the interfacial moduli. This is based on previously published data of strong coupling interfacial rheology to the surface pressure/surface density of the hydrophobins.[102, 128-129] Because the rest of the cylindrical bubble is stiff, it bends in the opposite direction as the cap inflates. Next, Step E – H is essentially fusion of two of the surfactant interfaces as volume of gas increases inside. Finally, at step I – L, the cylindrical bubble continues inflation, which is similar to the rubber balloon expansion model.[130] This provides a work argument based on difference in local pressures due to two curvatures, since Laplace pressure is inverse to local radius. The bubbles start becoming spherical since the CU is spread over a larger area, and thus low surface pressure, and low modulus can be effectively modelled as a uniform surface

tension. A schematic (Figure 3.10) highlights the major steps of the cylinder-to-sphere transition. Figure 3.11 provides two more examples showing the cylindrical bubbles transform to spherical ones under vacuum tension. Not all the cylindrical bubbles have turned into spheres. That is because some small/thin cylinders may not be perfectly closed bubbles meaning defects or holes are present on their surface and the surface are not fully covered by CU. In other words, the internal pressure inside bubbles are equivalent to external pressure above the dispersion. Application of external pressure change would not introduce pressure difference between inside and outside of bubbles. Therefore, no shape changes occur. Another possibility for some small/thin cylinders to retain their structures would be their stiff and solid-like interfaces. The stiffness and elasticity of the films are attributed to rearrangement of CU molecules at interfaces. The resistance to deformation of cylindrical bubbles may be due to a hampered rearrangements of CU. A certain threshold is believed to exist at where the critical pressure is related to the elasticity of the films. This is might be the case as the interfacial modulus of CU films is discussed in next chapter.
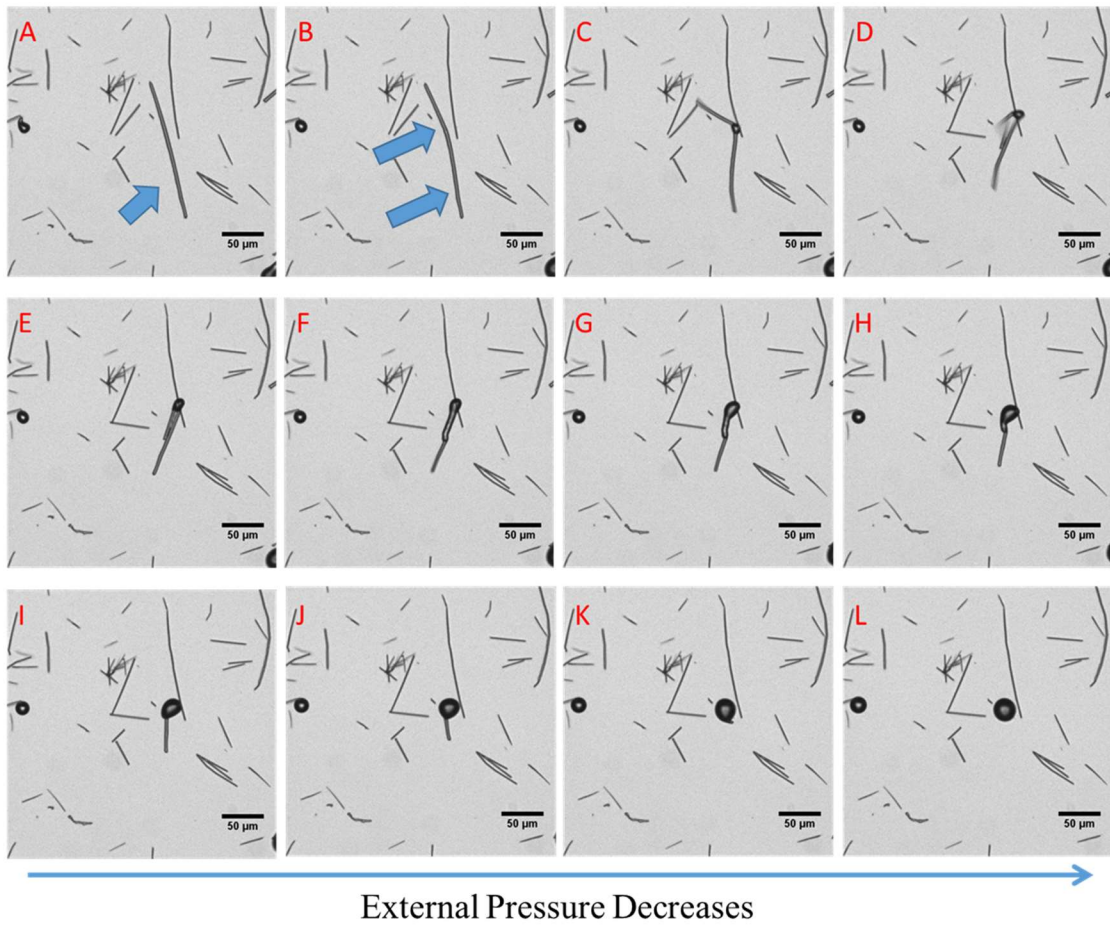
Figure 3.9. Shape evolution of CU bubbles while decreasing external pressure (A to L).
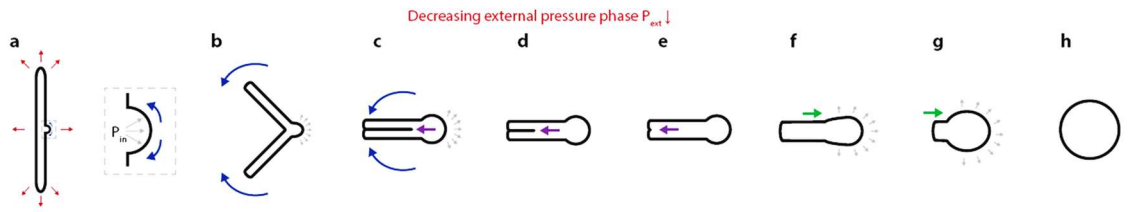
Figure 3.10. Cartoon exhibits the major steps of transition from cylindrical to spherical CU bubbles. (credits to Prof. Saad Bhamla)
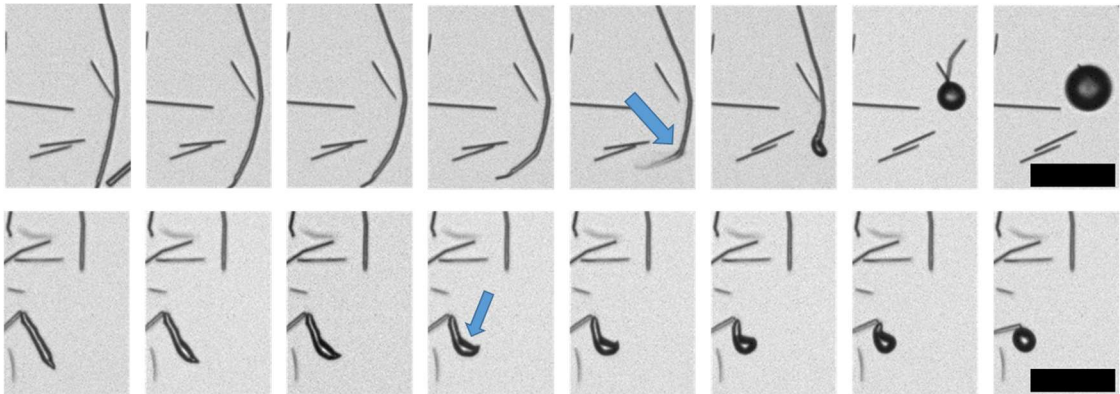
Figure 3.11. Two examples of shape evolution of CU bubbles despite their aspect ratio. Scale bars represent 50 μm.

Cylindrical bubbles are believed to be in a non-equilibrium or metastable state,[131] which is suggested by computing the energy difference ΔE between the free energy E_b of CU molecules integrated at the air-water interface and the free energy E_a of CU molecules

themselves lying in the water (Figure 3.12). Let γ_{GP}, γ_{LP}, and γ_{GL} be the interfacial energies of gas-particle (CU), liquid-particle and gas-liquid. A_{GP}, A_{LP}, and A_{GL} are the surface area correspondingly. R_{CU} and θ_{CU} are the radius of CU molecule and contact angle at interfaces. ϕ is the fraction of surface area CU covers at the air-water interface.
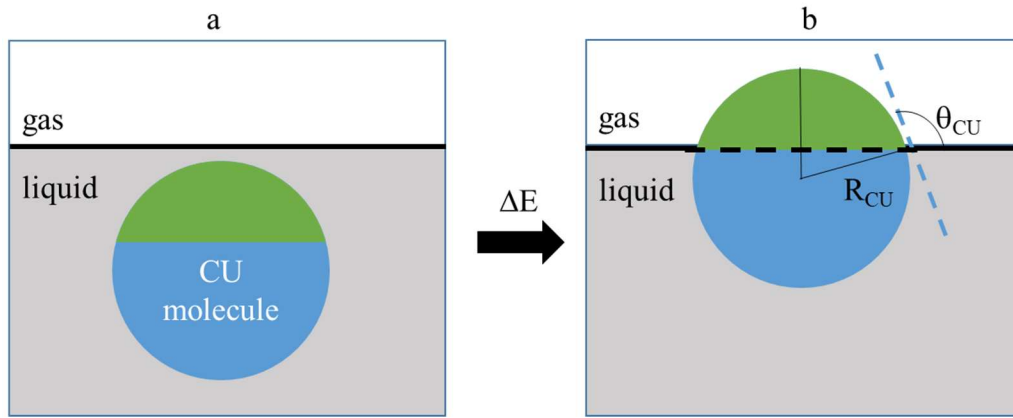
Figure 3.12. Diagram illustrates the migration of a CU hydrophobin molecule lying in the liquid to an extended meniscus.

$$\Delta E = E_b - E_a \tag{3.1}$$

$$E_a = \gamma_{LP} A_{LP}^a = \gamma_{LP} 4\pi R_{CU}^2 \tag{3.2}$$

$$E_b = \gamma_{GP} A_{GP}^b + \gamma_{LP} A_{LP}^b + \gamma_{GL} A_{GL}^b \tag{3.3}$$

$$A_{LP}^b = 2\pi R_{CU}^2 (1 - \cos\theta_{CU}) \tag{3.4}$$

$$A_{GP}^b = 2\pi R_{CU}^2 (1 + \cos\theta_{CU}) \tag{3.5}$$

$$A_{GL}^b = \frac{\pi R_{CU}^2}{\emptyset} - \pi R_{CU}^2 \sin^2\theta_{CU} \tag{3.6}$$

By combining equations above, the energy difference becomes

$$\Delta E = \pi R_{CU}^2 \left(\frac{1}{\emptyset} - (1 - \cos\theta_{CU})^2\right) \tag{3.7}$$

Since $1/\phi > 1$ and $0 \leq (1-\cos\theta_{CU})^2 \leq 1$, therefore ΔE is greater than 0. The positive ΔE indicates the quasi-static transformation of spherical bubbles into non-spherical ones (through migration of CU lying in the water to an extended interface) costs more energy. In other words, a non-spherical bubble is not in the stable state and would return to its least energetic state, *i.e.* spherical armoured bubble.[131] This argument provides the information that cylindrical bubbles are not at equilibrium state from surface energy stand point of view. Application of external energy to the cylindrical bubbles, they are possible and preferred to find its way to return to the least energetic or equilibrium state such as spheres.

3.4.3   Stage 3: Sphere to Toroid

Figure 3.13 and video S3.6 show how application of pressure in a prescribed sequence converts spherical bubbles to air-filled torus. Spherical CU bubbles were pre-generated by applying vacuum to a dispersion of cylindrical bubbles (Figure 3.13A). Releasing the tension atop the dispersion, wrinkles were observed as shown in Figure 3.13B. Further release of vacuum followed by an overpressure, ~ 500 mbar, induced the morphological transitions of spherical bubbles. The membrane exhibits large inward buckling (Figure 3.13C). The bubbles, which are large enough to float to the top of the vial and touch to the glass wall, deformed while deflating. Instead of continuing to increase the pressure, which causes full collapse of membranes and dissolution of the bubbles(discussed in Chapter 5), high pressure was kept for a while and then vacuum was applied to the dispersion again (Figure 3.13D – G). Bubbles are inflated again but in the toroidal shape. Further application of the vacuum results in the formation of spherical bubbles and continued growth in size.
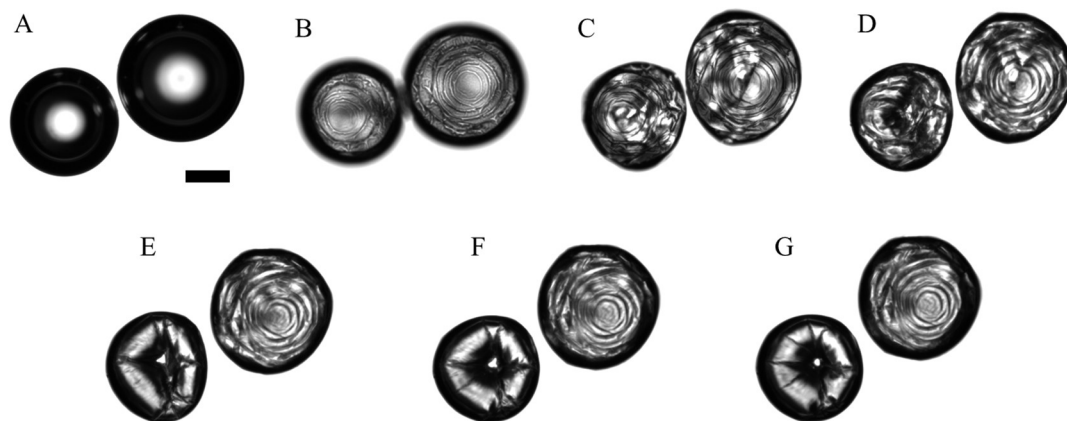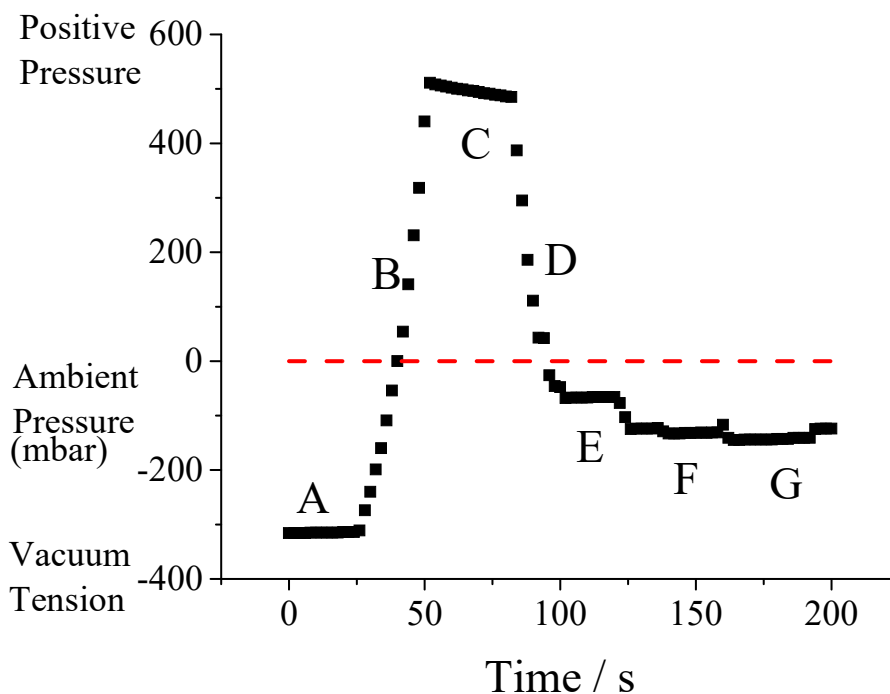
Figure 3.13 Image sequences exhibit formation of toroidal bubbles with pressure profiles. Scale bar represents 50 μm. The dash line denotes the ambient pressure.

3.4.4 Interpretation and Comparison to Liposome and Red Blood Cell

The foregoing is the first description of air-filled submicron torus. Most of what is known about toroidal objects comes from studies of liquid-filled systems. Amphiphilic molecules often assemble into membranes which then form different structures, closed surfaces or vesicles. Two well-known examples are lipid vesicles and red blood cells. Such vesicles have a linear size of the order of 1 - 10 μm and their membranes are in nanometer length scale (e.g. the thickness of the lipid bilayer is about 5 nm.). They exhibit a large

variety of shapes, in particular, non-spherical ones.[132-133] Physical theories have been developed to describe many aspects of membrane conformational behavior, such as the preferred shapes and shapes transformations of their closed vesicles.[134-136] It is believed that the non-spherical shapes of the vesicles or red blood cells are determined primarily by the bending elasticity and curvature.[133, 137-140] Curvature elasticity is not the only factor that controls the shape; the shear elasticity of the membrane is another factor.[133] In the case of red blood cells, the shear elasticity is often neglected because the elastic modulus of shearing is much smaller than that of area dilation. The membrane is considered constant during osmotic swelling or shrinking, which usually takes hours or days to develop the shape.[141-142] The same assumption is also done in the lipid bilayer model. Among the different shapes, such as, budding, discoid, sickle-shaped and etc., Mutz et al. reported the first observation of toroidal topology in partially polymerized diacetylenic phospholipid membranes,[143] which was followed by theoretical studies of toroidal vesicles by other researchers.[144-148] Liposome vesicles and red blood cells do not when first formed, but assume them later to minimize the elastic energy stored in the membrane.

Here, the bending elasticity and curvature theories are applied to CU-coated toroidal microbubbles. The shapes with surface area A and enclosed volume V are determined by a minimization of the shape energy F[133, 138]

$$F = \frac{1}{2}k_c \oint (c_1 + c_2 - c_0)^2 dA + \frac{1}{2}\bar{k}_c c_1 c_2 + \Delta p \int dV + \lambda \oint dA \qquad (3.8)$$

where c_1 and c_2 are the principle curvatures (inverse of its radius), c_0 is the spontaneous curvature, k_c and $\bar{k}_c$ are the mean and Gaussian curvature elastic constants, dA and dV are

the surface area and the volume elements. The first and second terms of Equation 3.8 are the curvature elastic energy of the vesicle membrane. The spontaneous curvature c_0 describes the effect of an asymmetry of the membrane. In other words, for a symmetric membrane, $c_0 = 0$. The Gaussian curvature $c_1 c_2$ is usually omitted, being constant for all shapes under fixed topology conditions. The third and fourth terms take account of the constraints of constant volume and area, where Δp and λ denote the difference between the outside and the inside pressure, and the mechanical lateral tension, respectively. The shapes with lowest energy are among the solutions of Equation 3.9.

$$\delta F = 0 \tag{3.9}$$

Three branches have been reported by solving the equation for axisymmetric shapes, including sickle-shaped, discoid, and the circular torus (Figure 3.14).[145] A detailed phase diagram of toroidal vesicles was predicted.[147]
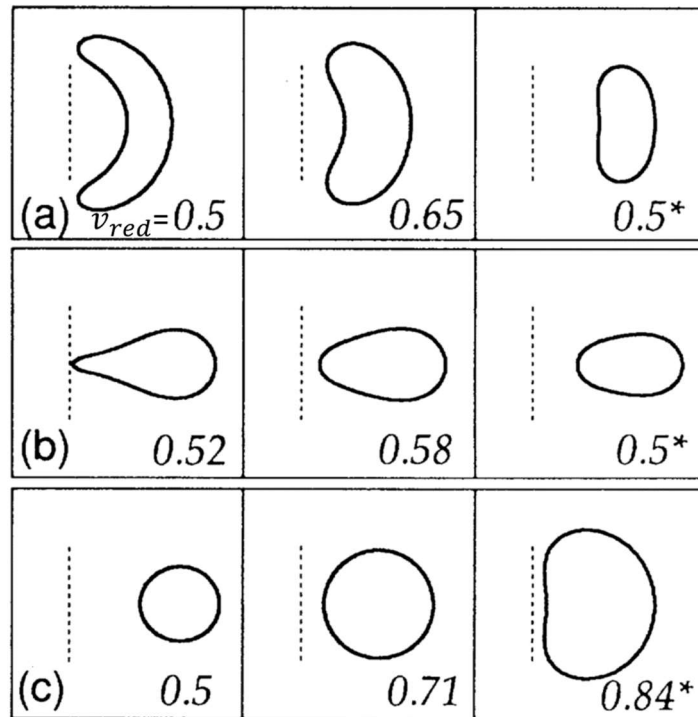
Figure 3.14. Cross sections of sickled-shaped (a), discoid (b), and circular torus (c). [145] **The numbers denote the reduced volume of the toroidal shapes, see equation 3.10. The dashed line represents the axis of symmetry. Shapes marked with an asterisk are unstable.**

A generic circular torus is shown as a 3D model in Figure 3.15A. The red arrow indicates the small ring, sometimes called the handle, and the blue one goes around the big ring. R is the major radius, defined as the distance from the center of the big ring to the center of the small ring, and r is the radius of the small ring or minor radius. The size of the torus hole varies while changing the ratio of R/r, as shown in Figure 3.15C. When R is

greater than r, the structure is called a ring torus or anchor ring. A horn torus is obtained when $R = r$. In the case of $R = 0$, the torus becomes a sphere.
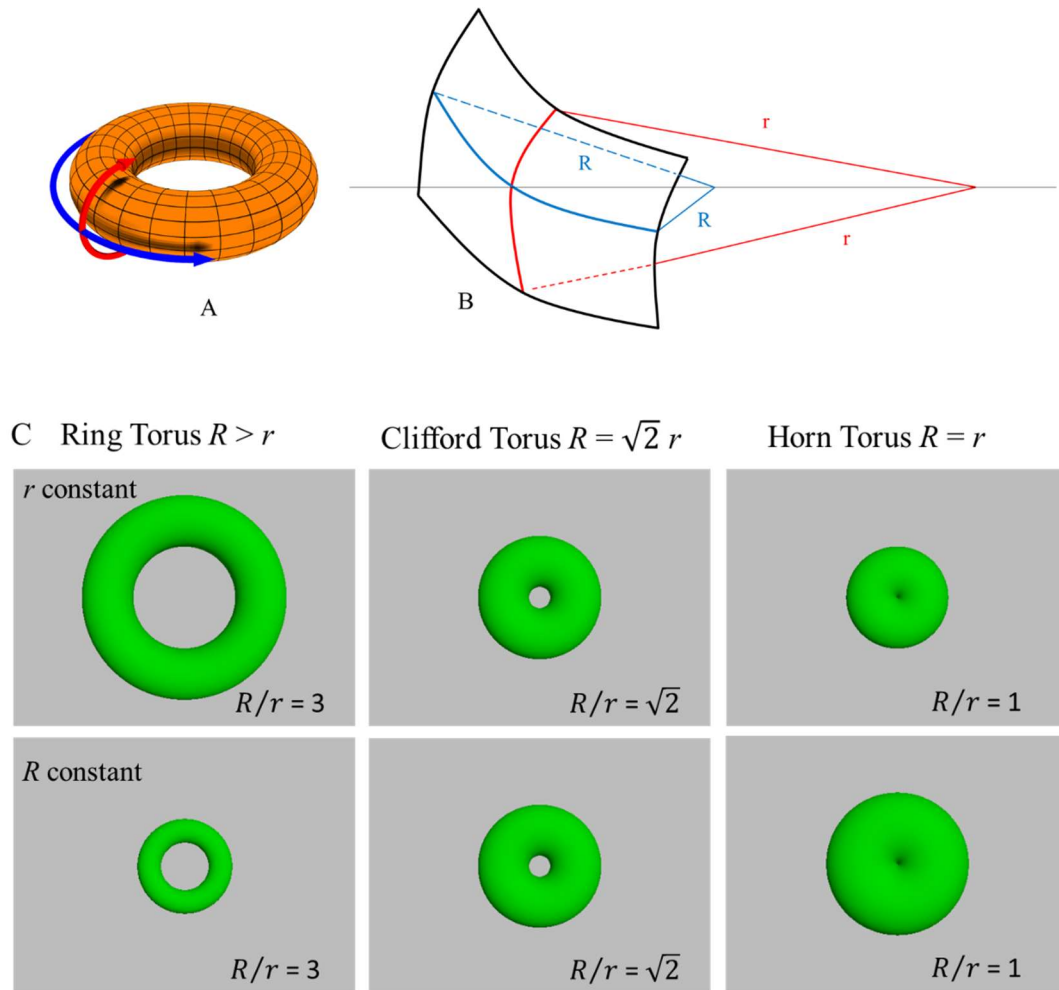
Figure 3.15. An illustration of 3D ring (https://en.wikipedia.org/wiki/Torus) and a section of 2D curved membrane (A&B), which exhibit two curvatures of c_1 and c_2, defined as $1/R$ and $1/r$ respectively. Various tori were drawn by POV-Ray by changing one of the ring radius while holding the other constant(C).

The shape of CU-coated toroidal microbubbles is in agreement with the circular torus, predicted by theories. Ou-Yang et al.[144] first analytically solved Equation 3.9 and predicted the existence of toroidal vesicles whose generating circles have a R/r ratio of $\sqrt{2}$. As shown in Figure 3.16A, these are called Clifford tori. Evaluation of the major (R) and minor (r) radius for 24 individual CU-coated toroidal bubbles allows verification of the predicted ratio of $\sqrt{2}$. The results are shown in Figure 3.16B. The major radius, R, ranges from 20 to 40 μm, whereas the minor radius are in the range of 12 – 30 μm. The ratio of R/r being measured for each torus is aligned on a straight line. The mean ratio of 1.40 ± 0.03 is in good agreement with the theoretical prediction, i.e., $\sqrt{2}$. This result agrees with findings from partially polymerized phospholipid toroidal vesicles.[143]
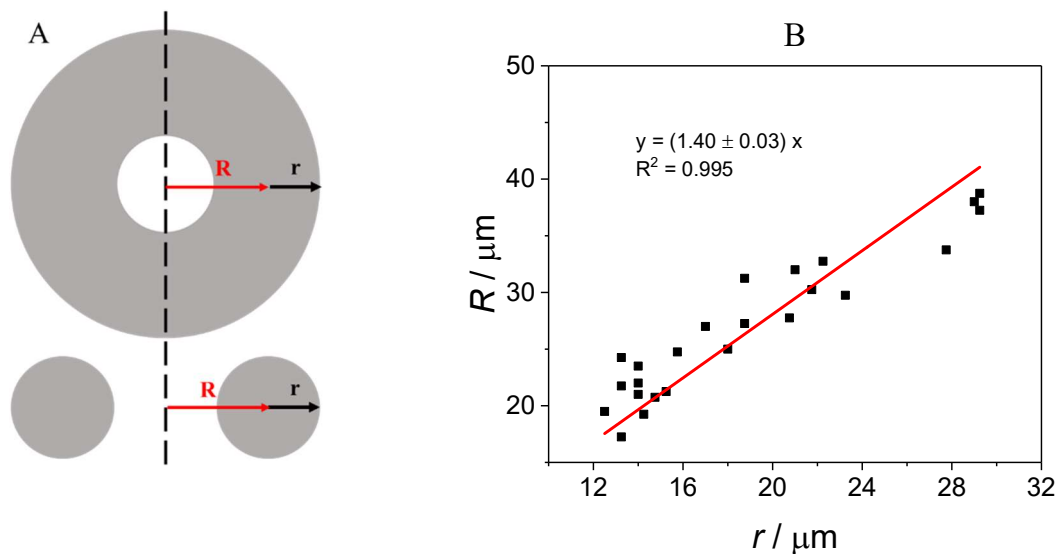
Figure 3.16. (A) Top-view and cross-sectional view of a torus. The major radius (R) and the minor one (r) of each ring, as drawn here, have no particular value. (B) R/r results for 24 individual toroidal bubbles. The solid fitted line represents the theoretical prediction.

The curvature model (the first and second terms from Equation 3.8) are scale invariant, meaning two vesicles have the same bending energy by differing only by their sizes and not by their shape. As a consequence, different shapes exist under toroidal topology. In other words, not all torus are the same. A famous example of this is the coffee-cup-to-donut transformation (https://en.wikipedia.org/wiki/File:Mug_and_Torus_morph.gif). No such extreme examples were observed in this work, but toroidal shapes with the holes shifted away from the center were found (Figure 3.17). These shapes are known as Dupin cyclides. The observation of Dupin cyclide bubbles is also in agreement with both experimental and theoretical studies;[143, 146-147] a significant difference from all previous studies is the air-filled interior in a submicron structure. This feature enables easy manipulation of the shapes by applied gas pressure. Liquid-filled torus are usually manipulated by addition of small-molecule solutes to create an osmotic gradient between the inner compartment and external surroundings.[111, 149-150]
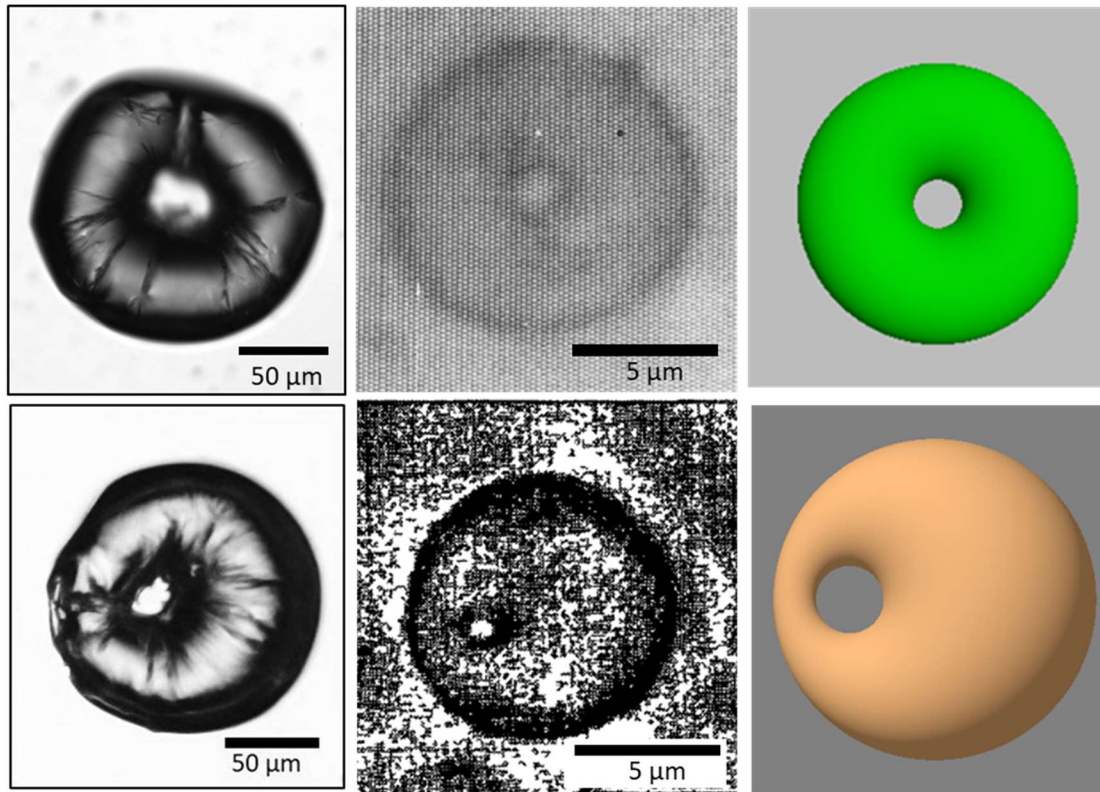
Figure 3.17 A collection of Clifford torus and Dupin cyclides (left column: our CU bubbles, middle column: lipid vesicle[143] and right column: 3D model drawn in POV-Ray).

Due to scale-invariant property, the surface area A and enclosed volume V are no longer important but the system can be described by a single dimensionless term, called reduced volume, which is expressed as

$$v_{red} = \frac{V}{\frac{4\pi}{3}\left(\frac{A}{4\pi}\right)^{\frac{3}{2}}} = 6\sqrt{\pi}\,\frac{V}{A^{\frac{3}{2}}}. \qquad (3.10)$$

The value of the reduced volume varies from 0 to 1. For a sphere, its reduced volume becomes 1, representing the maximum volume enclosed for a given surface area. For bubbles lacking a surface coating, or for those stabilized by a liquid membrane, surface tension often enforces the spherical shape. For the toroidal bubbles observed here, the surface has solid-like character and it may leak gas to the surroundings. Multilayer membranes may stabilize the system (see page 84) and reorganize. Nothing guarantees the system is at equilibrium. Anyway, the shape of torus varies smoothly as a function of the reduced volume. For example, the torus with a R/r of $\sqrt{2}$, a torus known in the mathematical literature as the Clifford torus,[144] has a value of $v_{Cliff} = 3/\left(2^{\frac{5}{4}}\sqrt{\pi}\right) \approx 0.71$. Circular tori are predicted to be stable when $v_{red} < v_{Cliff}$. They are verified to have a reduced volume of 0.66.[144] On the other hand, the reduced volume for an axisymmetric-breaking deformation appears to be $v_{Cliff} < v_{red} < 1$. Another useful parameter is the eccentricity, which is calculated as c/a, where the meaning of parameters a and c is illustrated in Figure 3.18. For the non-axisymmetric circular toroidal bubbles (Dupin cyclides), the eccentricity tells how off-center the structure is. Detailed geometrical parametrization of the Dupin cyclide has appeared in the literature.[148, 151] The reduced volume formula is calculated as a function of eccentricity and its profile is shown inFigure 3.18. The reduced volume increases with an increase in eccentricity. A dozen Dupin cyclide CU bubbles were selected and their eccentricity falls in the range of 0.20 ± 0.03, as indicated by the arrow in Figure 3.18.
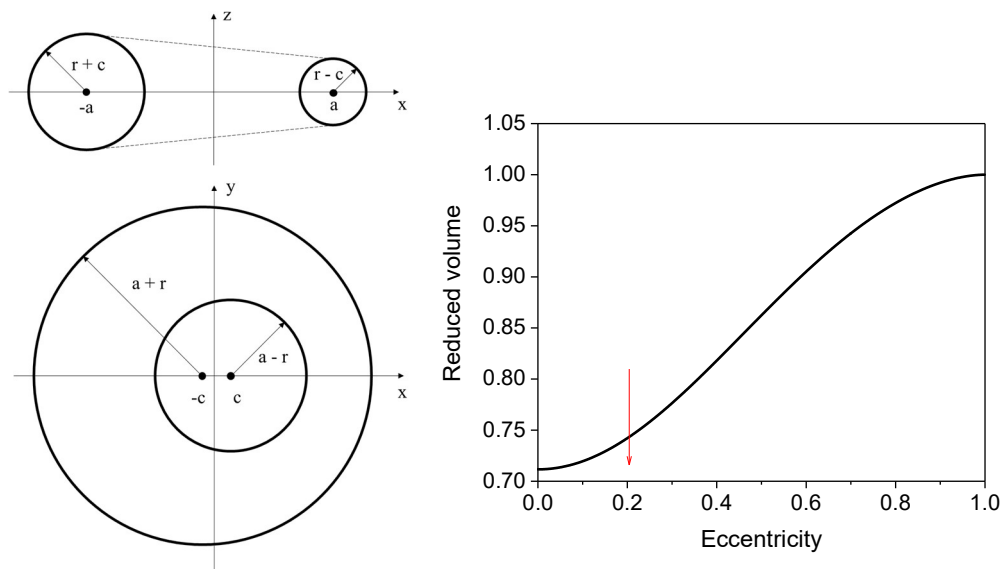
Figure 3.18. Cross section of a Dupin cyclide in its planes of symmetry (left). Theoretical reduced volume profile for non-axisymmetric circular torus as a function of eccentricity (defined by *c/a*) of the torus (right). The red arrow depicts the mean eccentricity of a dozen Dupin cyclide torus.

3.4.5   Other

Particle jamming is known to stabilize liquid-filled droplets of unusual shape, too.[110] In the vesicle community, toroidal and other high-topology shapes have been known for about 25 years.[117, 136, 145-146, 152-157] Their formation from spherical vesicles is described in terms of forces imposed by neighboring particles,[155, 157] by fluctuations that lead to wrapping one end of a cylinder over another permitting the fluid structures to fuse,[154] or by dimpling of a sphere to create opposing concave surfaces that pinch off to leave the toroid.[117]

The formation of CU toroidal gas bubbles seems to resemble this last mechanism, but the diffusion that enables small-molecule amphiphiles to translate along the surface of a liquid vesicle to permit a new shape must be greatly restricted for CU, whose films are known to behave almost as solids.[102] Hydrophobins can be considered rigid Janus-like particles with distinct amphipathic sides;[158-159] they are small but rigid amphiphiles. The reduction of surface tension due to adsorption of CU lowers the energy required to form shapes with a non-minimal surface area, but whether due to the rigid and globular nature of the protein or to specific interactions among proteins, the adsorbed film retains solid-like properties. Compared to traditional armor-coated bubbles, the surface is composed of very fine and possibly somewhat sticky particles. As described by Kam and Rossen, particles on a surface leave bare interfaces,[160] especially if the bubble is expanded under tension and has not yet recruited more particles from the dispersion, but the equilibrium shape remains spherical until the particles come into contact during compression. Thereafter, expulsion of particles (debris, as noted above) and flatter shapes may occur. CU-coated toroidal bubbles are stable for 5 days and do not coalesce on contact, suggesting that if the particles do exhibit specific interactions at all they are of the lateral sort.

3.5   Conclusion

Stable toroidal air bubbles with ~100 μm outer diameters were generated by manipulating the air pressure over aqueous dispersions of the amphiphilic protein *Cerato-ulmin*. Toroid formation is preceded by morphological transitions from cylindrical to

spherical bubbles. The toroidal bubbles are stable for at least five days. After they have finally disappeared, the process to create them can be repeated many times. The same parent dispersion remains active for at least one year. The toroidal bubbles may serve as encapsulation and reaction platforms or as delivery vehicles.

CHAPTER 4. STIFFNESS AND IRREVERSIBILITY OF ADSORBED *CERATO-ULMIN* HYDROPHOBIN MEMBRANES AT AIR-WATER AND OIL-WATER INTERFACES

4.1 Introduction

Proteins and small molecular weight (SMW for simplicity) surfactants play a crucial role in the stabilization of emulsions, foams and gas bubbles.[97, 119, 161-162] Large surface areas exist in such systems. Proteins and small molecular weight surfactants tend to adsorb to the interfaces. Here the interfaces are of the liquid-liquid and gas-liquid types, normally oil-water and air-water interfaces respectively.[163] The stabilization of the emulsion, foams and gas bubbles to some extent depend on the adsorption and desorption behavior of proteins and SMW surfactants at the interfaces during the process and at equilibrium. This is related to some important interfacial features of proteins and SMW surfactants. They are the capability of lowering the interfacial tension and the rate of lowering, the adsorbed amount at the interface, the ability to desorb, the possible conformational changes, and the thickness of the adsorbed layer.[164-165] A variety of methods and techniques can determine these properties. For example, tensile or sessile drop and Brewster angle microscopy approaches can give information about interfacial tension,[76, 121, 166-167] the thickness and adsorbed amount can be determined by ellipsometry,[122, 168] and spectroscopic methods can monitor the conformational changes.[42, 91, 165] The most important property of the interface

is the interfacial rheology, which relates to change in the interfacial tension as the interface deforms. Both static (at equilibrium) and dynamic (in expansion or compression) measurements are approachable.

4.1.1 Interfacial Tension

A surface forms when two phases exist together such as gas-liquid. This surface is held by a force called surface tension. The interfacial tension is similar to surface tension only in the case of two liquid phases. The interfacial tension allows a drop of water to become spheres because it minimizes the surface area to acquire minimum amount of free energy. Thereby the interfacial tension is measured in energy per unit area (J/m^2) or force by length (N/m). The Young-Laplace equation is expressed as,

$$\Delta P = \gamma \left(\frac{1}{R_1} + \frac{1}{R_2} \right) \tag{4.1}$$

where ΔP is the pressure difference across the interface, γ is the interfacial tension and R_1 and R_2 are the principal radii of curvature. In the simple case of capillary forming a spherical curvature, the Young-Laplace equation can be simplified as

$$\Delta P = \frac{2\gamma}{R} \tag{4.2}$$

Here common interfacial tension characterization techniques are discussed in brief. A Langmuir-Blodgett device (see Figure 4.1) is built around a trough made of Teflon which

is filled with water. Two movable barriers sit on top of water. Proteins or surfactants are dissolved in a volatile solvent and placed on the surface of the water between the two barriers. The volatile solvent is allowed to evaporate. When the barriers move closer together water can flow under the barriers but the surfactants remain at the surface. The surface tension is then monitored as a function of surface area at constant temperature to obtain the surface tension-area isotherm.
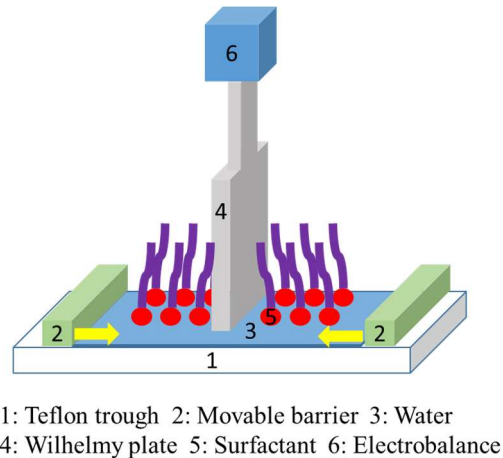
1: Teflon trough 2: Movable barrier 3: Water
4: Wilhelmy plate 5: Surfactant 6: Electrobalance

Figure 4.1. Schematic diagram of Langmuir trough.

Drop volume tensiometer is another way to measure surface tension. A schematic of drop volume method is shown in Figure 4.2. A drop of heavy density liquid (water) is dispensed through a capillary into a surrounding low-density phase (water immiscible oil). The drop is held at the tip due to the interfacial tension. The drop at a certain volume falls

when the separation force due to weight equals to the interfacial tension. At this moment the drop volume is measured and the interfacial tension is calculated.
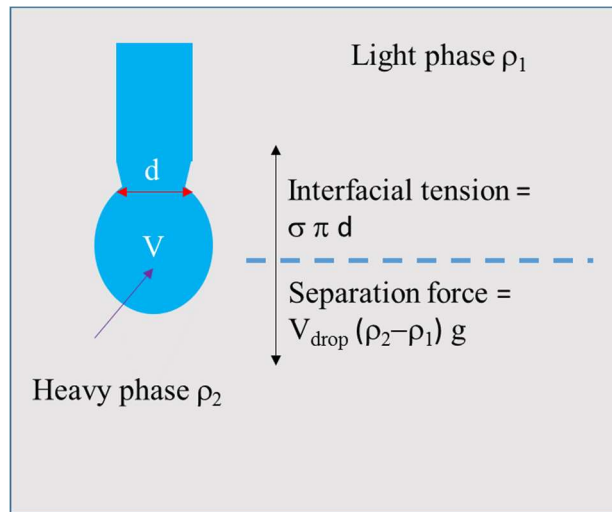
Figure 4.2 Schematic diagram of drop volume method.

Bubble and drop oscillation is another common technique to measure surface tension. In general, a bubble or drop is formed at the tip of capillary inside of surrounding liquid phase (see Figure 4.3). Depending on the density difference between two liquids, the configuration of the drop varies. Pendant and sessile drop are two examples. Such shapes are determined by both gravity force and surface tension. Gravity force tends to elongate or squeeze the drop or bubble whereas the surface tension forces the drop to be spherical. The pressure difference across the liquid-liquid interface, the curvature of the bubble or

drop and their interfacial tension are related to each other as shown by the Young-Laplace equation mentioned above.
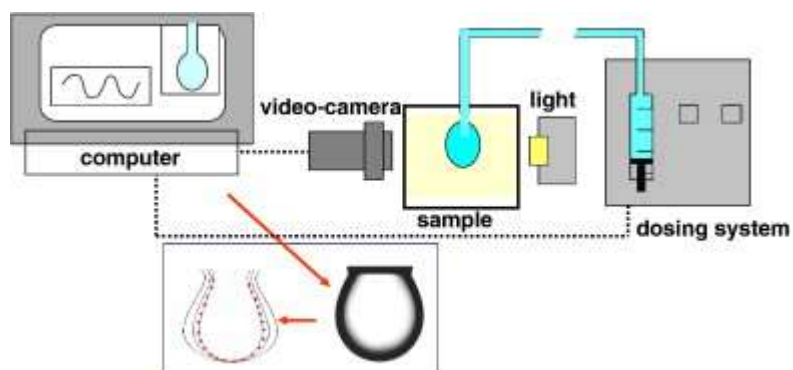
Figure 4.3. Schematic of bubble/drop profile set up.[169]

4.1.2   Interfacial Rheology

Interfacial rheology describes the relationship between the deformed interfaces and corresponding interfacial tension as a function of time.[161, 169-170] Dilatation, shear and bend can cause the deformation of the interfaces. In the dilatational deformation, the interface area is either increased or decreased while the shape of an interface remains the same. When applying shearing to the interface, the interfacial area keeps constant whereas the shape of an interface changes. The example of these two cases is illustrated in Figure 4.4.
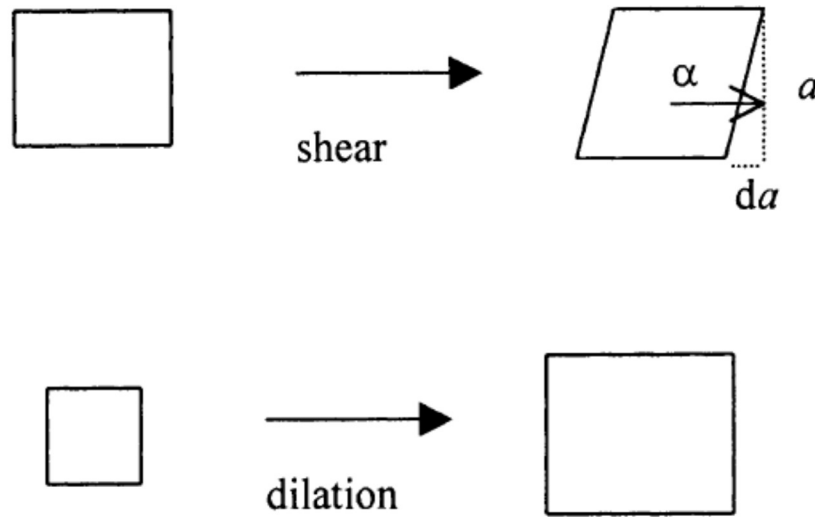
Figure 4.4. An example of 2D shear and dilatational deformation of an interface.

Only the dilatational model is discussed. As the interface is in expanded or compressed motion, the corresponding interfacial rheology is referred to a dynamic characterization. The expansion or compression can be slow or fast. In a dynamic measurement, the interfacial deformation leads to a sinusoidal change in surface tension ($d\gamma$) and a change in surface area. The infinitesimal change in surface area is expressed as

$$\frac{dA}{A} = d \ln A \qquad (4.3)$$

The interfacial dilatational modulus E, is defined by

$$E \equiv |E| = \frac{d\gamma}{d \ln A} \qquad (4.4)$$

The magnitude of interfacial dilatational modulus provides the information about the stiffness of the interface while expanding or compressing. For an elastic-viscous interface, two components can be extracted from interfacial dilatational modulus, which are the interfacial elastic modulus (E', in-phase contribution) and the interfacial viscous modulus (E'', out-of-phase contribution). They can be given as

$$E' = E \cos \delta \,, E'' = E \sin \delta \,, E = E' + iE'' \qquad (4.5)$$

The phase difference between E' and E'' is presented by tan δ, which is described as

$$\tan \delta = \frac{E''}{E'} \qquad (4.6)$$

This is a measure of the elastic vs. viscous behavior of the interface, nominally higher elasticity shows a lower tan δ.

Different techniques such as Langmuir trough, bubble/drop oscillation have been developed to measure the interfacial rheology (Table 4.1).

Table 4.1. Techniques used to measure interfacial rheology.[161, 171]

Interfacial rheology techniques	
Dilatation	Shear
Langmuir trough Ring trough Drop volume tensiometer Bubble/drop oscillation Dynamic light scattering	Langmuir trough Surface shear viscometer

4.1.3   Interfacial Properties of Protein and Small Molecular Weight Surfactants

The surface activity and interfacial properties of proteins and SMW surfactants have been extensively studied (Table 4.2). [96, 161, 170] Proteins are surface-active and show the ability to lower the interfacial tension of the fluid interfaces. Once the proteins absorb at the interfaces, their conformation may change. The protein desorption from the interfaces is often irreversible. The proteins are usually in globular shape. SMW surfactants have a hydrophilic head and hydrophobic tail and no conformational change at the interfaces. SMW surfactants can replace proteins at the interfaces in the case of protein-surfactant complex. This results in the proteins desorption. Proteins can form a viscoelastic film at the interfaces whereas the SMW surfactants cannot. It is found that proteins

adsorption and desorption is slower than SMW surfactants because of their high molecular weight.

Table 4.2. General interfacial properties of proteins and low molecular weight surfactants.[161]

Interfacial properties	LMW surfactants	Proteins
Number of molecules	10^{-5} mol m^{-2}	10^{-7} mol m^{-2}
Adsorbed amount	1.0–2.0 mg m^{-2}	2.0–3.0 mg m^{-2}
Adsorption	Reversible	Practically irreversible
Affinity to an interface	Rather small	Rather high
Molecular shape and size	Cylindrical ($1 \times 1 \times 2$ nm)	Often globular (4–5 nm)
Conformational changes upon adsorption	No	Yes
Film thickness in equilibrium fluid A/W/A^b	40 nm (charged, low I^c) < 40 nm (charged, high I)	4 nm
$\gamma_{equilibrium}$ (mN m^{-1}) at A/W interface	42–22 mN m^{-1}	57–47 mN m^{-1}
Surface tension decrease on adsorption A/W	30–50 mN m^{-1}	15–25 mN m^{-1}
Ability to build up surface tension gradients	Yes	Yes
Value of surface tension gradient	High	Low
Surface dilational modulus	Low	High
Stagnant layer formation	No	Yes
Bubble size distribution in foams	Larger bubbles	Smaller bubbles

^{a}The authors are aware of exceptions on these characteristics. Typical average values are given.
^{b}W = aqeous solution; A = air.
^{c}I = Ionic strength.

4.1.4 Interfacial Rheology Studies of Hydrophobins

Langmuir-Blodgett trough technique has been widely used to examine the adsorption of hydrophobins at hydrophilic-hydrophobic interfaces (normally air-water and oil-water interfaces) as well as interfacial tension in the presence of hydrophobin. The Class II

hydrophobins HFBI and HFBII[41, 172] are particular examples that have been extensively studied. Brewster angle microscopy has also been used to characterize internal tension of HFBI and HFBII.[76, 167] Bubble/drop approach is another way to assess the surface properties of hydrophobins. Lumsdon et al measured the adsorption of HFBII at the air-water and hexane-water interface with a digital video goniometer.[173] Askolin et al. used bubble/drop technique to determine the surface-activity of Class I hydrophobin SC3.[45] They further compared the difference in adsorption behavior of HFBII and SC3, and found the maximal lowering of the water surface tension was obtained instantly or took several minutes in the case of HFBII and HFBI, respectively. In contrast, it took several hours in the case of SC3.[45] Cox et al. determined the surface activity of HFBII at different concentrations.[49] Surface tensiometry data showed that HFBII can reduce the water surface tension to approximately 30 mN/m. The equilibrium surface tension depends on the concentration of hydrophobins. First, the equilibrium surface tension decreases as the concentration of hydrophobins is increased. A break point is reached and surface tension sharply decrease as the surface is saturated with hydrophobins (i.e. the surface saturation concentration, SSC).[18, 49] Further increase in concentration of hydrophobins, the equilibrium surface tension may or may not drop again. Linder et al. reported that the SSC term seems to have no direct connection with the formation of oligomers in solution. Therefore, SSC was suggested to describe the behavior of the hydrophobins better than the critical micelle concentration (CMC).[18, 174]

Hydrophobins are known to stabilize foams and bubbles.[4, 18] Cox et al. reported foams stabilized by Class II hydrophobin HFBII show no significant change in bubble size over 4 months and they are very stable across a wide range of pH conditions.[48] The

exceptional foam stability is due to the adsorption of HFBII to the air-water interface, forming a highly elastic surface and thus preventing the foams from coalescence and disproportion. This is also applied to the air bubbles.[49] The authors measured the interfacial shear elastic modulus and viscous modulus using a Pt-Ir Du Noüy setup. The measured surface shear elastic modulus is in the range of 300 - 400 mN/m,[48-49] which far exceeds that of other typical proteins, about 10 fold higher. For example, the surface elasticity of β-casein and β-lactoglobulin is around 50 mN/m or less.[175] Similar study was explored to show the comparison of stability foams made with HFBII, β-casein or β-lactoglobulin by measuring the differences in surface shear rheological properties.[122] The highly elastic monolayer of HFBII hydrophobin shows wrinkles when it is subjected to compression. Basheva and co-workers measured the average wavelength of the periodic wrinkles ($\lambda = 11.5 \pm 0.1$ μm) and further calculated the bending elasticity (rigidity) of $1.1 \times 10^{-19} J$.[47] The value of bending elasticity from HFBI adsorption monolayer is $7.5 \times 10^{-18} J$ with an average wrinkle wavelength of 33 μm.[176] It seems that for HFBI the bending elasticity is greater than for HFBII, which is 75 times greater. Alexandrov et al. characterized the elasticity of interfacial layers from HFBII hydrophobin by expansion and compression of the protein layers.[121] The dilatational elasticity shows a clear increase trend when the surface pressure is small, corresponding to high surface tension, until it reaches 11 mN/m. At higher surface pressure, the elasticity exhibits the opposite tendency and the data are scattered. The maximum dilatational elasticity from pendant drop method is 300 mN/m at a concentration of 0.002 wt%. This approach is not applicable to hydrophobin solutions because the model fails to fit an irregular drop shape by means of the Laplace equation.[18,]

[121, 176] Other studies on interfacial rheology of hydrophobins layers at air/water interfaces are included reference [129, 168, 177-179]

The interfacial properties of hydrophobins adsorption layers have been studied mostly at the air/water interfaces. There are only a few studies on interfacial rheology at the oil/water interfaces. Radulova et al first reported results on shear rheology of HFBII adsorption layer on oil/water interface, in particular hexadecane and soybean-oil.[180] They found the values of shear elasticity for HFBII layers at hexadecane/water interface and soybean-oil/water interface are 106 mN/m and 148 mN/m, which are lower than for the air/water interface. Richter and co-workers performed studies on the adsorption and interfacial behavior of the Class I hydrophobin H*Protein B at silicon oil/water interface.[181]

In addition to understanding the interfacial behavior of hydrophobin as a single species, studying a binary system containing hydrophobins and other surfactants or proteins are of interest too. The addition of β-casein leads to a rigid HFBII adsorption layer at the air/water interface.[75, 182] The results on high elasticity indicate the formation of an interfacial bilayer consisting of a layer of β-casein towards to water phase and a second layer of HFBII facing to air phase.[182] Blijdenstein et al reported the study of surface dilatational properties of HFBII adsorption layers in the presence of whey protein isolate at air/water interface.[183] They claimed a multi-layer is formed at the interface, where HFBII rich layer is dominant on the top and whey protein is adsorbed on the bottom layer.

The objective of this chapter is to understand the adsorption behavior of CU at both air-water and oil-water interfaces. The surface activity and dilatational moduli of CU at oil-water interfaces were investigated. That analysis, on samples of limited availability,

was made possible using a microtensiometer platform.[184] This fully vetted technique is based on capillary tensiometry and has been used to characterize the dynamics and transport of small molecule surfactants[184-187] as well as the irreversible adsorption and interfacial mechanics of polymeric surfactants,[120, 188-189] polymer grafted nanoparticles,[190] colloidal particles,[191-192] and proteins.[102]

Knowledge of the interaction of hydrophobins with oil in water and hydrophobin membrane's properties is germane to development of environmentally friendly dispersants for oil spill cleanup, and hydrophobins have been interacting with oils from natural seepage for eons. Additionally, the interaction of hydrophobins with organic molecules offers new opportunities in materials science. For example, CU membranes have been used to stabilize latex-like aqueous dispersions of semiconducting polymer solutions in organic solvents.[193] The oil being used is squalane (2,6,10,15,19,23-hexamethyltetracosane), which is a branched alkane with a melting point (-38 °C) well below the temperature range of interest for potential CU applications and with no measurable partitioning into water. Characterization of the progression and reversibility of membrane formation in the absence of competing surfactants was performed using dynamic and static measurements. Switching to mechanical (oscillatory) measurements, CU membranes were observed to grow quite strong, whether at oil-water or air-water interfaces. The study was extended to investigate how CU behaves at air interfaces in the presence of competitive surfactants.[102]

The organization of the remainder of the chapter is as follows. After describing the experimental methods, the behavior of CU at the air-water interfaces are discussed. Then the main topic, the results of CU at oil-water interfaces, are addressed. These observations

suggest circular dichroism (CD) measurements to probe CU's secondary structure, especially changes that may be induced by surface adsorption.

4.2   Materials and Methods

Cerato-ulmin was a gift from Dr. Wayne Richards of the Canadian Forest Service. It was produced by an aggressive strain of *C. ulmi* (RDT2) and purified by the methods of Takai and Richards[86] and Stevenson et *al*.[87] The purified sample was stored in a sealed vial and placed in a jar filled with Drierite® ($CaSO_4$) at ambient temperature and pressure. The water used to prepare CU aqueous stock solutions was supplied by a Barnstead Nanopure® purification system. A stock solution of CU was prepared at a concentration of 20 μg/mL. As a simple confirmation of potency, exposing glass and poly(tetrafluroroethylene) (Teflon) surfaces to CU, even at this low concentration, altered the water contact angle (See Chapter 2, Fig. 2.8).

Squalane was purified by gravity filtration through a glass column packed with 1.5 g of basic alumina. The filter medium was held in place with a slug of 400 μm silica beads purchased from OPS Diagnostics, LLC, Lebanon, NJ.[188]

The surface tension measurements were carried out using a microtensiometer design based on a capillary tensiometer (Figure 4.5). Because the apparatus has been described previously,[184] here a brief summary will suffice. Bulk solution is placed into the ~3 mL solution well (A) which is fabricated from cross-linked polydimethylsiloxane (PDMS). The solution chamber is open at the top and sealed by a No. 1 cover slip at the bottom. A glass capillary (E) is inserted from one side of the chamber and connected with a pressure

transducer (B) through polyethylene tubing. The capillary is extended to make a 35 - 38 μm tip using a capillary puller (Micro Data Instrument Inc., South Plainfield, NJ). An air bubble or oil drop is formed at the end of the capillary tip using a constant pressure head (C). The pressure is generated using a column of water attached to a three-way solenoid valve. An inverted light microscope and a camera are used to image the bubble or drop. The images are captured using a LabVIEW code. The radius of the bubble or drop is analyzed in real time by fitting a circle to images and extracting the radius, $R(t)$, of the spherical cap. The surface tension $\gamma(t)$ is calculated from the Laplace equation,

$$\gamma(t) = \frac{R(t)(P(t) - P_H)}{2} \tag{4.7}$$

where $P(t)$ is the pressure behind the fluid slug inside the capillary and P_H is the hydrostatic pressure of the aqueous solution at the capillary. The difference $P(t) - P_H$ is then the pressure jump across the hemispherical cap trapped at the end of the capillary. Rinsing the bulk solution with deionized water is achieved via the dilution/exchange bath valve (D) and peristaltic pump. The residence time of the reservoir is on the order of tens of seconds.

To determine the dilatational modulus, a reciprocating pump generates periodic pressure fluctuations to expand and contract a single bubble or drop. A low-amplitude pressure (400 Pa) oscillation is imposed at a frequency of 1.9 rad/s, and the response in the radius is measured. For an air bubble or oil drop, the dilatational modulus E is expressed as,[188]

$$E = \frac{dP^S}{d \ln A} \tag{4.8}$$

where P^S is the surface excess normal stress and A is the surface area of the spherical cap. The magnitude of the complex dilatational modulus can be calculated from the pressure and radius measurements as

$$|E^*| = \frac{b_1}{1 - b_1} \left(\frac{R_{eq}}{\Delta R_1} \right) \left(\frac{P_a R_{eq}}{2} \right) \sqrt{\left(\frac{\Delta R_1}{R_{eq}} \right)^2 + 2 \left(\frac{\Delta R_1}{R_{eq}} \right) \cos \emptyset_{R1} + 1} \tag{4.9}$$

where $b_1 = \sqrt{1 - \left(\frac{R_c}{R_{eq}} \right)^2}$ and $\Delta R_1 = \frac{P_{eq} R_a}{R_{eq}}$. P_{eq} is the equilibrium pressure, R_{eq} is the equilibrium radius, P_a is the amplitude of the pressure oscillations, R_a is the amplitude of the radial oscillations, R_c is the capillary radius, and ϕ_{R1} is the phase angle of the radial oscillations.[194] The oscillatory data are processed using a fast Fourier transform in MATLAB to find the frequency, amplitude, and phase angle of the pressure oscillation and resulting radius oscillation signals. All reported modulus values were obtained in the linear limit of small-amplitude oscillations, verified by the absence of harmonics in the radius oscillations.
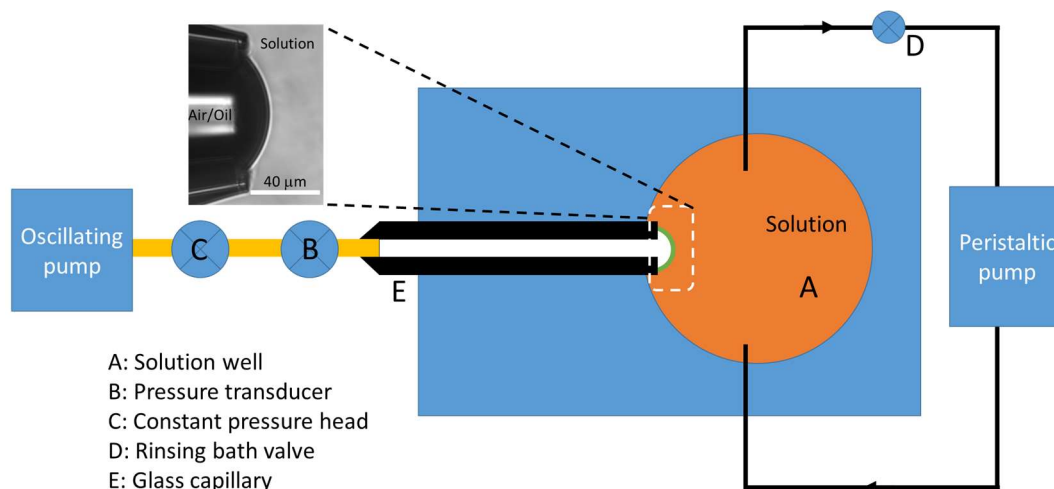
Figure 4.5 Schematic of the microtensiometer apparatus (top view, not to scale, adapted from Reference 38).

Circular dichroism spectroscopy was performed to monitor possible secondary structural changes of *Cerato-ulmin* as a function of concentration as well as in the presence of alcohol. CD spectra of the hydrophobin solutions were acquired with a Jasco 810 spectrometer at 20 °C. A rectangular quartz cell with 1 mm path length was used. The wavelength range was selected from 250 to 190 nm with a stepwidth of 1 nm and a bandwidth of 1 nm. The scan rate was set at 200 nm/min. The CD signals of the water background were subtracted. The data are averaged over three scans without smoothing.

Contact angle measurements were measured on a 2 µL *Cerato-ulmin* solution droplet under ambient conditions. The sessile drop technique was employed using a Rame-Hart goniometer coupled with DROP-image software. The static contact angle was averaged from three measurements at different locations for both Teflon and glass substrates.

4.3   Results and Discussion

4.3.1   Air-water Interface

The result of how CU behaves at the air-water interface has been published.[102] Given sufficient time to develop, CU forms solid-like films with very high dilatational moduli of at least 500 mN/m, accompanied by surface pressures of approximately 15 - 22 mN/m at 2 µg/mL bulk CU concentration (Figure 4.6). The CU films were irreversibly adsorbed (stable towards rinsing with water). Once a rigid hydrophobin film forms, the interface becomes incompressible. Figure 4.7 shows the pressure and radius of a rigidified film during a compression experiment. The pressure is reduced at a constant rate of 11.3 Pa/sec with a syringe pump, but the radius does not respond to the changing pressure. At 180 seconds, near a pressure of 100 Pa, the film buckles and collapses.
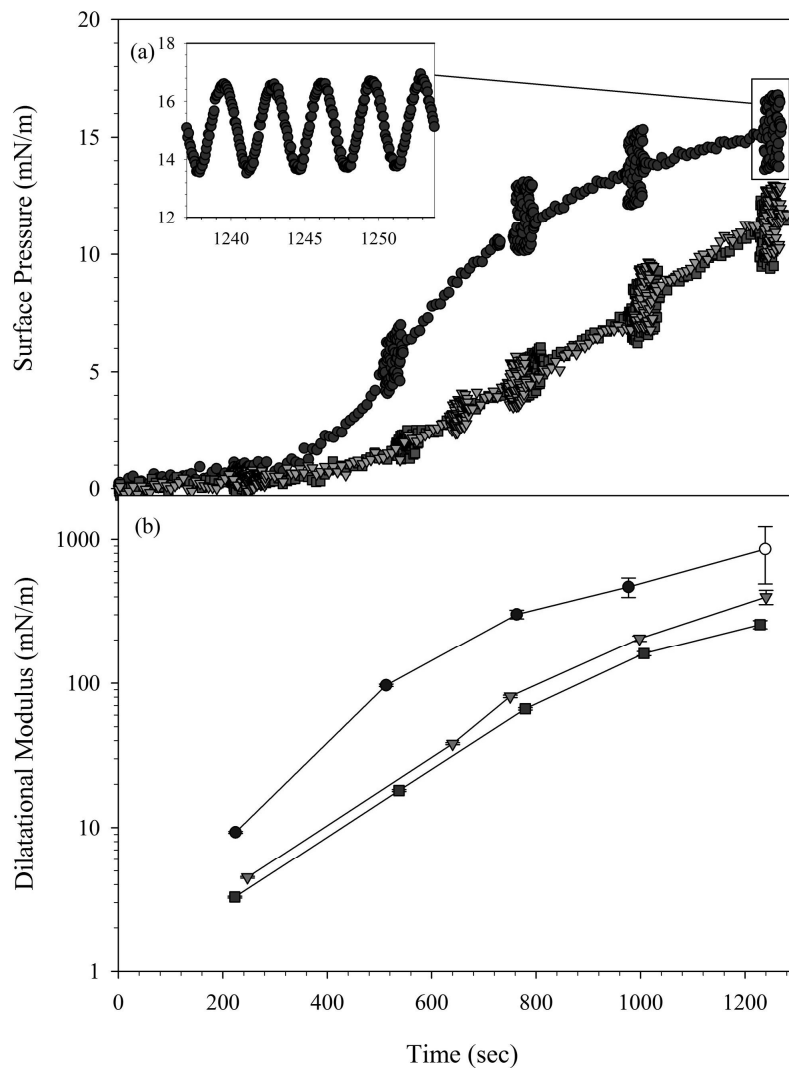
Figure 4.6. (a) Dynamic surface pressure and (b) dilatational modulus as a function of time for three sequential adsorption experiments of a 0.002 mg/mL solution of Cerato-ulmin at an air/water interface: immediately after pouring the sample into the reservoir (circle data points), a reservoir residence time of 1500 seconds (triangles), and a residence time of 3000 seconds (squares). Vertical "bars" in (a) indicate pressure oscillations to measure the dilatational modulus shown in (b). The inset shows the oscillations in surface pressure resulting from the imposed pressure oscillations. Lines are added in (b) to guide the eye.[102]
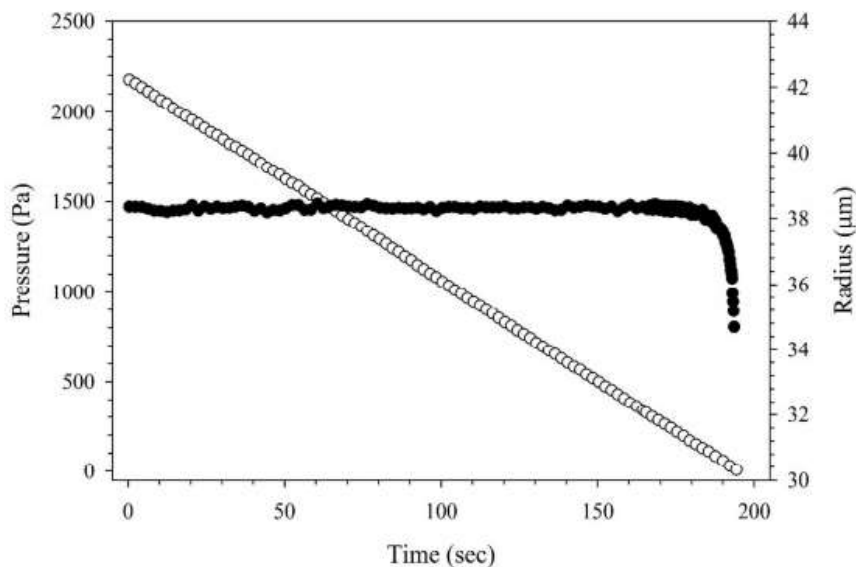
Figure 4.7. Pressure (open symbol) and radius (solid symbol) as a function of time during a compression experiment after the formation of a rigid CU film. The pressure is reduced at a steady rate of 11.3 Pa/sec. There is no change in the measured radius until the film buckles and collapses, at 180 seconds.[102]

Sequential addition of a competing surfactant, sodium dodecyl sulfate (SDS), further increased the surface pressure while reducing the dilatational modulus. Only at high SDS concentrations was CU removed from the interface. That analysis, on samples of limited availability, was made possible using a microtensiometer platform.[184] This fully vetted technique is based on capillary tenisometry and has been used to characterize the dynamics and transport of small molecule surfactants[184-187] as well as the irreversible adsorption and interfacial mechanics of polymeric surfactants,[120, 188-189] polymer grafted nanoparticles,[190] colloidal particles,[191-192] and proteins.[102]
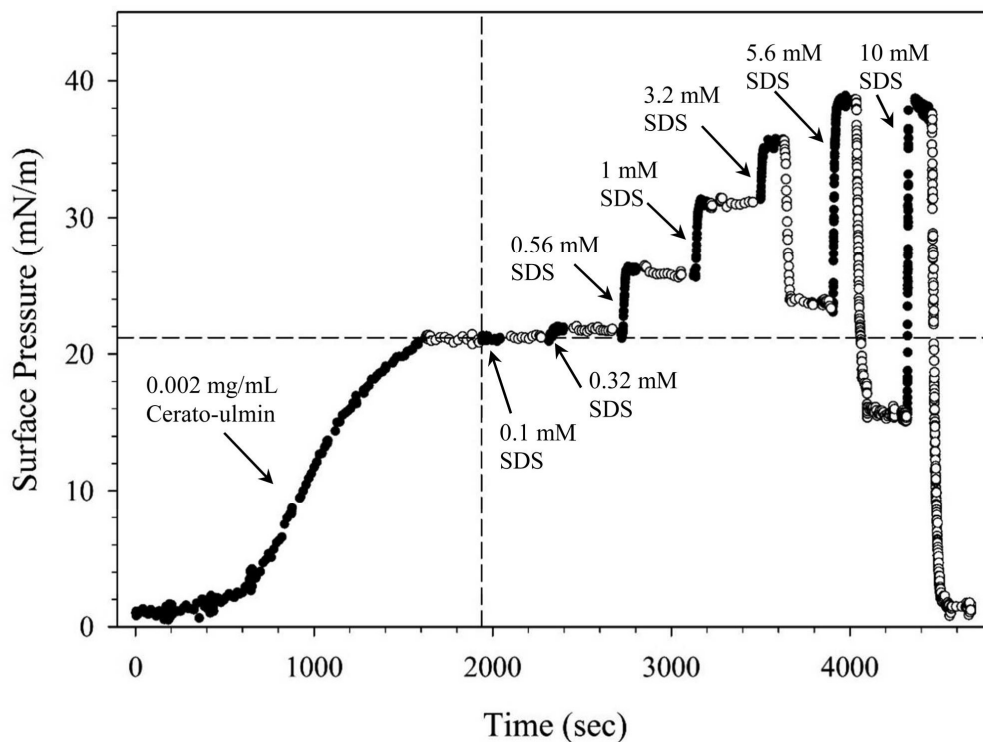
Figure 4.8. Dynamic surface pressure versus time for an air/water interface undergoing several bulk solution exchange steps. Filled symbols indicate adsorption from bulk solution, and open symbols indicate bulk fluid exchange with deionized water. Initially, the Cerato-ulmin adsorbs to the interface. The bulk fluid is exchanged with deionized water starting at 1650 seconds, once a protein film has formed. A 0.1mM SDS solution is introduced to the reservoir at 1950 seconds, indicated by the vertical dashed line. The surface pressure is allowed to reach steady state before the reservoir fluid is again exchanged with deionized water. This process is repeated with several increasing concentrations of SDS, up to 10mM (greater than the critical micelle concentration).[102]

Although our main focus is on the oil-water interface, it will prove valuable to update the previously published air-water results[102] by extending them to lower CU concentration and by considering the response of incompletely formed CU membranes to rinsing with water. In clean water, the microtensiometer provided a value of 72.8 ± 0.5 mN/m. Measurements at our previously used CU concentration of 2 μg/mL (0.26 μM) showed a surface tension reduction of ~15 mN/m (Figure 4.9). This result agrees with previous

115

measurements[15] by the du Noüy ring pull method at this concentration but falls short of our recent microtensiometry observations (~22 mN/m).[102]
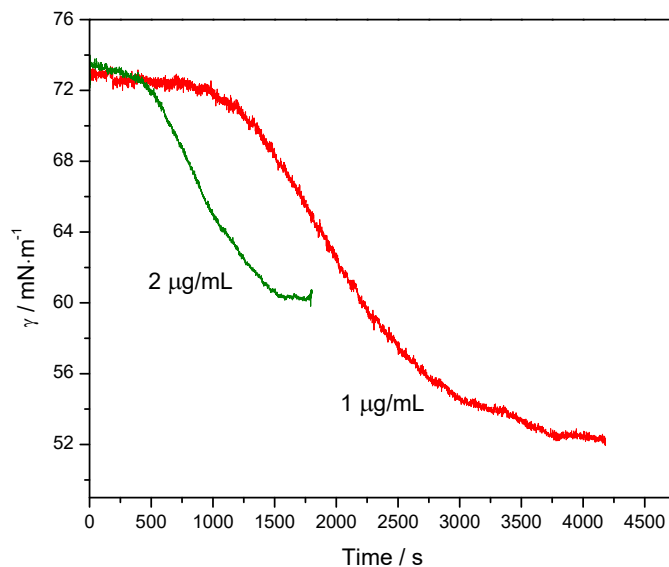
Figure 4.9. Dynamic surface tension of 1 μg/mL and 2 μg/mL of bulk CU dispersions at an air-water interface. Measurements were taken at room temperature using bubbles with similar interfacial curvatures (53 or 43 μm for 1 μg/mL and 2 μg/mL, respectively).

The easily measurable surface tension reduction suggested the feasibility of experiments at the even lower concentration of 1 μg/mL (0.13 μM). These experiments resulted, after longer initial plateaus and slower overall dynamics that necessitated longer measurements, in reproducible surface tension reductions of 22 mN/m. According to the du Noüy ring pull measurements,[15] which show the expected monotonic decline in surface tension with CU concentration, the maximum surface tension reduction is ~25 mN/m, seen at CU concentrations >30 μg/mL (3.9 μM).

These results suggest sensitivity to small differences in handling, a problem exacerbated by the propensity of CU and other hydrophobins to form and stabilize small bubbles in unusual shapes that do not minimize surface area for a given volume of trapped air.[46-47, 49] Measurements are also confounded by the fact that CU membranes form slowly into two-dimensional solids, making the comparison between a "static" experiment like du Noüy ring and an experiment that captures the full dynamics complicated. The observation that solutions at either 1 μg/mL or 2 μg/mL generate similar static surface pressures in a range of dilute solution demonstrates the exciting potential of these materials as surface active agents. Reproducibility at 1 μg/mL for the series of solutions studied here was very good and the important point lies in the *dynamics* of the surface tension reduction.

In all cases, the air-water surface tension versus time curves begin with a plateau where the surface tension does not vary significantly with time. At 2 μg/mL, whether in the present study or our previous one, this plateau lasts about 400 s. At 1 μg/mL the plateau time was extended almost three-fold to ~1200 s. As expected, these times are much longer than observed when measuring the interfacial behavior of small surfactants.[184] The exact duration of the initial plateau trended to longer values with repeat runs, likely due to depletion of material to the surfaces of the reservoir lowered the bulk concentration and slowed the dynamics. Working with dilute solutions of highly surface-active species does require concern over depletion of the bulk solution when measuring dynamics, but by using protocols of pre-rinsing/coating the reservoir with bulk solution we are confident in stating that the essential behavior—an initial plateau in surface tension followed by a rapid decline after a certain induction period—is a combination of slow diffusion to the interface and a competitive adsorption/desorption behavior.[185,42, 161]

To determine whether membranes evolve structurally during the adsorption process, the air-water interfaces were rinsed with deionized water after adsorption had progressed for a certain time. Figure 4.10 shows two individual dynamic surface tension measurements in which rinsing was performed early in the adsorption process (a low surface pressure) and later (a larger surface pressure), after steady state had almost been reached. For the early rinse run, the dynamic interfacial tension curve (red) decreased from the clean water value of 72.8 ± 0.5 mN/m. At 1600 s, when the dynamic surface tension reached 69.8 ± 0.5 mN/m, deionized water was introduced to the cell. The surface tension increased, indicating that some CU was removed from the interface. In the second run, the adsorption were permitted to continue for about 4200 s before exchanging the bulk solution. At this later time and larger surface pressure, the removal of CU from the surface was not observed. This suggests that the CU remained. The adsorption of CU is reversible at first, but becomes more difficult as the surface tension approaches its steady-state value. This observation invites measurements to determine the mechanical strength of the membrane.
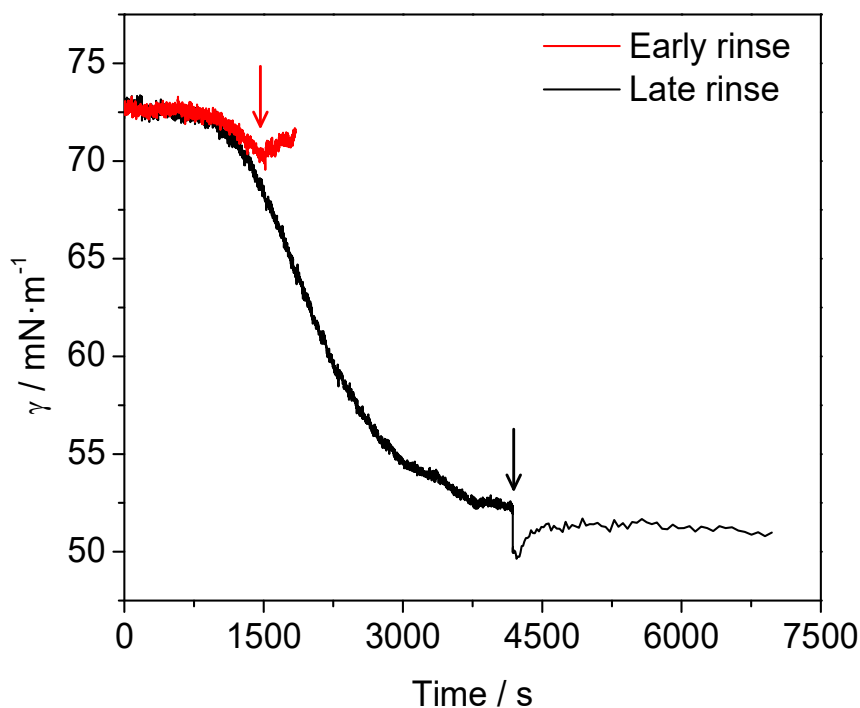
Figure 4.10 Effect of rinsing the interface with DI water on the adsorption of 1 µg/mL of CU at the air-water interface. Arrow indicates when a water rinse was begun at 1600 or 4200 seconds in each of the two separate runs.

4.3.2   Dilatational Modulus of the Air-water Interface

The dilatational modulus |E*| at the air-water interface was measured as described previously[102] by oscillation of the applied pressure (Figure 4.6). Figure 4.11 shows the magnitude of |E*| as a function of time for two different bulk solutions. At a CU concentration of 2 µg/mL, starting from about 18 mN/m before 400 seconds, the dilatational modulus increases and reaches a value of 764 ± 45 mN/m by 1460 s, which in these experiments is the microtensiometer's effective upper limit for reliable measurement (at longer times, the interfaces become too rigid and the radius modulations were too small

119

to detect [102]). This result should be compared to that of typical small molecule surfactants, about 10 mN/m.[190] For the lower concentration, 1 μg/mL, the dilatational modulus gradually increased, reaching about 15 mN/m at 760 seconds. Then it started to grow and followed the same trend as for 2 μg/mL of CU. The highest reliably measured value was 748 ± 39 mN/m. As with the interfacial tension behavior the development of modulus is faster for membranes formed from 2 μg/mL dispersions, but given extra time the membranes formed from 1 μg/mL dispersion are just as strong. So, although the data of Figure 4.9 show lower surface tension for 1 μg/mL compared to 2 μg/mL, we make no claim regarding the relation between interfacial tension and interfacial elasticity, or |E*|. Every interface measured achieved a modulus so large that the deformation of its shape upon application of oscillatory pressure was smaller than the optical detection limit of the instrument. This confirms the highly elastic interfaces reported previously, but now at either 1 μg/mL or 2 μg/mL. Not only can a competing surfactant as used in Ref. [102] but also pure water itself disrupt the CU membrane, as long as it is supplied early in the membrane formation (at about 1500 s in Figure 4.10).
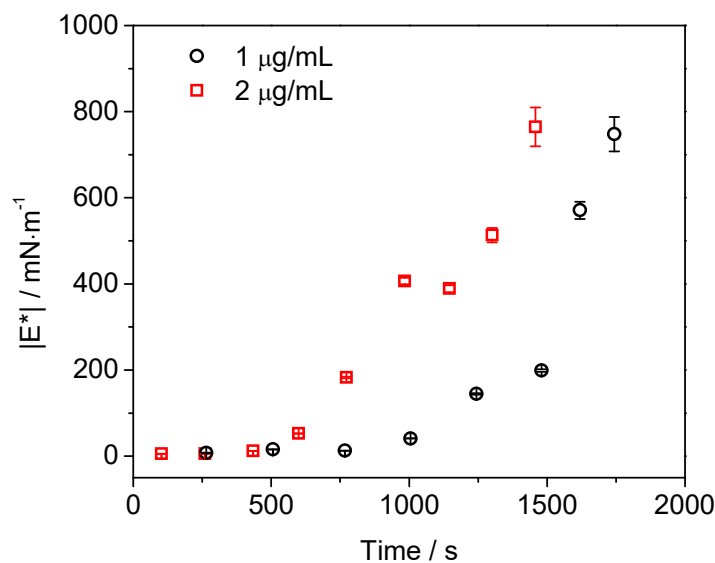
Figure 4.11 Dilatational modulus plot of 1 µg/mL and 2 µg/mL of CU at the air-water interface.

4.3.3 Oil-water Interface

A squalane-water interface was created that protruded slightly into the aqueous phase. Any air bubbles adhering to the tip were first removed by sweeping a sterile needle past the capillary. Figure 4.12 (black curve) shows the measured interfacial tension value as CU adsorbed from a dilute solution. The interfacial tension dropped immediately from the squalane-water value (52.5 ± 0.5 mN/m) and decreased continuously to a steady state value at 40 ± 0.5 mN/m, a reduction of 12.5 mN/m. Despite the lack of an apparent plateau at low times, as seen for air-water interfaces, almost 30 minutes were required for CU at the squalane-water interface to effect the full surface tension reduction. Again, many

121

factors may be responsible, including transport and orientation at interfaces, not to mention possible changes in the secondary structure. In a second run, the reservoir was pre-exposed to CU solution and emptied to guard against depletion of protein due to binding with the walls of the reservoir. As shown in Figure 4.12 (red curve) now the CU solution is able to reduce the surface tension from an intial value of 52.5 ± 0.5 mN/m by at least 23 mN/m.

In Figure 4.12 the reduction of interfacial tension is not steady but instead seems to accelerate after about 100 s. It almost levels out between about 300 s and 700 s before resuming its downward trend. Regarding the cause of this unsteady, or stepped, surface tension reduction, curvature of the interface itself does not introduce artifacts in microtensiometry measurements presented here. The technique relies on changes in the curvature and pressure jump across the interface to characterize the interfaces.[184] In our earlier work, the data for CU adsorbed at air-water interfaces were shown to collapse over a wide range of radii of curvature (see Figure 2 in Ref. [102]). Finally, there was no evidence that CU partitions from the aqueous into the oil phase; squalane left in contact with an aqueous CU dispersion returned the same interfacial tension against water as pure squalane. The most likely explanation for the stepped surface tension reduction is creation of non-equilibrium structures on the way to a more solid-like surface.
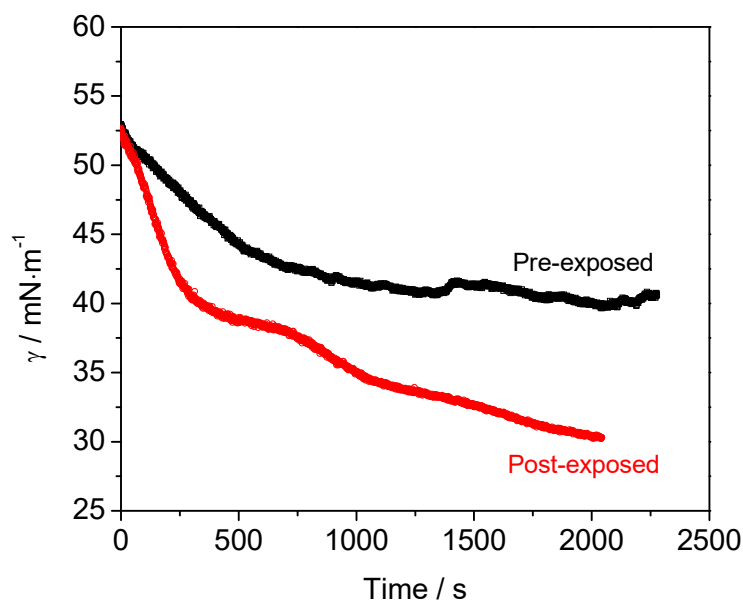
Figure 4.12 Dynamic interfacial tension of 2 μg/mL of CU at the squalane-water interface. The microtensiometer reservoir is either pre-exposed or post-exposed to dilute CU solution. Measurements were taken at room temperature using the interfacial curvatures (46 μm and 73 μm, respectively).

Comparison of adsorption from bulk solution to squalane-water and air-water interfaces reveals details of the adsorption behavior. Figure 4.13 shows the comparison in terms of surface pressure, defined as $\Pi(t) = \gamma_o - \gamma(t)$ where γ_o is the interfacial tension of the clean air-water/oil-water interface and $\gamma(t)$ is the instananeous measured interfacial tension of CU solution, as shown in Figure 4.9 and Figure 4.12. Representing the data as $\Pi(t)$ allows us to compare water and oil interfaces in terms of the differences, without regard for the pure air or pure oil surface tension values. The surface pressure rises as CU adsorbs to both interfaces, but for the squalane-water interface it starts increasing as soon

as the interface forms. At the air-water interface, an apparent plateau exists before the rapid increase in surface pressure. In this case, the final value of surface pressure reached is similar for both interfaces, suggesting a similar level of interfacial concentration (strict equivalence is not established, as that would require measurement of an isotherm). It seems adsorption of CU to an oil-water interface in a form capable of reducing surface tension is fast compared to that at an air-water interface, possibly due to differences in transport, molecular rearrangements or orientation of CU.[185, 195] In the next two sections, exploration of these possibilities from mechanical and spectroscopic perspectives are shown.
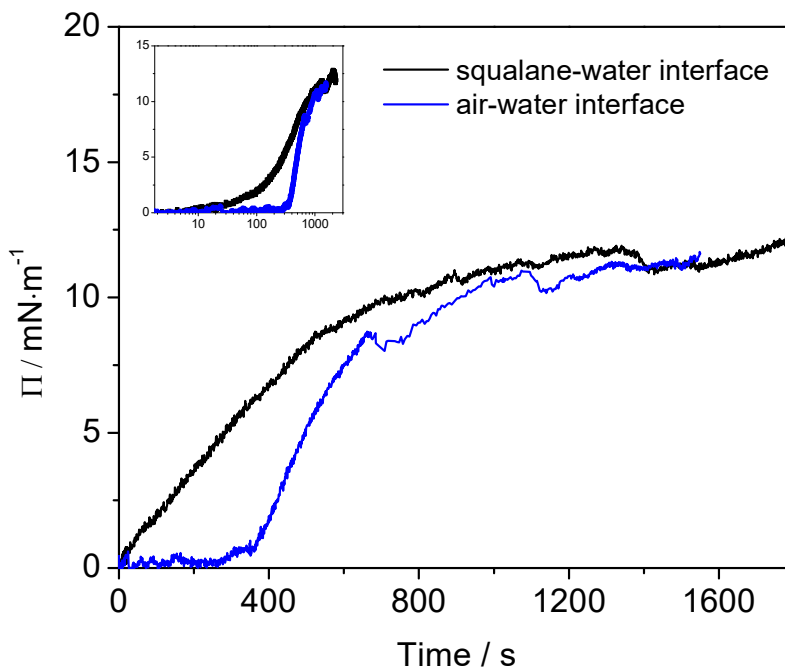
Figure 4.13 Comparison of surface pressure as a function of time at squalane-water and air-water interface (Inset is semi logarithmic representation). Bulk solution concentration is 2 μg/mL. Capillary radii were 46 μm and 43 μm, respectively. Larger surface pressures are sometimes observed at the air-water interface.[102]

4.3.4   Dilatational Modulus of the Oil-water Interface

As in Figure 4.10 for an air-water boundary, dilatational measurements were performed during the relaxation of an oil-water interface. Figure 4.14A shows interfacial tension and curvature profiles at the squalane-water interface with periods of applied oscillations. The interfacial tension decreases as CU adsorption takes place and surface pressure increases to 20 mN/m. Figure 4.14B shows the dilatational modulus as a function of time as CU adsorbs to the squalane-water interface. The dilatational modulus increases from 45 ± 2 mN/m to a highest reliably measured value of 339 ± 19 mN/m over a time of ~30 min. These values are higher than the moduli typically measured for small-molecule surfactants, but lower than measured for CU at the air-water interface. Experiments were conducted by simply filling the reservoir, as with the air-water interface measurements, and after pre-treating the reservoir by exposing it to CU solution and emptying prior to loading with fresh solution. Given the result of Figure 4.12, it is not surprising that the latter procedure produced the stronger dilatational moduli. Results in this section refer to the measurements after pre-treatment of the reservoir, but the outcome is the same with or without pre-treatment: very low concentrations of CU produce very large surface tension reductions and high dilatational moduli.
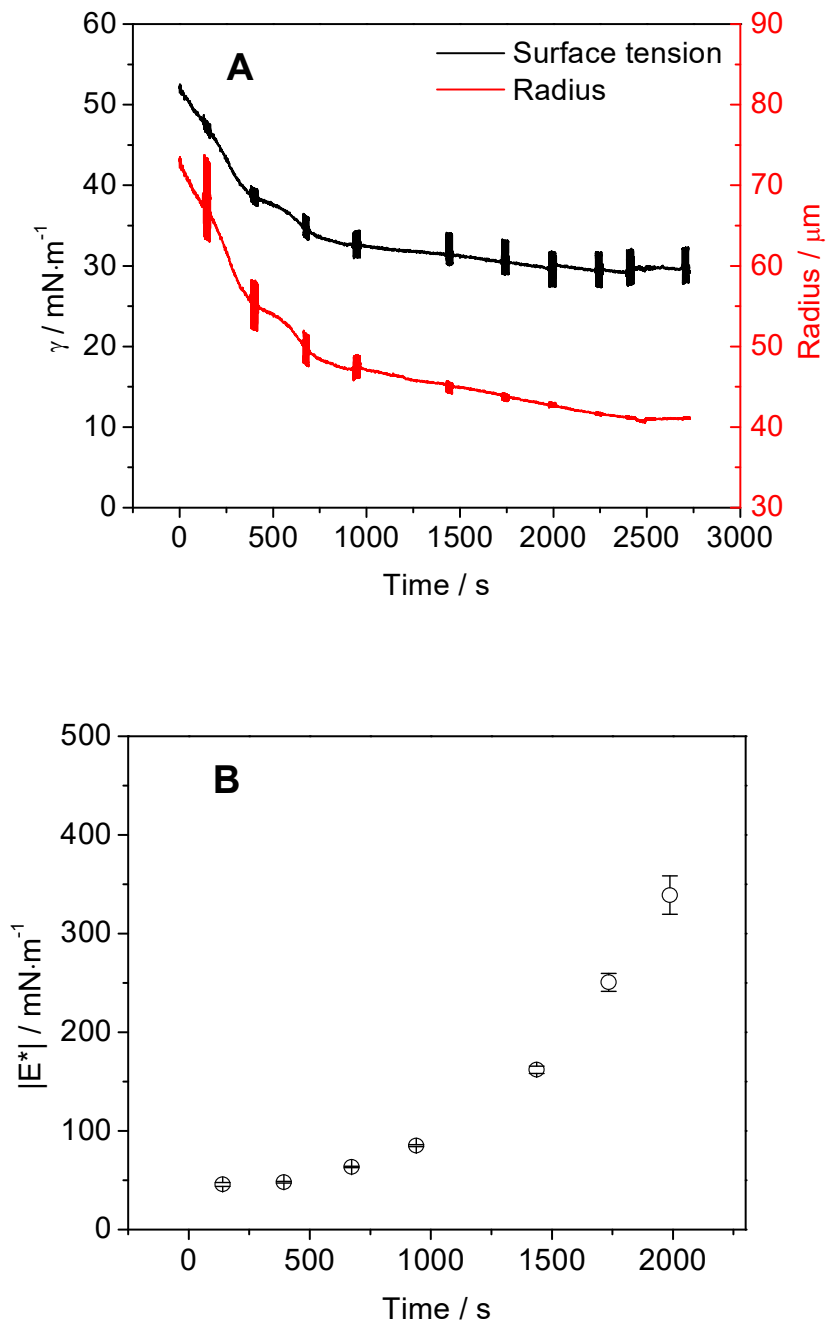
Figure 4.14 Dynamic interfacial tension and radius measurements while oscillating the squalane-water interface (A) and dilatational modulus (B) as a function of time. The system is 2 μg/mL of CU at the squalane-water interface.

4.3.5   Circular Dichroism

Circular dichroism spectroscopy was performed to identify structural characteristics of CU and how they may change at interfaces. First, CD spectra were recorded at different CU concentrations; see Figure 4.15. The CD signals were too weak to collect at the concentrations below 20 μg/mL, so the same low concentrations used for microtensiometry could not be investigated. At all measurable concentrations, the overall features of the far UV CD spectra were similar. All spectra are characterized by a minimum at ~200 nm, suggesting CU is rich in β-sheets. A weak negative band close to 225 nm indicates partial α-helical structure. These results agree with those of Yaguchi et al., who reported infrared and Raman spectra showing that CU contains both β-sheet and α-helix.[91] Although no major changes appear, the band intensity at 200 nm increases with CU concentration, which is attributed to increased β-sheet folding. It is known that hydrophobins self-assemble into aggregates (dimers or tetramers) driven by the interaction between the surface hydrophobic patches existing among monomeric molecules. The secondary structures such as β-sheets and α-helical structure are expected to be preserved during self-assembly.[196] This could explain the minor change in the far UV CD with increasing CU concentration. Agitation of CU solution leads turbidity due to the formation of microstructures stabilized by CU,[46] yet no changes in CD spectral shape were observed after vigorous shaking of the solutions. Only a slight alteration of intensity was seen, which was due to accumulation of protein at the air-water interface.[45] The effect of a hydrophobic solvent, ethanol, on the secondary structure of CU was also studied. The far UV CD spectrum of CU in 70% ethanol (v/v) indicate that ethanol does not have a dramatic effect on the conformation of the hydrophobin within the bulk solution. Similar observations have been reported for Class I

hydrophobin EAS$_{\Delta 15}$.[197] Temperature also had almost no effect on the shape of the CD spectra of CU solutions (Figure 4.16) but reductions in the band intensity with increasing temperature probably signal partial unfolding.
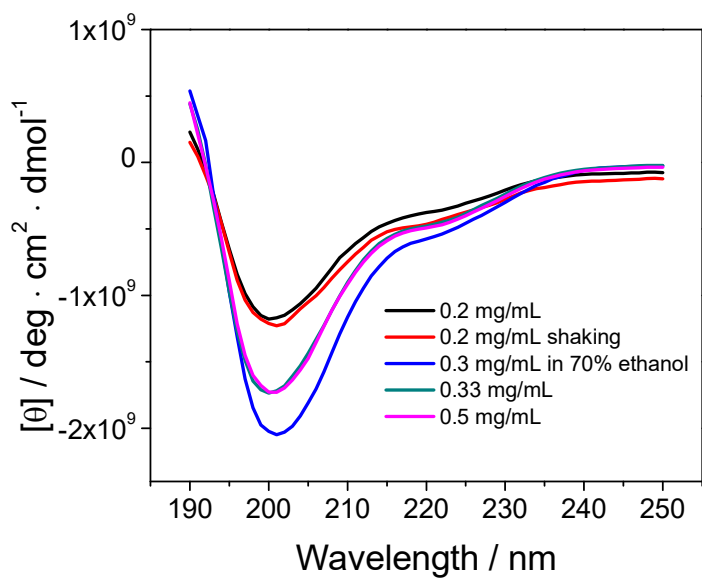
Figure 4.15 CD spectra of the *Cerato-ulmin* hydrophobin in water at different concentration, after vigorous shaking and in 70% ethanol (v/v).
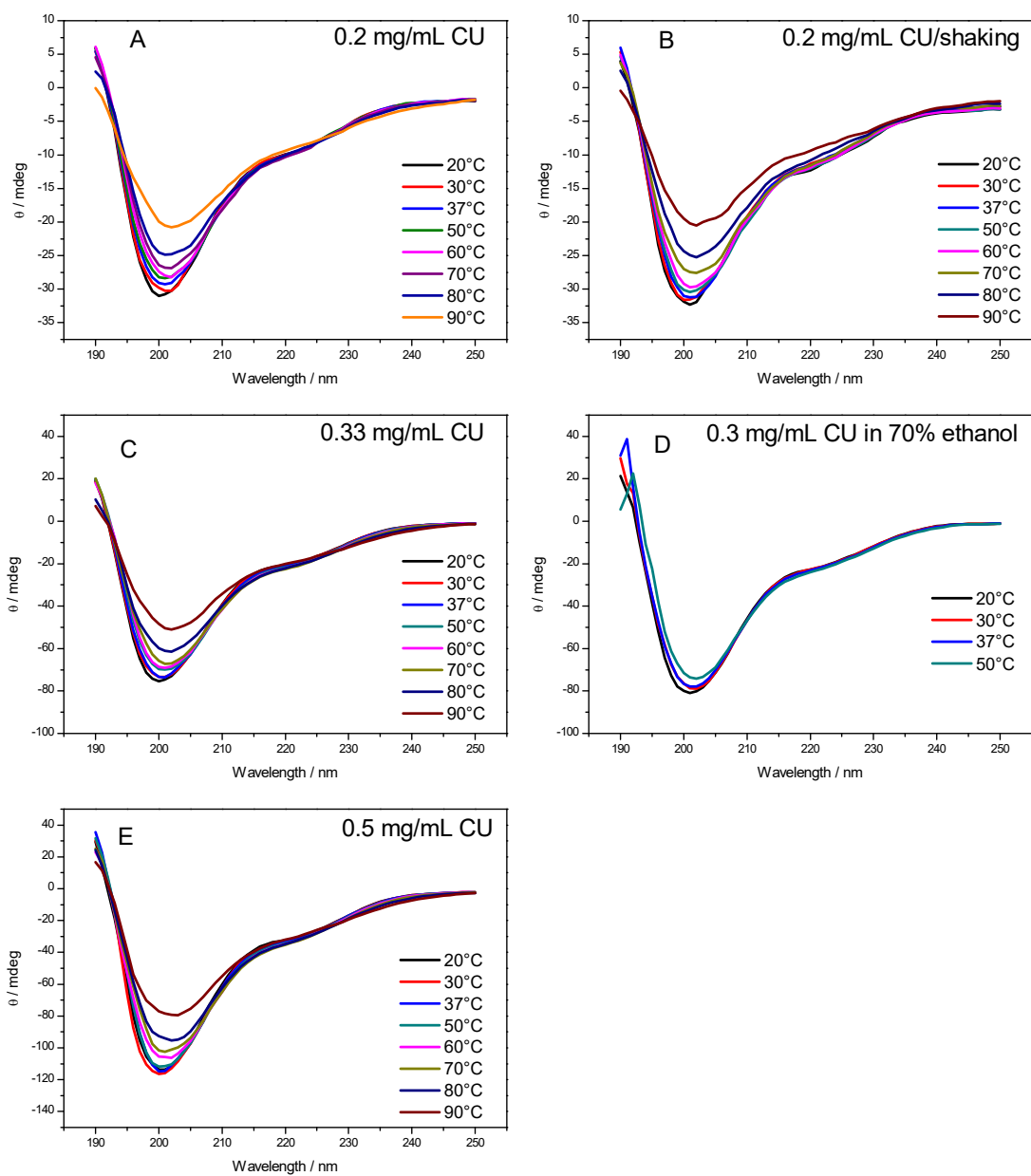
Figure 4.16. CD spectra of the *Cerato-ulmin* hydrophobin as a function of temperature. (A & B) 0.2 mg/mL CU before and after shaking, (C) 0.33 mg/mL, (D) 0.33 mg/mL in 70 % ethanol (v/v) and (E) 0.5 mg/mL.

Having established the basic CD spectroscopy of aqueous and ethanolic CU solutions and agitated suspensions, we can turn to the behavior in the presence of oil. These studies were accomplished by shaking CU suspensions in the presence of squalane. This had almost no effect on the CD spectrum, as shown in Figure 4.17, but ultrasonication resulted in an emulsion, whereupon the minimum band of the CD spectrum lost intensity, broadened, and shifted from 200 nm to 205 – 208 nm. The signal at 225 nm intensified. These changes indicate an increase in α-helical content. Such changes resemble the conformational transition of the Class II hydrophobin HFBI when it binds to colloidal Teflon.[45]
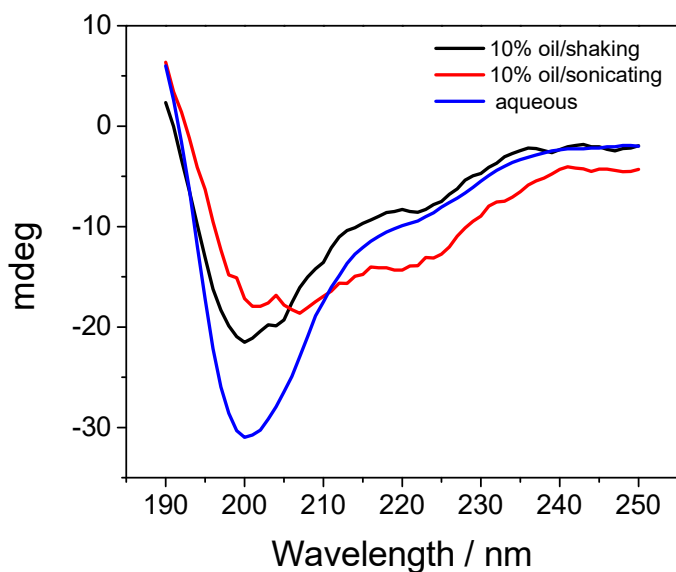
Figure 4.17 CD spectra of 0.2 mg/mL of *Cerato-ulmin* hydrophobin in the presence of oil, with shaking, and after sonication.

To summarize the results, high surface pressure (~20 mN/m) was observed from very dilute CU solutions (1 µg/mL or 0.13 µM) at both air-water and oil-water interfaces. The corresponding elastic modulus reaches values almost 75 times higher than observed for typical surface-active proteins. The mechanism leading to such strong interfaces for CU is not known, but the process is likely controlled by the rate of diffusive transfer relative to that for adsorption to the interface in an orientation and form that can reduce surface tension.[163, 166] Once bound, or perhaps concurrent with binding, the protein may experience conformational change,[42] jamming[109, 190] and/or "sticky" hydrophobic interactions with neighboring proteins.[198] At the air-water interface, surface tension reduction and elastic strengthening only occur after an induction period, which is much longer than it is at oil-water interfaces.

These results are consistent with others on interfacial protein adsorption. In a study on the Class I hydrophobin H*Protein B, Richter et al.[181] classify adsorption into three regimes, following the work of Beverung, Radke and Blanch[166] on non-hydrophobin proteins. In Regime I, corresponding to the induction period, proteins diffuse to the interface without much effect on surface tension. Regime II is characterized by a rapid decline of surface tension. In the third and final regime, the reduction in surface tension slows as the interface solidifies (Beverung, Radke and Blanch use the term "gelation" for this phase). The CD spectra of Figure 4.17 support the notion of a surface-induced conformational transition for the oil-water interface, but no such evidence is found from Figure 4.15 for the air-water interface. It has been reported that Class I hydrophobin SC3 undergoes structural changes at adsorbed interfaces,[30] but the two Class II hydrophobins HFBI and HFBII did not show significant conformational changes at the molecular level

at an air-water interface.[45] They do in the presence of colloidal PTFE, and this resembles our result at a squalane-water interface after sonication. Other mechanisms to stabilize the surface may occur concurrently (at least at the time resolution of our present experiments) with the conformational transition sensed by CD. For example, hydrogen bonding, hydrophobic and covalent bonding (crosslinking), and electrostatic interactions may vary strongly.[161] The fashion of the hydrophobin molecular packing could also affect surface elasticity. Knoche *et. al* [199] proposed a model featuring hard cores with soft shells to explain the elastic properties of hydrophobin-coated interfaces. Elucidation of the degree of surface coverage or the importance of conformational change requires a separate measurement like neutron reflectivity[128, 200] or vibrational sum-frequency generation spectroscopy.[201-202]

4.4   Conclusion

Cerato-ulmin reduces the interfacial tension of both oil-water and air-water interfaces, even at a low CU concentration of 1 µg/mL (0.13 µM). The quick action at oil-water interfaces compared to the long induction period at air-water interfaces suggests that CU adsorbs in a form capable of reducing tension more quickly at oil-water interfaces relative to air-water interfaces. In support of this idea, far UV CD spectra show a significant enhancement of the helix content after oil-water microemulsion formation. Other potent environmental factors such as alcohol and temperature only exert a comparatively minor effect on CU's secondary structure. For either oil-water or air-water interfaces, many minutes are required to reach steady interfacial tension values, suggesting that it is worthwhile to characterize protein transport fully before designing applications. Initially, CU adsorption at an air-water interface is reversible by water rinsing, but this property is

lost in aged samples. The increase in dilatational interfacial modulus during oscillation experiments shows that the air-water interface stiffens as CU adsorbs. The highest reliably measured dilatational modulus at the air-water interface was 764 ± 45 mN/m but aged membranes probably achieve even greater moduli not measurable by our methods. The CU-adsorbed squalane-water interface is not as rigid as the air-water interface but still shows very high stiffness, ultimately reaching a dilatational modulus of 339 ± 19 mN/m. These values are higher than those measured for most proteins, including other hydrophobins (Table 4.3).[34, 49, 102, 121, 129, 180-181, 203-204]

Table 4.3. Interfacial moduli measured for various hydrophobin systems.

Hydrophobin	Class	Dilatational/Shear Elasticity (mN/m)	
		Air-water interface	Oil-water interface
Cerato-ulmin	II	>764 (0.0002 wt%)[102,205]	>339 (0.0002 wt%)/squalane[205]
HFB II	II	300 -350 (0.002 wt%)[121] 500 (0.15 wt)%[129]	150 (0.005 wt%)/soybean oil[180,a] 110 (0.005 wt%)/n-hexadecane[180,a]
HFBI	II	500 (0.00072 wt%)[49,a]	500 (10 wt%)/Galden® V90[203,a]

Charged-engineered HFBI	II	1400 (0.00023 wt%)[204,a]	/
H* Protein A	I	/	4 (0.4 wt%)/octane[34]
H* Protein B	I	/	25 (0.000047 wt%)/silicon oil[181]
[a], shear elasticity			

Much remains to learn about CU adsorption to air-water and oil-water interfaces. For example, how quick is the transition in the secondary structure relative to adsorption and surface tension reduction/modulus build-up?
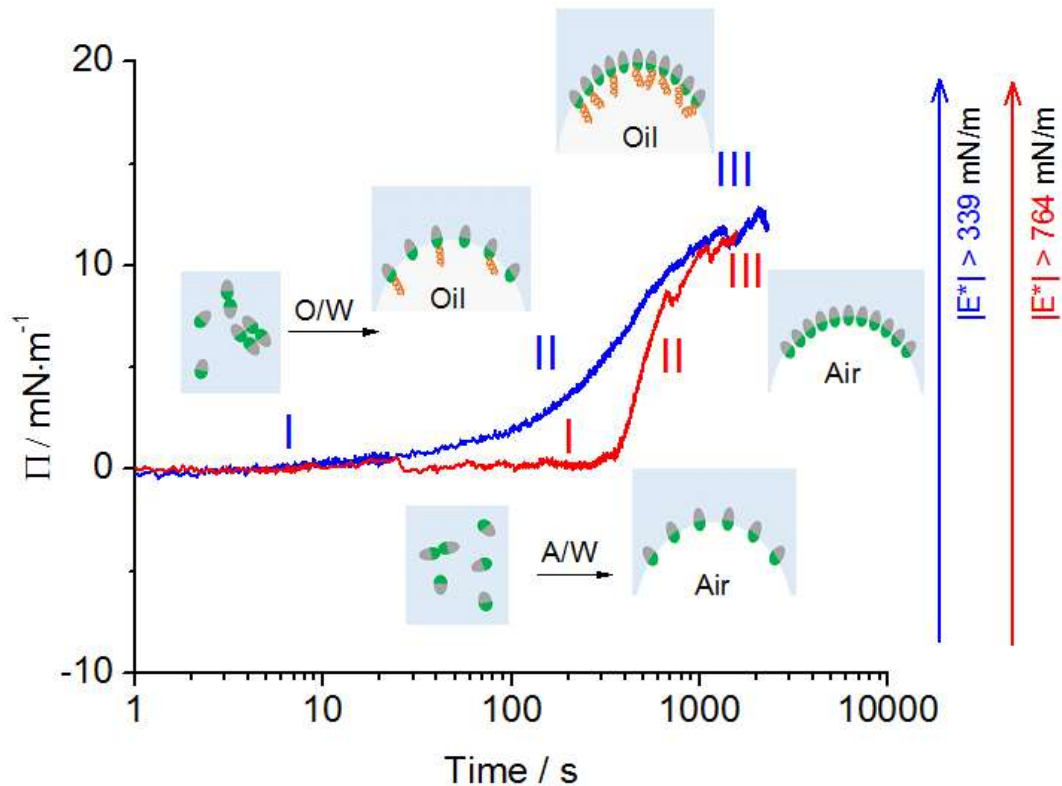
Figure 4.18 Membrane development at oil-water (blue curve) and air-water (red curve) interfaces, showing induction period for air-water curves, followed by more rapid growth in surface pressure.

Figure 4.18 depicts a tentative scheme, based on that of Beverung, Radke and Blanch;[166] see also Richter et. al..[181] It highlights the differences between air-water and oil-water interfaces, including the secondary structural conformation transition in the latter case (indicated by orange helix). The air-water surface stronger than the oil-water interface, and strengthens quickly after a long induction period. The increased helix content attending the adsorption of CU to an oil-water interface is largely based on ultrasonication results leading to a microemulsion. The fast action at oil-water interfaces (compared to air-water case) could equally well be the result of specific interactions with the oil phase.

Promising avenues for future investigation include other frequencies for the dynamic measurements and the addition of salt and other components, like alcohols and oils other than squalane, that may alter possible conformational transitions, or "sticky" interactions. Physicochemical characterization of CU and its aggregates as a function of concentration in the bulk phase may help to identify why there is a plateau prior to surface tension reduction at the air-water interface and why it varies with concentration. Given the low concentrations, these experiments are expected to be challenging. Similar investigations in a bulk CU dispersion under an oil-water interface could reveal whether trace oil in the aqueous phase alters how CU is dispersed. Finally, the strength of the membranes invites continued experiments to use hydrophobins to develop novel materials.

CHAPTER 5.   DIFFUSIVE DYNAMICS OF CU BUBBLES

DEBRIS AND NANOPARTICLES UNDER CU OIL DROPLET

CONFINEMENTS BY DIFFERENTIAL DYNAMIC

MICROSCOPY

5.1   Introduction

The diffusion of small molecules, macromolecules, and nanoparticles is evident in chemical, biological and physical systems. Nevertheless, these systems often include complex and confined geometries and fluids. For example, natural porous structures and surfaces, crowded environments and complex biological systems. Understanding the dynamics of nanoparticles in a variety of complex systems is of significant interest[206] and is required for not only fundamental studies[207] but also different applications, such as drug delivery, enhanced oil recovery and remediation.[208] Brownian motion caused by thermal motions characterizes of particle diffusion in the liquid phase. Robert Brown was the first to describe the motion of pollen particles in a static liquid suspension.[209] Einstein solved the relationship between the coefficient of diffusion of the particle (D) and other physical properties including the particle radius (R), and the viscosity (η) of the liquid phase at a temperature (T).[210]

Two common techniques have been used to quantify the dynamics of a suspension of nanoparticles either as individuals or as a group. The particle tracking method tracks the position of an individual particle based on real-space micrographs as a function of time. The determined trajectory provides information on the dynamics in a limited region of interest of a sample. The experimental setup includes an optical microscope and open source algorithm. Particle tracking becomes more challenging for nanoparticles as their size is smaller than the resolution of the microscope. The other well-known technique for characterizing the dynamics of nanoparticles is the scattering method. Depending on the incident light, it consists of light, X-rays and neutron scattering. Traditionally, the diffusive dynamics of nanoparticles in dilute suspension have been measured by dynamic light scattering (DLS). DLS consists of shining a laser through the dilute particle suspension and monitoring the intensity fluctuations of scattered light as a function of time. It provides the average information on the dynamics of a sample. DLS also has limitations. For example, DLS is typically not reliable for measuring dynamics in complex geometries or region of interest of a sample. It also struggles in very dilute suspensions, and is not suitable for high concentrations of a sample.

Differential dynamic microscopy, also known as DDM, is becoming an emerging technique to measure sample dynamics. It was first developed by Cerbino and Trappe in 2008.[211] This new approach consists of a standard light microscope with normal illumination and a digital fast camera. A series of sample images is analyzed using a digital Fast Fourier transform and the relevant dynamics are obtained.[212] The first attempt was made to measure an aqueous dispersion of colloidal particles with 73 nm using simple bright-field illumination.[211] Since then, different microscopy approaches have been

developed, ranging from bright-field to fluorescence-based, confocal, polarized, and dark-field to study diverse systems. Ferri et al. studied the kinetics of colloidal fractal aggregation induced by adding salt.[213] Wilson and Martinez used DDM to measure the dynamics of E. coli bacteria and their swimming speed distribution.[214-215] He et al. reported the diffusive dynamics of polystyrene nanoparticles using fluorescence based DDM and compared to the measurements from dynamic light scattering.[216] Confocal DDM was first introduced by Lu and they characterized concentrated hard-sphere-like colloids.[217] The dynamics of nematic liquid crystals[218] and gold nanoparticles have been studied using polarized and dark-filed based DDM, respectively. Others include anisotropic magnetic particles[219] and Janus particles.[220]

Researchers have also applied DDM to more complex systems and confined geometries. Dienerowitz and co-workers were able to retrieve the flow information from the image structure function of sub-diffraction nanoparticle suspension.[221] DDM allowed them to spatially resolve the flow velocity and map out the flow profile across the width of a microfluidic channel. Cell mobility on curved substrates was observed by Gouglass.[222] They found the minimal radius of curvature that constrains motility of rat Schwann cells along the axis of cylinder is determined based on difference images analysis. Another example is the determination of the diffusive dynamics of nanoparticles in microfabricated arrays of nanoposts. The Conrad group showed the dynamics of nanoparticles of diameter 200 - 400 nm slowed as the spacing between posts was decreased.[223-224] They further conclude the strongly confined nanoparticles experience a heterogeneous spatial environment leading to non-Gaussian diffusive dynamics.[225] Other examples include

anomalous diffusion behavior of small particles as they move in a slowly rearranging, glass matrix of large spheres.[226]

One objective of this research is to use DDM to measure dynamics of hydrophobic polystyrene latex beads in oil droplet confinement stabilized by CU membrane. First, DDM was validated by measuring dynamics of standard monodispersed polystyrene beads aqueous solutions. As a second application, DDM is demonstrated to study diffusive dynamics for region of interest. Specifically, bubble debris expelled from micrometer CU-coated bubbles were of interest. Finally, DDM is proved to be an easy and powerful technique for local diffusive dynamics of particles confined in CU-coated oil droplet. This suggests potential for applications such as controlled drug release from encapsulations/vesicles.[208]

5.2 Materials and Methods

5.2.1 Latex Beads Suspensions

Uniform polystyrene (PS) microspheres and cross-linked poly(styrene/divinylbenzene) (PS/DVB) were purchased from Bangs Laboratories Inc., Polysciences Inc. and ThermoFisher Scientific. The diameter of microspheres includes 50 nm, 119 nm, 290 nm, 500 nm and 1 - 2 μm. The nanoparticles are well dispersed in water with the addition of a trace amount of surfactant to inhibit aggregation and promote stability at a weight fraction of 1 – 10%, depending on vendor. Generally, the nanoparticles have a density of 1.05 g/cm^3 and a refractive index of 1.59 at a wavelength of 589 nm (25 °C).

DDM microsphere aqueous suspensions were prepared by diluting the original concentration in 1:1 or 1:2 v/v with deionized water or used as received without dilution. Non-aqueous suspensions of cross-linked PS/DVB particles were prepared following the protocol in elsewhere.[227] To transfer the particles from aqueous to organic solvent, they were first treated with deionized water and then transferred to the organic solvents. Because many organic solvents are not miscible with water, successive steps of solvent exchange were performed. In brief, first exchange was made to water in the original suspension with ethanol through 3 cycles of dilution and concentration; in each cycle, the particle suspension was diluted with ethanol, sonicate for 10 minutes, centrifuge at 4700 RPM for 30 minutes, and remove the supernatant. Then the process of dilution and concentration with octanol to exchange ethanol for octanol was repeated for 3 times. To suspend the particles in nonpolar solvents such as toluene, suspension of particles was diluted by volume in octanol by a ratio of 1:10 with the desired nonpolar solvent. Nanoparticle dispersions were withdrawn by capillary force to VitroCom rectangular capillary tubes. The typical dimensions for the capillaries were 100 μm in thickness and 1 mm in width. The samples were flame-sealed to prevent evaporation.

5.2.2 Theoretical Background of Differential Dynamic Microscopy

The DDM experimental set up consists of a Leica DM2500P microscope equipped with a scientific CMOS camera (PCO.edge, 1920 × 1280 pixels). A condenser lens (numerical aperture 0.9) is used to focus white light on the sample. An objective with 50 ×

magnification (numerical aperture 0.55) is used for detection. In a typical experiment, a stack of 3000 images is acquired with a frame rate of 60 fps and an exposure time of 8 ms. The longer exposure time potentially provides higher signal-to-background contrast, which is crucial to extract the light scattering off the samples from overall signal background in the data analysis process later. The region of interest is set to 500×500 pixels in the middle of the camera sensor. The size and location of the region of interest are subject to change depending on the needs.

To extract the dynamics of the particles, a DDM algorithm was written in MATLAB by Dr. Jinxin Fu as described in the literature.[211] First, the intensity difference,

$$D(x, y; \Delta t) = I(x, y; t + \Delta t) - I(x, y; t) \tag{5.1}$$

is obtained by subtracting two images acquired at different times, where $I(x, y; t + \Delta t)$ is the intensity obtained in the sensor plane (x, y) at time t, and the minimum delay time Δt here is 0.017 s depending on the frame rate. After performing Fourier transform of $D(x, y; \Delta t)$, we obtained,

$$F_D(u_x, u_y; \Delta t) = \int D(x, y; \Delta t) exp[-i2\pi(u_x x + u_y y)] dxdy \tag{5.2}$$

where (u_x, u_y) are the coordinates in Fourier space. By calculating the square of the absolute value of $F_D(u_x, u_y; \Delta t)$ and assuming the sample is isotropic, the 2D image structure function $|F_D(q, \Delta t)|^2$ is obtained. Finally, we fitted it to,

$$|F_D(q, \Delta t)|^2 = A(q)[1 - f(q, \Delta t)] + B(q) \tag{5.3}$$

$$f(q, \Delta t) = exp(-\Delta t / \tau(q)) \tag{5.4}$$

where $q = 2\pi\sqrt{u_{\tilde{x}}^2 + u_{\tilde{y}}^2}$ is the scattering wave factor by averaging azimuthally, $A(q)$ is the signal factor, $B(q)$ is the background, and $\tau(q)$ is the relevant q-dependent decay time. A single exponential fitting model is used to extract the decay time using OriginLab software. The decay rate ($\Gamma(q)$) is defined as $1/\tau(q)$, and the diffusivity of nanoparticles $D_m = \Gamma(q)/q^2$, is obtained by linear fitting going through origin intercept. More theoretical background appears in the original DDM paper[211] and in review articles.[212, 228]

5.3   Results and Discussion

5.3.1   Dynamics of Latex Nanoparticles in Aqueous Suspensions

A sequence of N = 3000 micrographs was acquired with a sampling rate of 125 frames/s and an exposure time of 4 ms. Figure 5.1A shows a typical bright-field microscope image of 119 nm latex particle in an aqueous suspension. The image appears as a bright background with some dark spots. These dark spots are dust particles located on the camera

sensor. The particles of interest are below the resolution of the microscope, which is $\lambda/2NA \approx 0.58$ µm. The signal due to the particles is barely visible as it contribution is small compared to the large background signal. Although they are weak, the signal caused by Brownian motion of the particles is dynamic and fluctuates all the time while the background signal is static. Subtracting two images acquired at different times allow to eliminate the background contributions in images and promote the particles signal. Examples of difference images obtained by this subtraction procedure are shown in Figure 5.1B, C and D. They are separated in time by 8 ms, 80 ms and 240 ms, respectively. The signal has become visible after subtractions and has increased as the grainy appearance of the difference images increases due to long separation time. The increasing signal suggests the increasing displacement of the particles. Figure 5.2 image structure function $|F_D(q, \Delta t)|^2$ for the images B, C and D in Figure 5.1. Each image is the result of an average over 1000 statistically independent difference image with the same separation time. The donut signal has increased too.
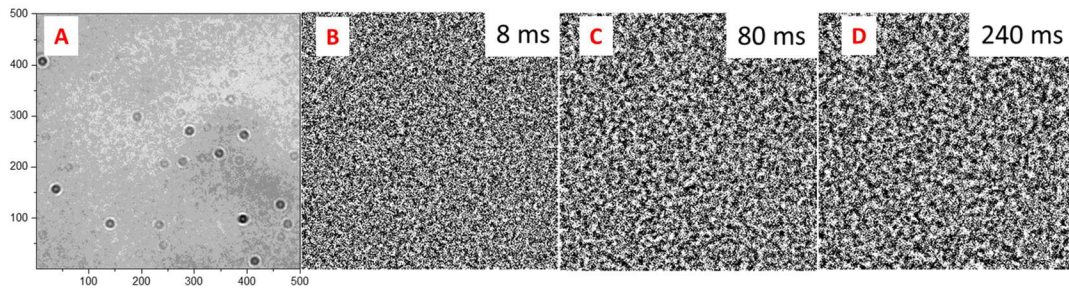
Figure 5.1. (A) Microscope image of an aqueous suspension of 119 nm particles at a weight fraction of 1.3%. The particles are below the resolution of the microscope and the signal generated by them is very small. (B to D) Results of the subtraction of two images taken 8 ms, 80 ms and 240 ms apart in time. The signal due to the particles is now visible from diffuse speckle patterns and has increased. The size of each panel corresponds to 51 μm in the sample.
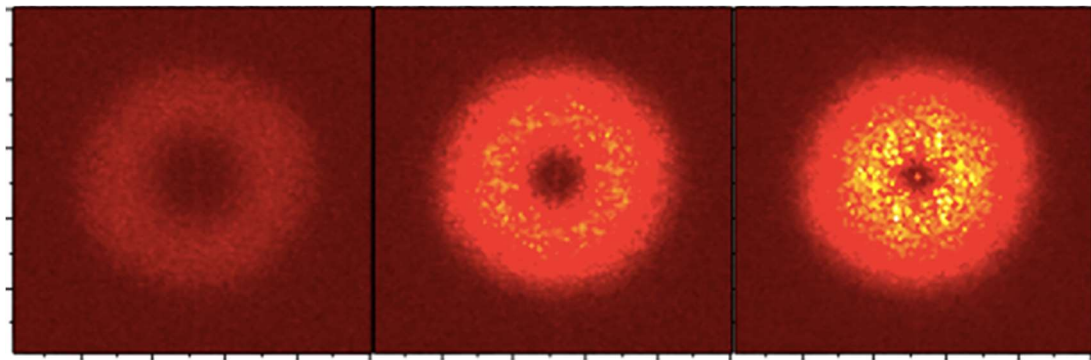
Figure 5.2. Results of images structure function $|F_D(q, \Delta t)|^2$ for the images B, C and D in Figure 5.1. Each image is the result of an average over 1000 statistically independent difference image with the same separation time. The donut signal has increased too.

From a time series of images similar to those shown in Figure 5.1A, the azimuthal average $|F_D(q, \Delta t)|^2$ was calculated as a function of the wave vector q for different values of the separation time Δt (see Figure 5.3). The area under the curve increases with Δt. Representative delay time dependence of the image structure function $|F_D(q, \Delta t)|^2$ at three values of q (= 1.60 μm^{-1}, = 2.83 μm^{-1}, = 3.45 μm^{-1}) for suspensions of nanoparticles with diameter 119 nm is shown in Figure 5.4. Data at different values of q increased monotonically with the delay time Δt until reaching a plateau at long delay times, indicating the system had decorrelated. The crossover to the plateau value shifts to smaller Δt as the wave vector q increases, suggesting a q dependence in the characteristic time of the system. Such behavior is similar to q -dependence correlation functions in DLS. The non-normalized representation of the image structure function against delay time (Figure 5.4) looks odd at first glance because the black curve corresponding to low q value has the highest slope. After normalization of the baselines for each q value, it is clear that the black curve is the slowest plot.
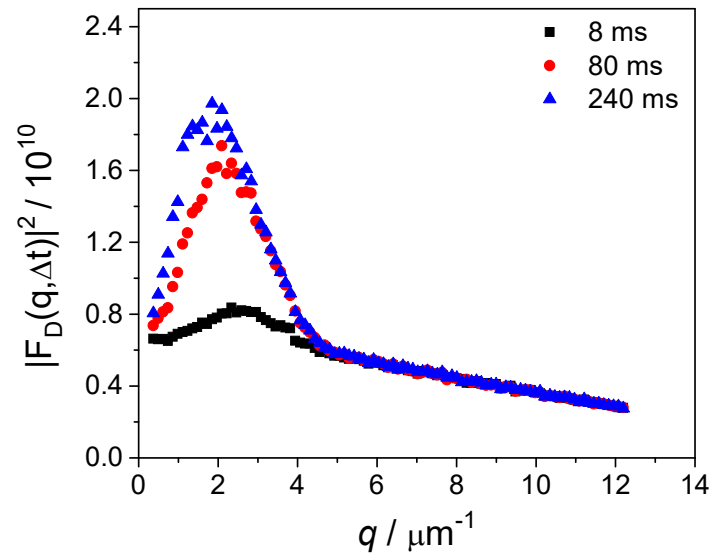
Figure 5.3. The image structure function is plotted as a function of *q* for different values of separation time.
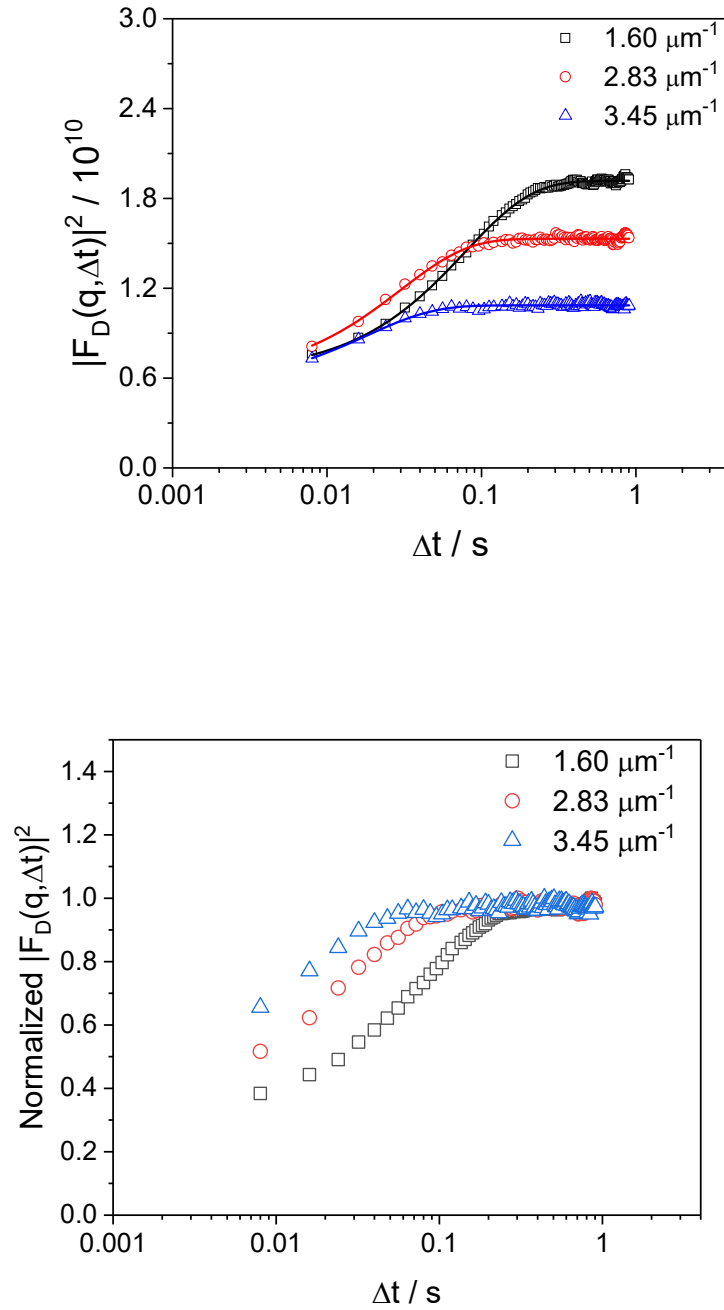
Figure 5.4. Growth of $|F_D(q, \Delta t)|^2$ with delay time Δt for three values of q. The continuous lines are fits of the data to Equation 5.4.

Fitting the data in Figure 5.4 to Equation 5.4 allows to extract the characteristic time $\tau(q)$, as shown in Figure 5.5 for q ranging from 0.5 μm^{-1} to 5 μm^{-1}. $\tau(q)$ scales as q in power of 1.95 ± 0.03, which is close to the theoretical value of 2 for Fickian diffusion. Using the formula $D = \Gamma(q)/q^2$, the diffusion coefficient of the nanoparticles is fitted to be 4.4 ± 0.1 $\mu m^2 \cdot s^{-1}$. The estimated diffusion coefficient (using Stokes-Einstein equation) is 4.1 $\mu m^2 \cdot s^{-1}$. The experimental result is in good agreement with the theoretically expected values over the q range. The decay rate (Γ) versus q^2 is sensitive to linear behavior.
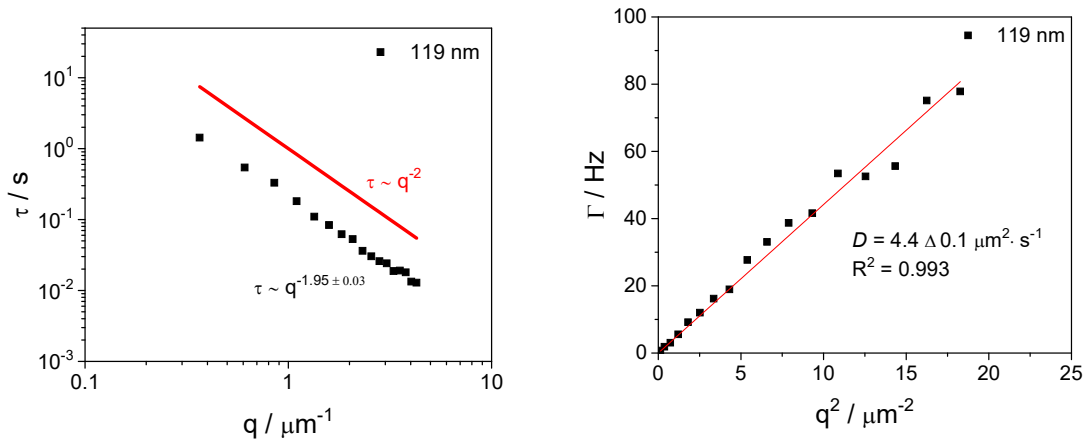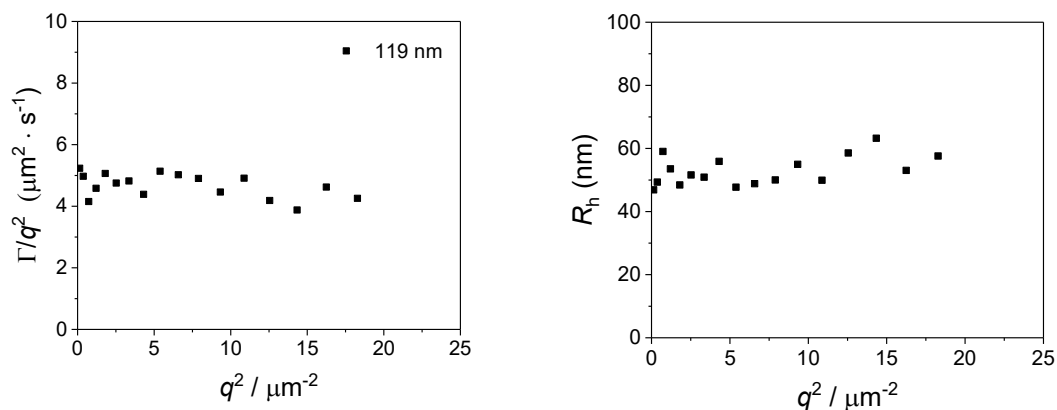
Figure 5.5.Plots of τ vs q, $\Gamma(q)$ vs q^2, $\Gamma(q)/q^2$ vs q^2, and R_h vs q^2 for the 119 nm (diameter) particles.

Measurements from particles with different diameters were also performed using DDM. The characteristic decay time τ versus the wave vector q plots for four particles are summarized in Figure 5.6. As for different particles, the characteristic decay time τ scales as q^{-2} as expected from the anticipated free diffusive behavior of the nanoparticles. For all four latex nanoparticle samples, the diffusion coefficient results measured by DDM are in good agreement with the estimated value calculated from the Stokes-Einstein equation as shown in Table 5.1. These results indicate DDM is reliable for measuring dynamics of nanoparticles in aqueous solution at higher concentration normally not handled by traditional method such as DLS. DDM provides a new and alternative way to measure dynamic diffusion.
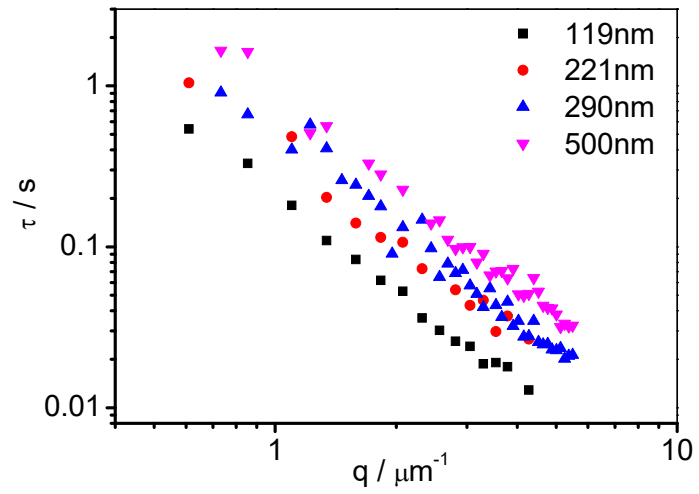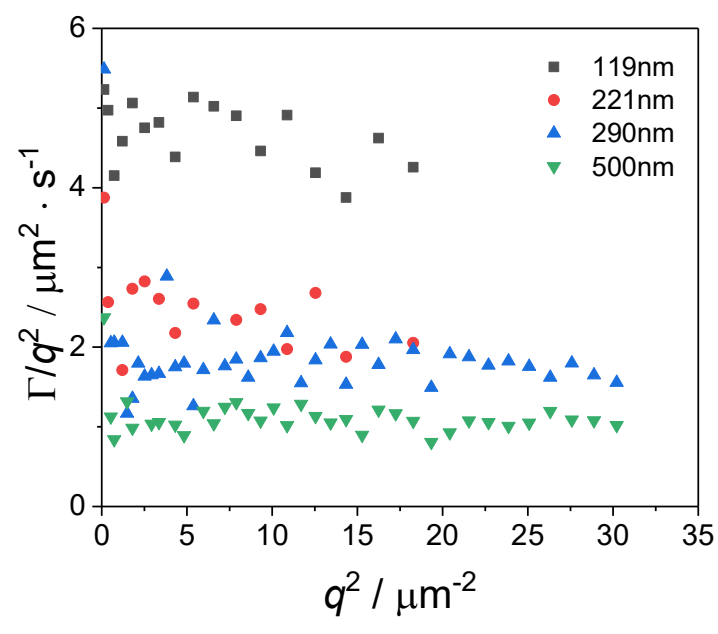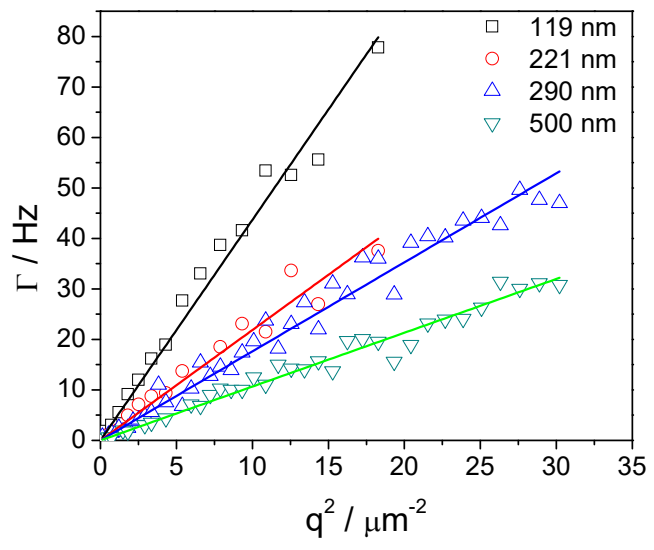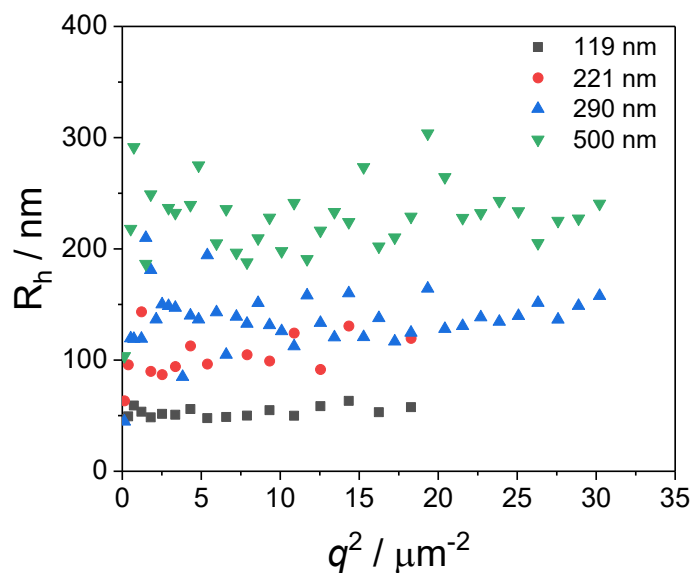
Figure 5.6. Summary of four particles with different diameters (119 nm, 221 nm, 290 nm and 500 nm).

Table 5.1. Diffusion coefficient results of DDM compared to expected theoretical values for four latex microspheres.

Particles/diameter nm	D (DDM) $\mu m^2/s$	D (Stokes-Einstein) $\mu m^2/s$
119	4.4 ± 0.1	4.1
210	2.19 ± 0.08	2.34
290	1.76 ± 0.03	1.69
500	1.07 ± 0.01	0.98

Here, several advantages of DDM over traditional light scattering technique such as DLS are highlighted. From the sample preparation point of view, DDM does not require dust-free samples and is immune to the static dust that is present in the sample as it can be subtracted off between two images by any intervals. This allows sample preparation for DDM to be much easier. Unlike DLS, any large particles or dust exist in the scattering volume would destroy the measurement, therefore DLS samples are often prepared and cleaned followed by specific procedures. In terms of colored materials, it is no problem for DDM because the light source used in experiments is incoherent such as LEDs, but often an issue as coherent laser source is common in DLS. Using the microscope as a platform for imaging in DDM provides multiple options with respect to images collection and contrast enhancement. In other words, bright-field, dark-field, and fluorescent microscope can be used for various samples. For bidisperse colloidal suspensions,[229] DDM enables measurement of diffusion of the little objects in the presence of big ones. It can even measure objects in the region of interest among inhomogeneous systems, which is challenging in DLS. The disadvantage of DDM is its inability to go to high q values, but in some applications this is an advantage. The information obtained from DDM could be complementary to that from DLS. Working at low q in DDM increases the possibility to provide high-resolution polydispersity analysis via Laplace transforms.[229] DDM has been successfully applied to colloidal particles and protein aggregates but seems to be limited to real polymer in solutions, although the polymer has a molecular weight in the level of millions and high dn/dc.

5.3.2 Dynamics in a Region of Interest: Bubble Debris

Differential dynamic microscopy permits diffusive measurement of region of interest. Some cylindrical bubbles coated with CU membrane turn into spherical bubbles after applying partial vacuum to the container. They fall apart if overpressure is supplied to increase the solubility of dissolved gases. Generation of small debris is observed from micrograph (denoted by red arrows in Figure 5.7). Such tiny debris are believed to be bubbles of submicron size rather than large protein aggregates. Measuring their dynamics provides information about the size and its distributions. It is more challenging to use DLS due to existence of micrometer size spherical bubbles. The intensity of scattered light from large bubbles dominates. Taking advantage of DDM, the region of interest for those tiny debris is easily taken series of microscopic images. The corresponding dynamics therefore is recorded.

DDM experiments were performed on bubble debris shown in right below corner in Figure 5.7. Taking advantage of logarithmically sampled Δt with 10 points per decade according to the procedure of Germain, Leocmach and Gibaud,[230] results in the reduction of calculation time to a few minutes. The DDM matrix $|F_D(q, \Delta t)|^2$ and auto-correlation function $f(q, \Delta t)$ projected on Δt for different q are shown in Figure 5.8, indicating either exponential growth or decay behavior. Figure 5.8C represents $f(q, \Delta t)$ collapses when plotted as a function of $\Delta t q^2$. This scaling is compatible with a Brownian diffusive process. That is also confirmed when plotted $\tau(q)$ versus q and have a slope of -2 (Figure 5.9). Our measurements yield a diffusion coefficient of $D = 0.61$ μm^2/s. The apparent radius of bubble debris falls to ~ 400 nm.
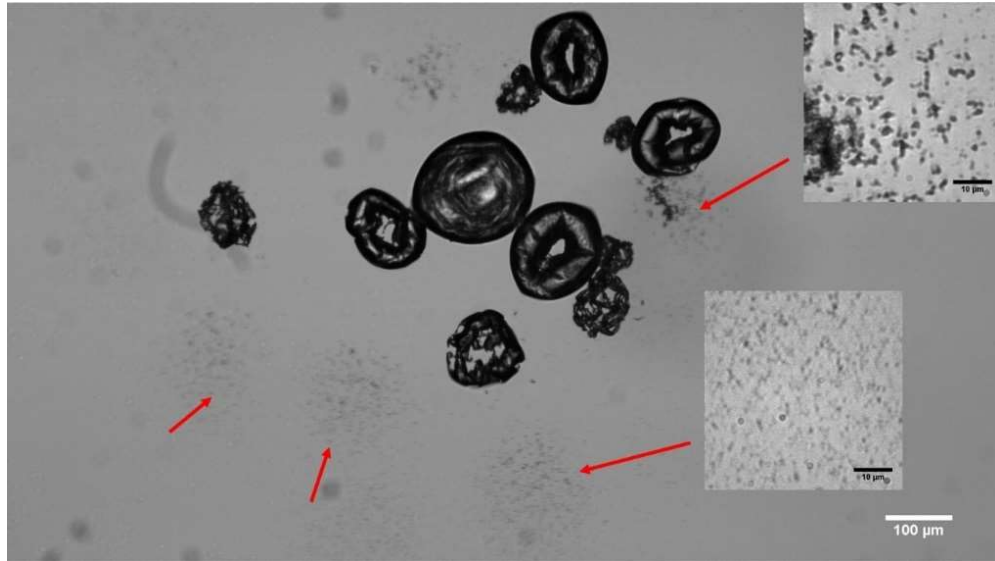
Figure 5.7. Spherical CU-coated air bubbles fall apart into small debris (arrow indicated) as overpressure is supplied. Inset images show zoom-in view of two bubbles after falling apart.

A

B
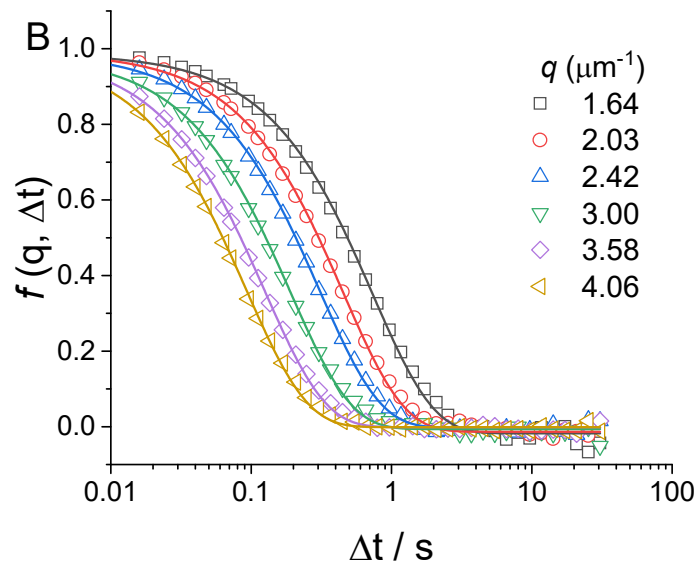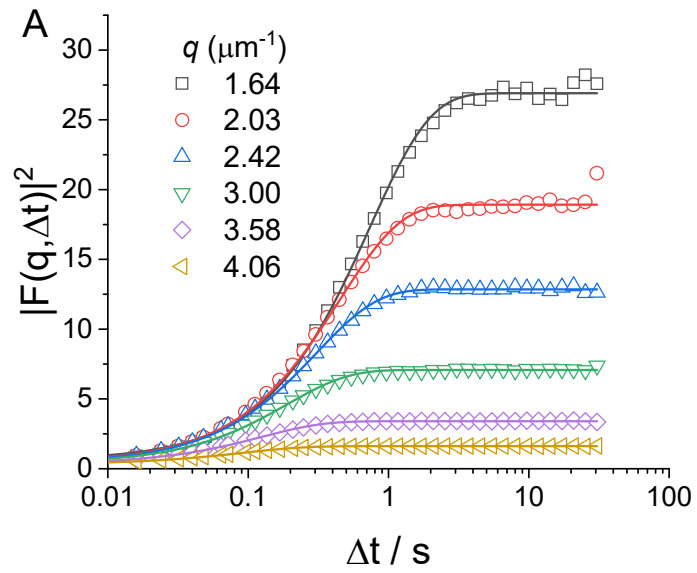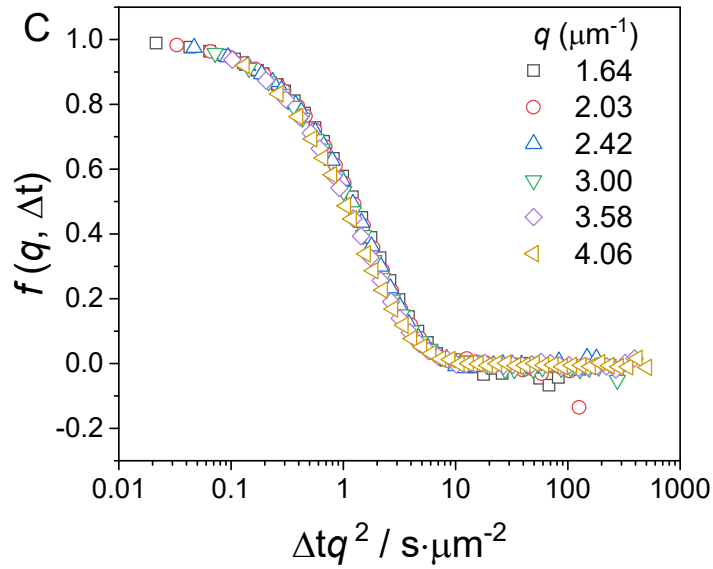
Figure 5.8 DDM results from bubbles debris in Figure 5.7. (A) Growth of $|F_D(q, \Delta t)|^2$ **with delay time** Δt **for three values of** q **(μm^{-1}). The continuous lines are fits of the data to Equation 5.4. (B) Auto-correlation function** $f(q, \Delta t)$ **extracted from** $|F_D(q, \Delta t)|^2$ **at various** q **versus** Δt**. Lines are exponential fits to the data according to Equation 5.4. (C)** $f(q, \Delta t)$ **at various** q **rescaled as a function of** $\Delta t q^2$**.**
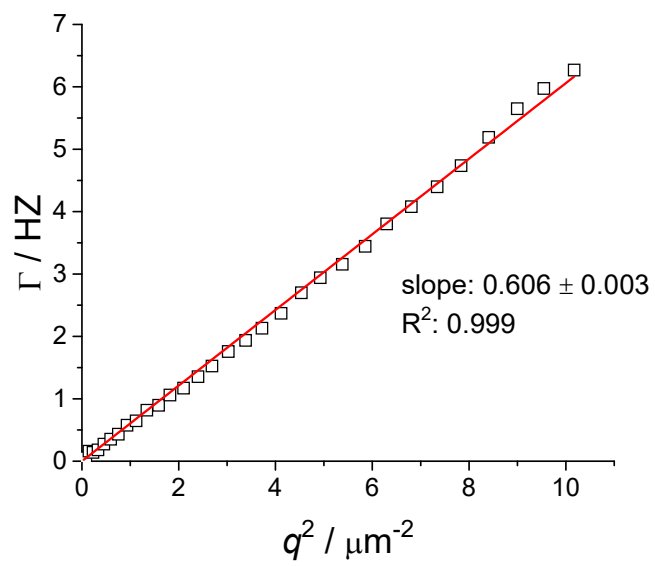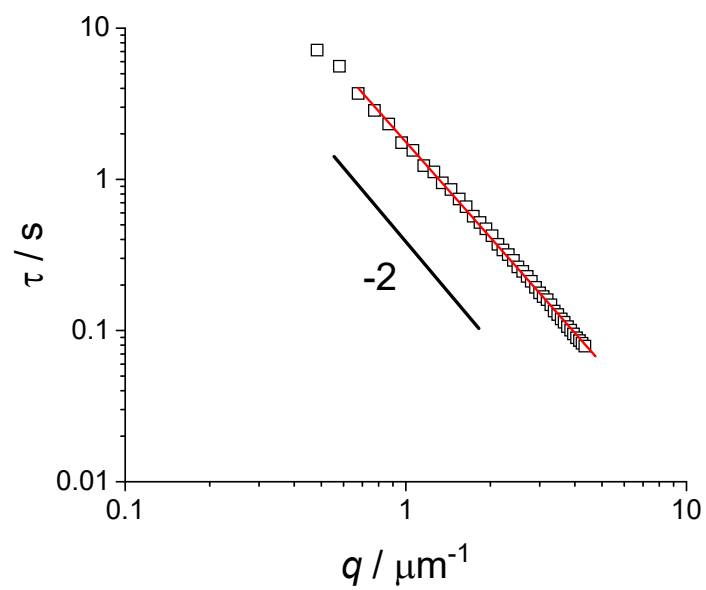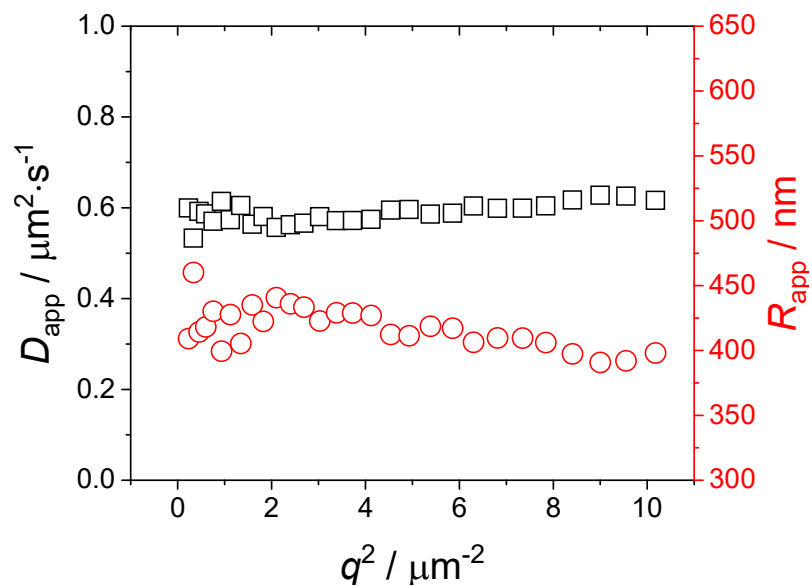
Figure 5.9 The bubble debris indicates characteristic Brownian diffusion behaviors and shows a uniform size of 400 nm in radius.

Figure 5.10 depicts a sequence of optical microscopic images recorded by a fast camera as spherical CU bubbles fall apart. Different morphological transitions were observed during bubble dissolution. Debris kept fluctuating spatially for many minutes. After further dissolution, 3000 images were captured to determine the dynamic of those debris by DDM.
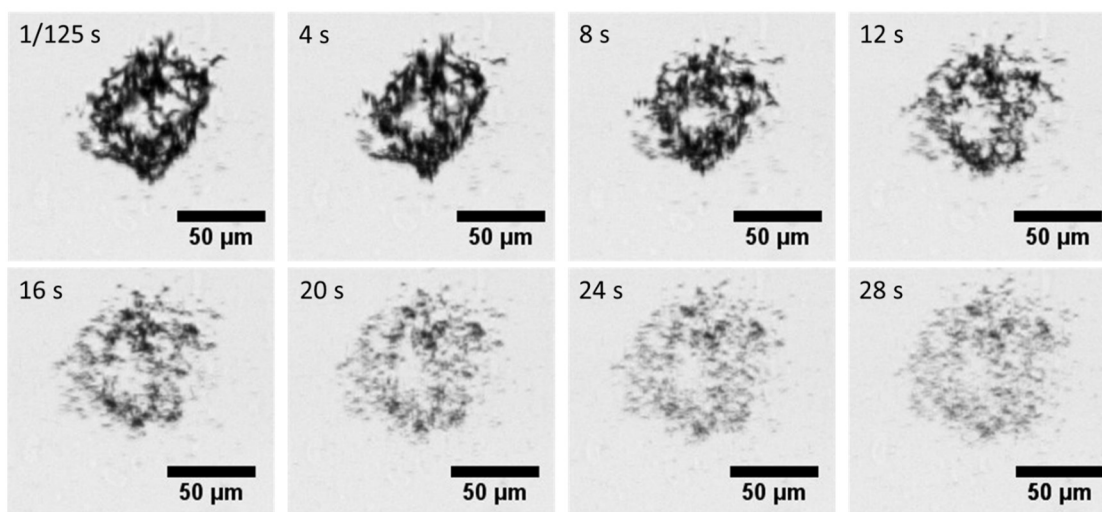
Figure 5.10. An example of time series of DDM micrographs denoting generation of bubble debris under overpressure. The frame rate was set at 125 frames per second. 3000 images were taken and DDM was calculated by averaging 1000 images statistically.

5.3.3 *Dynamics of Latex Nanoparticles in Confined Media (CU Oil Droplet)*

CU has shown the ability to encapsulate hydrocarbon oil into cylindrical droplets in aqueous dispersion. Therefore, water-insoluble colloidal particles or polymers can be dispersed into aqueous environment. Earlier experiments show toluene evaporates away from CU encapsulated toluene droplets as time proceeds (as shown in Figure 5.11). The droplets flatten and CU membranes are left behind and disappear eventually.

These behaviors can promote organic solvent evaporation-assisted alignment of encapsulated particles or polymers. Fluorescent C18 (stearyl alcohol) particles and rod-like polymer such as poly(γ-stearyl-L-glutamate) (PSLG) have been tried (Figure 5.12). The toluene-filled CU droplets containing fluorescent C18 particles deform and collapse over the time. No clear organization or alignment of particles is seen. Birefringence of PSLG under cross-polarized microscope becomes apparent as time progresses due to the evaporation of toluene from the droplets.
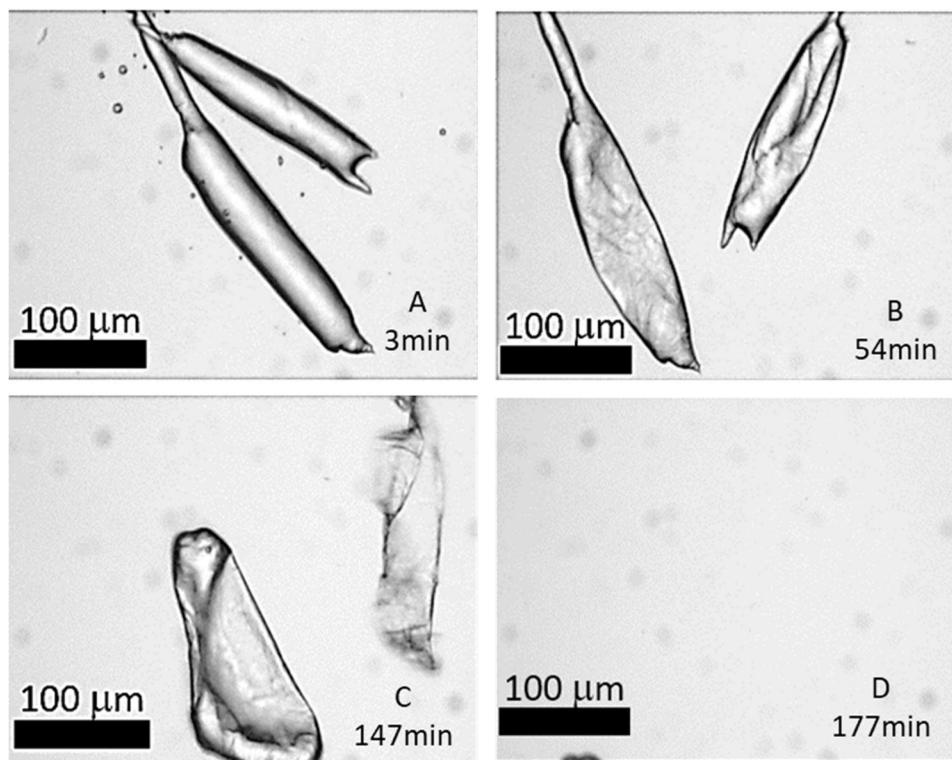
Figure 5.11. Toluene evaporates away from toluene-filled CU droplets.
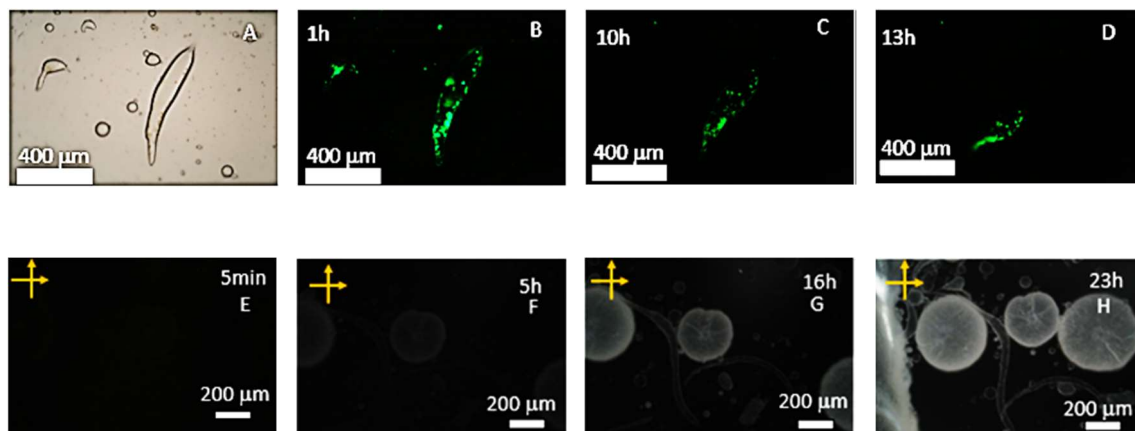
Figure 5.12. Bright-field (A) and epifluorescence microscopy images (B to D) of fluorescent C18 particles and cross-polarized microscopy images of rod-like PSLG polymer (E to H) in toluene-filled CU droplets as a function of time.

Early studies show CU/water dispersion is known to form oil droplets when gently agitated with a small amount of nonpolar solvent layered on top of the sample. Hydrophobic particles are anticipated to be encapsulated inside of CU oil droplet after introducing them to the nonpolar solvent. The results confirm it. Commercial cross-linked poly(styrene/ 41% divinylbenzene) are hydrophobic and coated by surfactants to be well dispersed in water. After removal of surfactants on the particles surface and solvent exchange, PS/DVB are well dispersed in a binary mixture of 1-octanol and toluene by a ratio of 1:10 v/v. Figure 5.13 shows typical toluene-filled CU oil-droplets. They are in fat, sausage-like shapes. 1.54 μm PS/DVB particles are evidently encapsulated inside of oil droplets. Aging time affects significantly the morphological of CU oil droplets. The evaporation of toluene from the capsules is related to changes in morphology. The oil

droplets become smaller as aging time progresses. On the other hand, encapsulated PS/DVB particles tend to become close to each other in packed fashion, in comparison with big distances between each other at short aging times. They are more packed at long times as shown in Figure 5.13E. After further aging, the particles stopped moving as judged by naked eyes. The relevant dynamics are expected to be slower and eventually lose the feature of Brownian motion. Here, DDM was used to monitor the dynamics of PS/DVB particles encapsulated inside of CU toluene-filled droplet at each aging time.
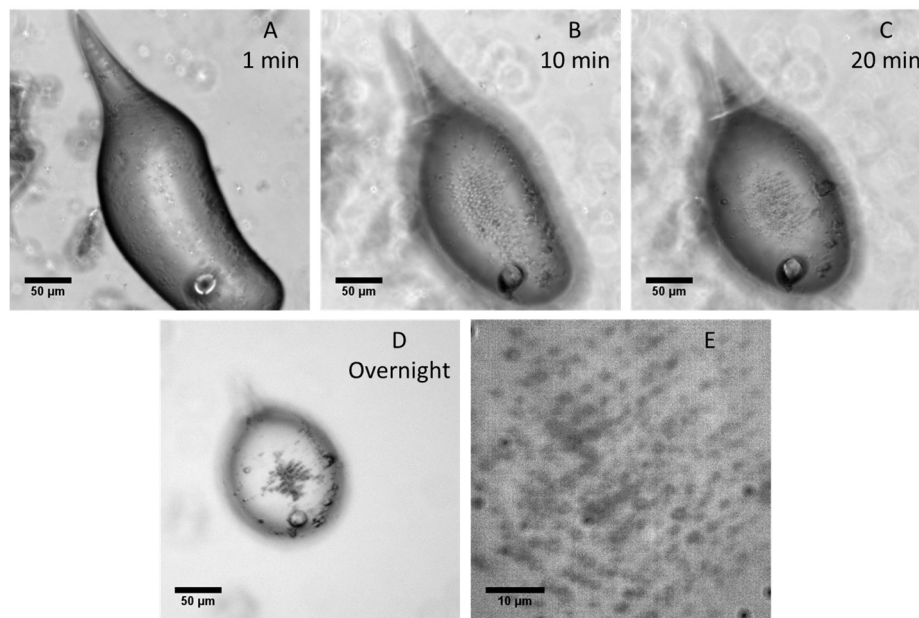
Figure 5.13. Hydrophobic particles, cross-linked poly(styrene/divinylbenzene) with a diameter of 1.54 μm, were encapsulated toluene-filled CU droplet. (A, B, C, and D), optical microscopic images of encapsulations as a function of time. (E), a zoom-in view of particles inside of encapsulations.

As control experiments, DDM was first performed on PS/DVB particles that were dispersed in toluene and drawn into a capillary glass tube. The representative image structure functions grow monotonically as a function of separation time for different values of wave vector q. The measured diffusion coefficient of PS/DVB particles is 0.35 ± 0.01 $\mu m^{-2}/s$. Next, similar DDM procedure was conducted on PS/DVB inside of CU toluene droplet. The corresponding measured diffusivity of PS/DVB in confined media is 0.34 ± 0.01 $\mu m^{-2}/s$.

Figure 5.14 summarizes characteristic Brownian decay rate (inverse of characteristic relaxation time) at various q^2 as a function of aging time of CU droplet for another individual experiment. The slope of Γ vs. q^2 plot exhibits insignificant changes at first a few hours, meaning the evaporation of toluene is slow and has not impacted the PS/DVB particles' diffusion. Nevertheless, the oil droplet becomes smaller in size and starts to return to the spherical shape and a declined trend in diffusion coefficient is observed as the toluene evaporates away from droplet at longer aging time, indicating the diffusion of PS/DVB particles becomes slower. This confirms the confinement environment due to solvent evaporation has caused the slowdown of particles' diffusion dispersed in the confinement. At even longer time beyond 12 h, the diffusion coefficient is not measurable and becomes close to zero, suggesting no diffusive dynamics exist at this point.
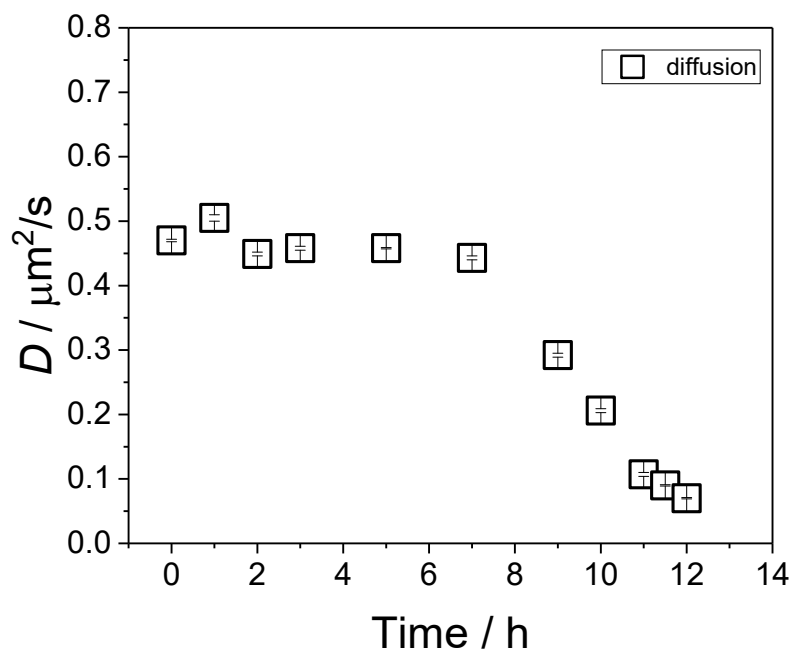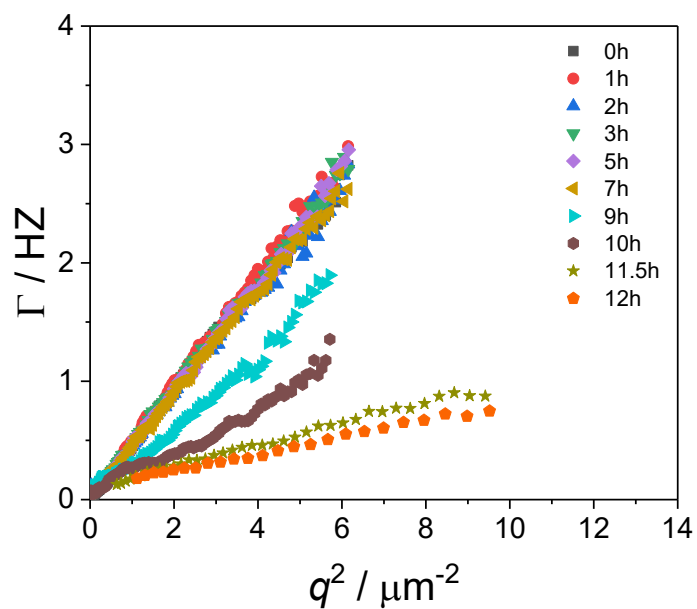
Figure 5.14. Diffusivity of PS/DVB in toluene droplet confined by CU membrane as a function of aging time.

5.4 Conclusion

CU-stabilized oil droplets sometimes exhibit solid-like interfaces. The high interfacial modulus allows long term stability of and oil droplets. Under certain circumstances, such as solvent evaporation, the oil droplets reconfigure their shape or size, confining the organization/packing of the particles dispersed inside droplet. Such systems complicate size determination of these particles by dynamic light scattering or even particle tracking. Instead, differential dynamic microscopy is suitable for measuring local diffusive dynamics of particles. The results show the particles freely follow Brownian diffusion at short time but lost their diffusive dynamics at long times due to solvent evaporation inside confinement. DDM proves to be an easy and powerful technique for such study. This suggests potential for applications such as controlled drug release from large vesicles.

CHAPTER 6.   CONCLUSIONS AND FUTURE WORK

6.1   Conclusions

This dissertation has presented detailed measurements and characterization of air bubbles and oil droplets coated by surface-active hydrophobin, *Cerato-ulmin* (CU). Producing bubbles and droplets coated with CU was explored by starting with a variety of gases and organic solvent. CU is not fussy about forming bubbles. It requires a tiny, hard-to-weigh speck of dry CU added to 1 mL of water and agitation of the container by gently rocking back and forth. The "solution" becomes opaque and turbid although CU is scarcely soluble at the molecular level. The experiments are reproducible by agitation and sonication (bath sonication destroys bubbles to "reset" the system). The formation of bubbles coated with CU is efficient even at a dilute concentration of 0.02 mg/mL. It is as easy to produce blobs as bubbles: one merely layers a nonpolar organic solvent atop the CU solution and agitates the container. Hexane, dodecane, and toluene were easily trapped and encapsulated. Both bubbles and blobs are in unusual cylindrical shapes with aspect ratios of length:width up to 35 and 5, respectively. No other hydrophobin systems reproducibly produce such structures. Then experiments were performed over different range of pH, temperature and pressure. Some rods have turned into spherical bubbles after applying partial vacuum to the container. They fall apart if overpressure is supplied to increase the solubility of dissolved gases. The cylindrical blobs are less compressible compared to bubbles and retain their shape with pressure change. After further expansion followed by release of tension, crinkled bubbles remain, suggesting CU molecules have

assembled at the interface and formed a strong membrane. Big bubbles are in millimeter-size and visible in an optical microscope. Submicron bubbles are detected by dynamic light scattering. They are initially around 600 nm in radius, decreasing to 200 nm over a period of several hours. Those nanobubbles are stable and remain for a month.

Chapter 3 described a facile method to produce stable sub-millimeter toroidal bubbles and provided possible mechanisms of the non-equilibrium shapes. Unlike other phospholipid vesicles produced by osmotic pressure, producing CU air-filled toroidal bubbles simply relies on atmospheric pressure changes. Manipulation of pressure in a prescribed sequence introduces shape transitions of the bubbles from cylinders to spheres and ultimately torus. The stable air-filled tori are in the scale of 100 μm and the major-to-minor radius ratio of the majority toroidal bubbles is 1.41, known as Clifford torus. Non-axisymmetric circular torus, known as Dupin cyclides, are also found and have a mean eccentricity of 0.20 ± 0.03. The size of the toroidal bubbles are correlated to the differential values between inside and outside pressures. A critical differential pressure window was found. The bending elasticity and curvature theories were applied to the formation of toroidal shapes.

The stability of bubbles and droplets coated with CU led us to study the behavior of CU at interfaces (Chapter 4). The adsorption of CU solutions at air-water and squalane-water interfaces has been characterized using a home-built microtensiometer at CMU. The interfacial tension at both interfaces were reduced by CU, even at a low concentration of 2 μg/mL (0.26 μM), but adsorption is slow in either case. Hours or minutes were required to reach steady interfacial tension values. The measured dilatational modulus at the air-water interface was 764 ± 45 mN/m, while the CU-adsorbed squalane-water interface is not as

rigid as the air-water interface but still shows very high stiffness with a dilatational modulus of 339 ± 19 mN/m. Those values indicate interface about ten times stronger than those formed by traditional surfactant molecules. CU adsorption is irreversible, exhibiting no significant desorption upon fluid exchange with deionized water. The protein film remains rigid and incompressible after fluid exchange. The sodium dodecyl sulfate (SDS) is added to CU solution as a competing component, SDS co-adsorbs to the preformed CU membrane. For SDS concentrations greater than 0.32 mM (critical micelle concentration, CMC, equals 8.2 mM), the surface pressure increases with SDS concentration while the dilatational modulus decreases, indicating SDS is adsorbing to the interface and decreasing the rigidity of the CU membrane. Exchanging the bulk solution with deionized water after exposing the CU membrane to SDS reveals behavior that strongly depends on SDS concentration. At high SDS concentrations near the CMC, the surface pressure and dilatational modulus decrease substantially upon rinsing, indicating the nearly total desorption of CU and SDS. At moderate concentrations, some SDS remains adsorbed on the surface with CU, creating a mixed layer that retains an extremely large dilatational modulus. SDS can both disrupt and displace a preformed CU film as well as contribute to a mixed adsorption layer.

The final research explored the delivery of hydrophobic molecules by taking advantage of CU's ability to encapsulate nonpolar organics. An analytical method based on image enhancement, differential dynamic microscopy (DDM), was used to track the dynamics of the particles. The results show CU can efficiently deliver hydrophobic particles and molecules in nonpolar solvents to aqueous solutions. The solid-like interfaces confining the particles and solvent retain enough flexibility to reconfigure their shape and

size during solvent evaporation. The particles freely follow Brownian diffusion soon after encapsulation, but lose diffusive motion as the solvent evaporates.

6.2   Future Work

Future work will be aimed at extending further exploration based on what has been found in this dissertation.

6.2.1   Coalescence Behaviour for Air Bubble and Oil Droplet Coated by CU

Rarely, coalescence of expanded spherical bubbles occurs, whereas cylindrical bubbles never do possibly due to the thicker membrane. Figure 6.1 shows dumbbell and "T"-shape fused bubbles. They retain their unusual shapes both during the inflation and deflation. Our early studies show the solid-like CU membrane is attributed to the shape stability of a single bubble in Chapter 4. Continuous collaborating with Prof. Lynn Walker and Prof. Shelly Anna and using the modified two-capillary microtensiometer platform would allow future workers to characterize the coalescence behaviour between two air bubbles or oil droplets. Interfacial properties, such as coalescence time, interfacial tension and elasticity would be measured to help understand the mechanism of air bubble/oil droplet stability. The findings would provide more insight into application of CU hydrophobin as an emulsifier.
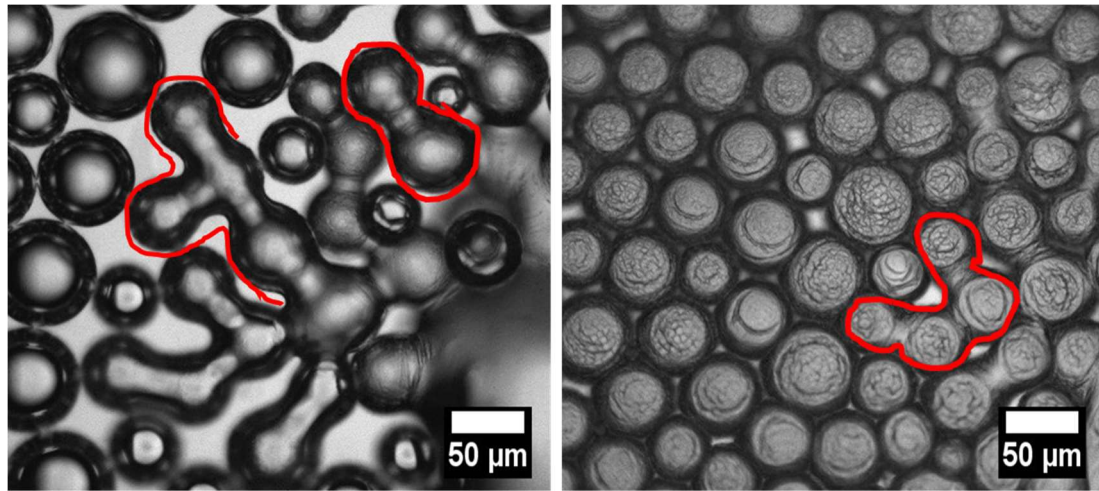
Figure 6.1. Bubble coalescence.

6.2.2 *Correlation of the Collapse Pressure and Toroidal Bubble Formation*

The formation of toroidal CU bubbles was achieved by application of pressure in a prescribed sequence (Chapter 3). Finding the critical pressure at which the crumpled bubbles start to rupture before full dissolving is the key to generating the holes of the toroidal bubbles. This pressure level acts as the upper limit while deflating the bubbles (Figure 6.2). On the other hand, locating the critical pressure at which the toroidal bubbles turn into full spheres is also important. This pressure level sets the lower limit during the inflation. The relationship between critical pressure and radius of the bubbles will be determined as well as the various morphological regimes. Understanding those correlations would provide a roadmap/procedure for mass production of toroidal bubbles.
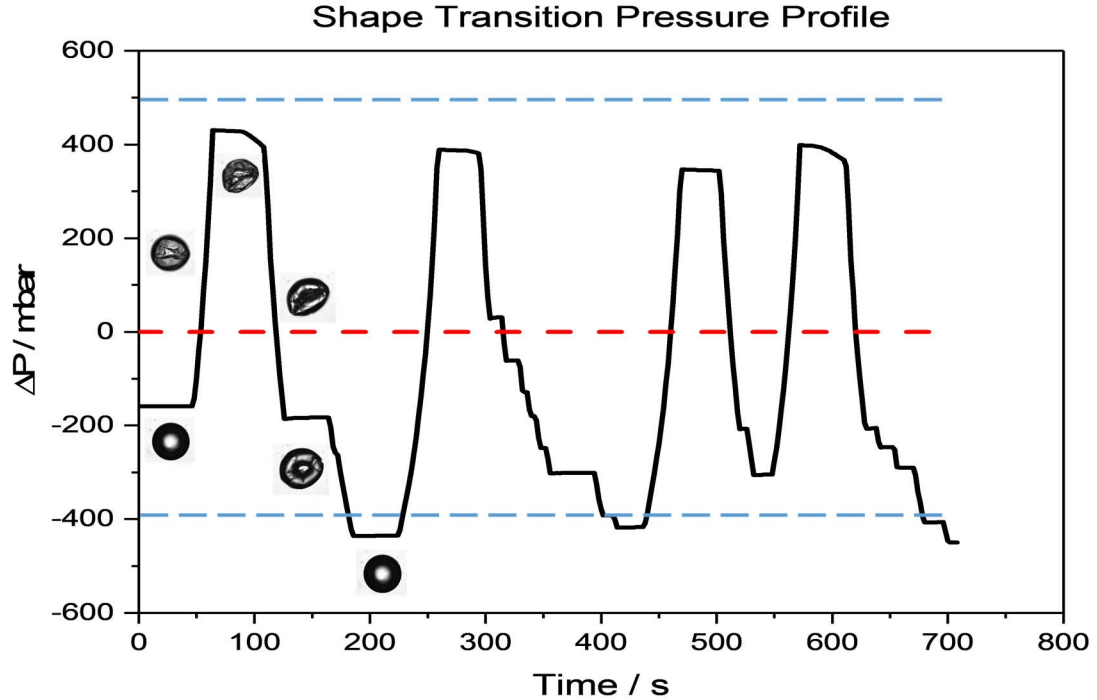
Figure 6.2. Four cycles of pressure manipulations. The red dashed line denotes ambient pressure, and two blue ones represent ideal upper and lower pressure limits. Bubble fully dissolves above the upper limit and transforms to spherical shape below the lower limit.

6.2.3 Wrinkling of the Pressurized CU-Coated Elastic Shell

Wrinkling of the bubbles surface during the deflation would be another subject of interest. (Figure 6.3). Future study would be focused on presenting scaling laws for the critical pressure at which wrinkling occurs, the position and number of wrinkles in terms of applied pressure, and mechanical properties of CU-coated elastic shell.

inflation = increasing internal pressure
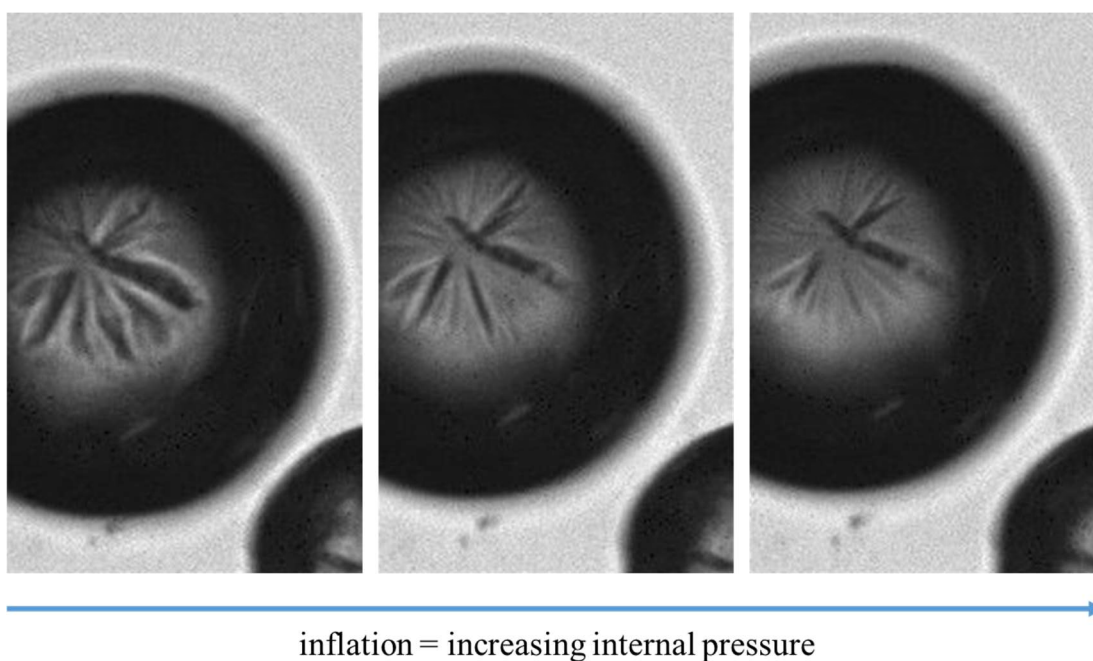
Figure 6.3. Wrinkling of the pressurized CU-coated elastic shell.

6.2.4   Polymerization in CU Droplets

Polymerization of oil-soluble monomer inside of CU droplets is also of interest. Styrene is a good choice as the model monomer. Here styrene monomer with initiator azobisisobutyronitrile (AIBN) and fluorescent C18-coated silica was encapsulated by CU and heated at 70 °C for 14 hours. Optical and epifluorescence images of the single CU droplets containing the styrene monomer illustrate the deformation of droplet after polymerization (Figure 6.4). Future study is required to confirm *in-situ* polymerization in

the droplet. Particle tracking, or DDM discussed in Chapter 5, would be used to track the fluorescent particles inside CU droplet as the polymerization proceeds. Physical properties of synthesized polystyrene, such as molecular weight, melting or glass transition temperature and morphology, would be further characterized by Gel Permeation Chromatography (GPC), Differential Scanning Calorimetry (DSC) and Scanning Electron Microscopy (SEM). Other strategies to demonstrate that polymerization occurred include washing the objects with sodium dodecyl sulfate (SDS) and alcohol which are proved to disrupt the CU membrane. If the objects retain intact, it is likely the polymerization has succeed.
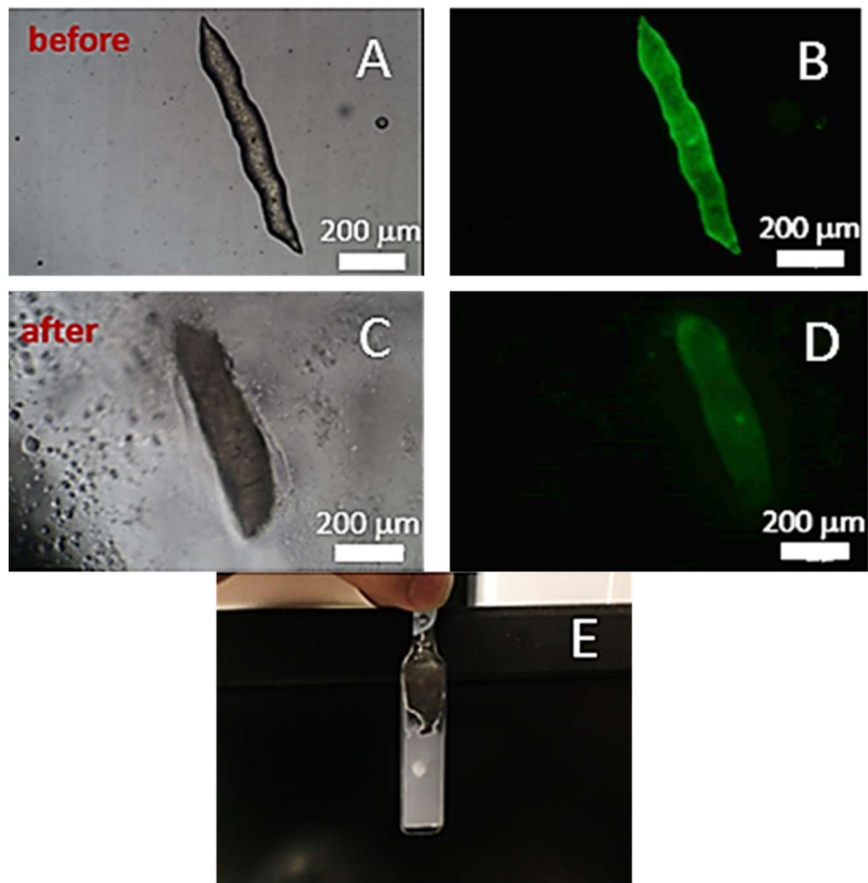
Figure 6.4. Optical and epifluorescence images of CU droplet containing styrene and fluorescent C18-Silica before (A and B) and after polymerization (C and D). Milky solution after polymerization (E).

6.2.5   Cross-linking of Shells

Although the unusual air bubbles (cylindrical, spherical, and toroidal ones) and sausage-like oil droplet remain long enough in the solutions for hours or days, it is desirable to preserve their structures or shapes permanently for practical applications such as light-weight materials, contrast agents and etc. One strategy is to chemically crosslink the shells

of the objects. In general, four functional groups in the proteins are accountable for crosslinking despite the complexity of amino acid sequence and composition. They are primary amines (-NH$_2$), carboxyls (-COOH), sulfhydryls (-SH) and carbonyls (-CHO). Among the amino acid composition of CU (Table 6.1), five reactive crosslinking targets exist including one Lysine (Lys) and four aspartic acid (Asp). Aldehydes and carbodiimides are common reactive reagents. Other specific reagents are also available. The crystallography of CU is not understood yet. Crosslinking CU shells may be expected to be challenging because the locations of reactive groups are unknown, either on the surface or in the core, in terms of the protein structure.

Table 6.1. Amino acid sequence of *Cerato-ulmin*.[91]

Ser. Asp. Ser. Tyr. Asp. Pro. Cys. Thr. Gly. Leu. Leu. Gln. Lys. Ser. Pro. Gln. Cys. Cys. Asn. Thr. Asp. Ile. Leu. Gly. Val. Ala. Asn. Leu. Asp. Cys. His. Gly. Pro. Pro. Ser. Val. Pro. Thr. Ser. Pro. Ser. Gln. Phe. Gln. Ala. Ser. Cys. Val. Ala. Asp. Gly. Gly. Arg. Ser. Ala. Arg. Cys. Cys. Thr. Leu. Ser. Leu. Leu. Gly. Leu. Ala. Leu. Val. Cys. Thr. Asp. Pro. Val. Gly. Ile.

REFERENCES

1.   Schuren, F. H. J.; Wessels, J. G. H., Two genes specifically expressed in fruiting dikaryons of Schizophyllum commune: homologies with a gene not regulated by mating-type genes. *Gene* **1990,** *90* (2), 199-205.

2.   Tablas de marea. Centro de Investigacion Cientifica y de Educacion Superior de EnsenadaWessels, J.; De Vries, O.; Asgeirsdottir, S. A.; Schuren, F., Hydrophobin Genes Involved in Formation of Aerial Hyphae and Fruit Bodies in Schizophyllum. *Plant Cell* **1991,** *3* (8), 793-799.

3.   Wösten, H. A. B., Hydrophobins: Multipurpose Proteins. *Annu. Rev. Microbiol.* **2001,** *55* (1), 625-646.

4.   Hektor, H. J.; Scholtmeijer, K., Hydrophobins: proteins with potential. *Curr. Opin. Biotechnol.* **2005,** *16* (4), 434-439.

5.   Cox, P. W.; Hooley, P., Hydrophobins: New prospects for biotechnology. *Fungal Biology Reviews* **2009,** *23* (1–2), 40-47.

6.   Wösten, H. B.; Scholtmeijer, K., Applications of hydrophobins: current state and perspectives. *Appl. Microbiol. Biotechnol.* **2015,** *99* (4), 1587-1597.

7.   Wösten, H. A. B.; van Wetter, M.-A.; Lugones, L. G.; van der Mei, H. C.; Busscher, H. J.; Wessels, J. G. H., How a fungus escapes the water to grow into the air. *Curr. Biol.* **1999,** *9* (2), 85-88.

8.   Wösten, H. B.; Wessels, J. H., Hydrophobins, from molecular structure to multiple functions in fungal development. *Mycoscience* **1997,** *38* (3), 363-374.

9.   Ebbole, D. J., Hydrophobins and fungal infection of plants and animals. *Trends Microbiol.* **1997,** *5* (10), 405-408.

10.   Wessels, J. G., Fungal hydrophobins: proteins that function at an interface. *Trends Plant Sci.* **1996,** *1* (1), 9-15.

11.   Wösten, H. A. B.; de Vocht, M. L., Hydrophobins, the fungal coat unravelled. *Biochimica et Biophysica Acta (BBA) - Reviews on Biomembranes* **2000,** *1469* (2), 79-86.

12.   Linder, M. B.; Szilvay, G. R.; Nakari-Setala, T.; Penttila, M. E., Hydrophobins: the protein-amphiphiles of filamentous fungi. *FEMS Microbiol. Rev.* **2005,** *29* (5), 877-96.

13.   Kyte, J.; Doolittle, R. F., A simple method for displaying the hydropathic character of a protein. *J. Mol. Biol.* **1982,** *157* (1), 105-132.

14.   Wessels, J. G. H.; De Vries, O. M. H.; Ásgeirsdóttir, S. A.; Springer, J., The thn mutation of Schizophyllum commune, which suppresses formation of aerial hyphae, affects expression of the Sc3 hydrophobin gene. *Microbiology* **1991,** *137* (10), 2439-2445.

15.   Russo, P. S.; Blum, F. D.; Ipsen, J. D.; Abul-Hajj, Y. J.; Miller, W. G., The solubility and surface activity of the Ceratocystis ulmi toxin cerato-ulmin. *Physiol. Plant Pathol.* **1981,** *19* (1), 113-126.

16.   Hakanpaa J Fau - Linder, M.; Linder M Fau - Popov, A.; Popov A Fau - Schmidt, A.; Schmidt A Fau - Rouvinen, J.; Rouvinen, J., Hydrophobin HFBII in detail: ultrahigh-resolution structure at 0.75 A. **2006,** (0907-4449 (Print)), 356-367.

17.   Hakanpää, J.; Paananen, A.; Askolin, S.; Nakari-Setälä, T.; Parkkinen, T.; Penttilä, M.; Linder, M. B.; Rouvinen, J., Atomic Resolution Structure of the HFBII Hydrophobin, a Self-assembling Amphiphile. *J. Biol. Chem.* **2004,** *279* (1), 534-539.

18.   Linder, M. B., Hydrophobins: Proteins that self assemble at interfaces. *Curr. Opin. Colloid Interface Sci.* **2009,** *14* (5), 356-363.

19.   Kwan, A. H.; Winefield, R. D.; Sunde, M.; Matthews, J. M.; Haverkamp, R. G.; Templeton, M. D.; Mackay, J. P., Structural basis for rodlet assembly in fungal hydrophobins. *Proc Natl Acad Sci U S A* **2006,** *103* (10), 3621-6.

20.   Fan, H.; Wang, X.; Zhu, J.; Robillard, G. T.; Mark, A. E., Molecular dynamics simulations of the hydrophobin SC3 at a hydrophobic/hydrophilic interface. *Proteins: Structure, Function, and Bioinformatics* **2006,** *64* (4), 863-873.

21.   Morris, V. K.; Kwan, A. H.; Sunde, M., Analysis of the Structure and Conformational States of DewA Gives Insight into the Assembly of the Fungal Hydrophobins. *J. Mol. Biol.* **2013,** *425* (2), 244-256.

22.   Rey, A. A.; Hocher, A.; Kwan, A. H.; Sunde, M., Backbone and sidechain 1H, 13C and 15N chemical shift assignments of the hydrophobin MPG1 from the rice blast fungus Magnaporthe oryzae. *Biomolecular NMR Assignments* **2013,** *7* (1), 109-112.

23.   Pille, A.; Kwan, A. H.; Cheung, I.; Hampsey, M.; Aimanianda, V.; Delepierre, M.; Latgé, J.-P.; Sunde, M.; Guijarro, J. I., 1H, 13C and 15N resonance assignments of the RodA hydrophobin from the opportunistic pathogen Aspergillus fumigatus. *Biomolecular NMR Assignments* **2015,** *9* (1), 113-118.

24.   Hakanpää, J.; Szilvay, G. R.; Kaljunen, H.; Maksimainen, M.; Linder, M.; Rouvinen, J., Two crystal structures of Trichoderma reesei hydrophobin HFBI—The structure of a protein amphiphile with and without detergent interaction. *Protein Sci.* **2006,** *15* (9), 2129-2140.

25.   Ren, Q.; Kwan, A. H.; Sunde, M., Solution structure and interface-driven self-assembly of NC2, a new member of the Class II hydrophobin proteins. *Proteins: Structure, Function, and Bioinformatics* **2014,** *82* (6), 990-1003.

26.   Torkkeli, M.; Serimaa, R.; Ikkala, O.; Linder, M., Aggregation and Self-Assembly of Hydrophobins from Trichoderma reesei: Low-Resolution Structural Models. *Biophys. J.* **2002,** *83* (4), 2240-2247.

27.   Kisko, K.; Szilvay, G. R.; Vainio, U.; Linder, M. B.; Serimaa, R., Interactions of Hydrophobin Proteins in Solution Studied by Small-Angle X-Ray Scattering. *Biophys. J.* **2008,** *94* (1), 198-206.

28.   Szilvay, G. R.; Nakari-Setälä, T.; Linder, M. B., Behavior of Trichoderma reesei Hydrophobins in Solution: Interactions, Dynamics, and Multimer Formation†. *Biochemistry* **2006,** *45* (28), 8590-8598.

29.   Zhang, X. L.; Penfold, J.; Thomas, R. K.; Tucker, I. M.; Petkov, J. T.; Bent, J.; Cox, A.; Grillo, I., Self-Assembly of Hydrophobin and Hydrophobin/Surfactant Mixtures in Aqueous Solution. *Langmuir* **2011,** *27* (17), 10514-10522.

30.   Wang, X.; Graveland-Bikker, J. F.; De Kruif, C. G.; Robillard, G. T., Oligomerization of hydrophobin SC3 in solution: From soluble state to self-assembly. *Protein Sci.* **2004,** *13* (3), 810-821.

31.   Mackay, J. P.; Matthews, J. M.; Winefield, R. D.; Mackay, L. G.; Haverkamp, R. G.; Templeton, M. D., The hydrophobin EAS is largely unstructured in solution and functions by forming amyloid-like structures. *Structure* **2001,** *9* (2), 83-91.

32.   Longobardi, S.; Picone, D.; Ercole, C.; Spadaccini, R.; Stefano, L. D.; Rea, I.; Giardina, P., Environmental Conditions Modulate the Switch among Different States of the Hydrophobin Vmh2 from Pleurotus ostreatus. *Biomacromolecules* **2012,** *13* (3), 743-750.

33.   Paslay, L. C.; Falgout, L.; Savin, D. A.; Heinhorst, S.; Cannon, G. C.; Morgan, S. E., Kinetics and Control of Self-Assembly of ABH1 Hydrophobin from the Edible White Button Mushroom. *Biomacromolecules* **2013,** *14* (7), 2283-2293.

34.   Wohlleben, W.; Subkowski, T.; Bollschweiler, C.; von Vacano, B.; Liu, Y.; Schrepp, W.; Baus, U., Recombinantly produced hydrophobins from fungal analogues as highly surface-active performance proteins. *Eur. Biophys. J.* **2010,** *39* (3), 457-68.

35.   Takai, S., Pathogenicity and cerato-ulmin production in Ceratocystis ulmi. *Nature* **1974,** *252* (5479), 124-126.

36.   Wosten, H.; De Vries, O.; Wessels, J., Interfacial Self-Assembly of a Fungal Hydrophobin into a Hydrophobic Rodlet Layer. *Plant Cell* **1993,** *5* (11), 1567-1574.

37.   Beever, R. E.; Dempsey, G. P., Function of rodlets on the surface of fungal spores. *Nature* **1978,** *272* (5654), 608-610.

38.   Gebbink, M. F. B. G.; Claessen, D.; Bouma, B.; Dijkhuizen, L.; Wosten, H. A. B., Amyloids - a functional coat for microorganisms. *Nat Rev Micro* **2005,** *3* (4), 333-341.

39.   Butko, P.; Buford, J. P.; Goodwin, J. S.; Stroud, P. A.; McCormick, C. L.; Cannon, G. C., Spectroscopic Evidence for Amyloid-like Interfacial Self-Assembly of Hydrophobin Sc3. *Biochem. Biophys. Res. Commun.* **2001,** *280* (1), 212-215.

40.   Morris, V. K.; Sunde, M., Formation of Amphipathic Amyloid Monolayers from Fungal Hydrophobin Proteins. In *T Protein Nanotechnology*, 2012; Vol. 996, pp 119-129.

41.   Paananen, A.; Vuorimaa, E.; Torkkeli, M.; Penttilä, M.; Kauranen, M.; Ikkala, O.; Lemmetyinen, H.; Serimaa, R.; Linder, M. B., Structural Hierarchy in Molecular Films of Two Class II Hydrophobins†. *Biochemistry* **2003,** *42* (18), 5253-5258.

42.   de Vocht, M. L.; Scholtmeijer, K.; van der Vegte, E. W.; de Vries, O. M.; Sonveaux, N.; Wösten, H. A.; Ruysschaert, J. M.; Hadziloannou, G.; Wessels, J. G.; Robillard, G. T., Structural characterization of the hydrophobin SC3, as a monomer and after self-assembly at hydrophobic/hydrophilic interfaces. *Biophys. J.* **1998,** *74* (4), 2059-2068.

43.   Grunér, M. S.; Szilvay, G. R.; Berglin, M.; Lienemann, M.; Laaksonen, P.; Linder, M. B., Self-assembly of Class II Hydrophobins on Polar Surfaces. *Langmuir* **2012,** *28* (9), 4293-4300.

44.   de Vries, O. M. H.; Moore, S.; Arntz, C.; Wessels, J. G. H.; Tudzynski, P., Identification and characterization of a tri-partite hydrophobin from Claviceps fusiformis. *Eur. J. Biochem.* **1999,** *262* (2), 377-385.

45.   Askolin, S.; Linder, M.; Scholtmeijer, K.; Tenkanen, M.; Penttilä, M.; de Vocht, M. L.; Wösten, H. A. B., Interaction and Comparison of a Class I Hydrophobin from Schizophyllum commune and Class II Hydrophobins from Trichoderma reesei. *Biomacromolecules* **2006,** *7* (4), 1295-1301.

46.   Russo, P. S.; Blum, F. D.; Ipsen, J. D.; Abul-Hajj, Y. J.; Miller, W. G., The surface activity of the phytotoxin cerato-ulmin. *Can. J. Bot.* **1982,** *60* (8), 1414-1422.

47.   Basheva, E. S.; Kralchevsky, P. A.; Christov, N. C.; Danov, K. D.; Stoyanov, S. D.; Blijdenstein, T. B. J.; Kim, H.-J.; Pelan, E. G.; Lips, A., Unique Properties of Bubbles and Foam Films Stabilized by HFBII Hydrophobin. *Langmuir* **2011,** *27* (6), 2382-2392.

48.   Cox, A. R.; Aldred, D. L.; Russell, A. B., Exceptional stability of food foams using class II hydrophobin HFBII. *Food Hydrocoll* **2009,** *23* (2), 366-376.

49.   Cox, A. R.; Cagnol, F.; Russell, A. B.; Izzard, M. J., Surface Properties of Class II Hydrophobins from Trichoderma reesei and Influence on Bubble Stability. *Langmuir* **2007,** *23* (15), 7995-8002.

50.   Green, A. J.; Littlejohn, K. A.; Hooley, P.; Cox, P. W., Formation and stability of food foams and aerated emulsions: Hydrophobins as novel functional ingredients. *Curr. Opin. Colloid Interface Sci.* **2013,** *18* (4), 292-301.

51.   Ren, Q.; Kwan, A. H.; Sunde, M., Two forms and two faces, multiple states and multiple uses: Properties and applications of the self-assembling fungal hydrophobins. *Peptide Science* **2013**, n/a-n/a.

52.   Khalesi, M.; Gebruers, K.; Derdelinckx, G., Recent Advances in Fungal Hydrophobin Towards Using in Industry. *The Protein Journal* **2015,** *34* (4), 243-255.

53.   Taniguchi, S.; Sandiford, L.; Cooper, M.; Rosca, E. V.; Ahmad Khanbeigi, R.; Fairclough, S. M.; Thanou, M.; Dailey, L. A.; Wohlleben, W.; von Vacano, B.; T. M. de Rosales, R.; Dobson, P. J.; Owen, D. M.; Green, M., Hydrophobin-Encapsulated Quantum Dots. *ACS Applied Materials & Interfaces* **2016,** *8* (7), 4887-4893.

54.   Rosu, C.; Kleinhenz, N.; Choi, D.; Tassone, C. J.; Zhang, X.; Park, J. O.; Srinivasarao, M.; Russo, P. S.; Reichmanis, E., Protein-Assisted Assembly of π-Conjugated Polymers. *Chemistry of Materials* **2015**.

55.   Pigliacelli, C.; D'Elicio, A.; Milani, R.; Terraneo, G.; Resnati, G.; Baldelli Bombelli, F.; Metrangolo, P., Hydrophobin-stabilized dispersions of PVDF nanoparticles in water. *J. Fluorine Chem.* **2015,** *177*, 62-69.

56.   Khalesi, M.; Mandelings, N.; Herrera-Malaver, B.; Riveros-Galan, D.; Gebruers, K.; Derdelinckx, G., Improvement of the retention of ocimene in water phase using Class II hydrophobin HFBII. *Flavour Fragrance J.* **2015,** *30* (6), 451-458.

57.   Yang, W.; Ren, Q.; Wu, Y.-N.; Morris, V. K.; Rey, A. A.; Braet, F.; Kwan, A. H.; Sunde, M., Surface functionalization of carbon nanomaterials by self-assembling hydrophobin proteins. *Biopolymers* **2013,** *99* (1), 84-94.

58.   Wang, Z.; Wang, Y.; Huang, Y.; Li, S.; Feng, S.; Xu, H.; Qiao, M., Characterization and application of hydrophobin-dispersed multi-walled carbon nanotubes. *Carbon* **2010,** *48* (10), 2890-2898.

59.   Della Ventura, B.; Rea, I.; Caliò, A.; Giardina, P.; Gravagnuolo, A. M.; Funari, R.; Altucci, C.; Velotta, R.; De Stefano, L., Vmh2 hydrophobin layer entraps glucose: A quantitative characterization by label-free optical and gravimetric methods. *Appl. Surf. Sci.* **2016,** *364*, 201-207.

60.   Zhao, Z.-X.; Qiao, M.-Q.; Yin, F.; Shao, B.; Wu, B.-Y.; Wang, Y.-Y.; Wang, X.-S.; Qin, X.; Li, S.; Yu, L.; Chen, Q., Amperometric glucose biosensor based on self-assembly hydrophobin with high efficiency of enzyme utilization. *Biosensors Bioelectron.* **2007,** *22* (12), 3021-3027.

61.   Gravagnuolo, A. M.; Morales-Narváez, E.; Matos, C. R. S.; Longobardi, S.; Giardina, P.; Merkoçi, A., On-the-Spot Immobilization of Quantum Dots, Graphene Oxide, and Proteins via Hydrophobins. *Adv. Funct. Mater.* **2015,** *25* (38), 6084-6092.

62.   Gravagnuolo, A. M.; Morales-Narváez, E.; Longobardi, S.; da Silva, E. T.; Giardina, P.; Merkoçi, A., In Situ Production of Biofunctionalized Few-Layer Defect-Free Microsheets of Graphene. *Adv. Funct. Mater.* **2015,** *25* (18), 2771-2779.

63.   Laaksonen, P.; Kainlauri, M.; Laaksonen, T.; Shchepetov, A.; Jiang, H.; Ahopelto, J.; Linder, M. B., Interfacial Engineering by Proteins: Exfoliation and Functionalization of Graphene by Hydrophobins. *Angew. Chem. Int. Ed.* **2010,** *49* (29), 4946-4949.

64.   Mereghetti, P.; Wade, R., Diffusion of hydrophobin proteins in solution and interactions with a graphite surface. *BMC Biophysics* **2011,** *4* (1), 9.

65.   Kostiainen, M. A.; Szilvay, G. R.; Lehtinen, J.; Smith, D. K.; Linder, M. B.; Urtti, A.; Ikkala, O., Precisely Defined Protein–Polymer Conjugates: Construction of Synthetic DNA Binding Domains on Proteins by Using Multivalent Dendrons. *ACS Nano* **2007,** *1* (2), 103-113.

66.   Gazzera, L.; Corti, C.; Pirrie, L.; Paananen, A.; Monfredini, A.; Cavallo, G.; Bettini, S.; Giancane, G.; Valli, L.; Linder, M. B.; Resnati, G.; Milani, R.; Metrangolo, P., Hydrophobin as a Nanolayer Primer That Enables the Fluorinated Coating of Poorly Reactive Polymer Surfaces. *Advanced Materials Interfaces* **2015,** *2* (14), n/a-n/a.

67.   Varjonen, S.; Laaksonen, P.; Paananen, A.; Valo, H.; Hahl, H.; Laaksonen, T.; Linder, M. B., Self-assembly of cellulose nanofibrils by genetically engineered fusion proteins. *Soft Matter* **2011,** *7* (6), 2402-2411.

68.   Laaksonen, P.; Walther, A.; Malho, J.-M.; Kainlauri, M.; Ikkala, O.; Linder, M. B., Genetic Engineering of Biomimetic Nanocomposites: Diblock Proteins, Graphene, and Nanofibrillated Cellulose. *Angew. Chem. Int. Ed.* **2011,** *50* (37), 8688-8691.

69.   Iwanaga, A.; Asakawa, H.; Fukuma, T.; Nakamichi, M.; Shigematsu, S.; Linder, M. B.; Haruyama, T., Ordered nano-structure of a stamped self-organized protein layer on a HOPG surface using a HFB carrier. *Colloids Surf. B. Biointerfaces* **2011,** *84* (2), 395-399.

70.   Yamasaki, R.; Takatsuji, Y.; Lienemann, M.; Asakawa, H.; Fukuma, T.; Linder, M.; Haruyama, T., Electrochemical properties of honeycomb-like structured HFBI self-organized membranes on HOPG electrodes. *Colloids Surf. B. Biointerfaces* **2014,** *123* (0), 803-808.

71.   Longobardi, S.; Gravagnuolo, A. M.; Rea, I.; De Stefano, L.; Marino, G.; Giardina, P., Hydrophobin-coated plates as matrix-assisted laser desorption/ionization sample support for peptide/protein analysis. *Anal. Biochem.* **2014,** *449*, 9-16.

72.   Alongi, J.; Carletto, R. A.; Bosco, F.; Carosio, F.; Di Blasio, A.; Cuttica, F.; Antonucci, V.; Giordano, M.; Malucelli, G., Caseins and hydrophobins as novel green flame retardants for cotton fabrics. *Polym. Degradation Stab.* **2014,** *99* (0), 111-117.

73.   Schulz, A.; Liebeck, B. M.; John, D.; Heiss, A.; Subkowski, T.; Boker, A., Protein-mineral hybrid capsules from emulsions stabilized with an amphiphilic protein. *J. Mater. Chem.* **2011,** *21* (26), 9731-9736.

74.   Schulz, A.; Fioroni, M.; Linder, M. B.; Nessel, A.; Bocola, M.; Subkowski, T.; Schwaneberg, U.; Boker, A.; Rodriguez-Ropero, F., Exploring the mineralization of hydrophobins at a liquid interface. *Soft Matter* **2012,** *8* (44), 11343-11352.

75.   Burke, J.; Cox, A.; Petkov, J.; Murray, B. S., Interfacial rheology and stability of air bubbles stabilized by mixtures of hydrophobin and β-casein. *Food Hydrocoll* **2014,** *34* (0), 119-127.

76.   Wang, Y.; Bouillon, C.; Cox, A.; Dickinson, E.; Durga, K.; Murray, B. S.; Xu, R., Interfacial Study of Class II Hydrophobin and Its Mixtures with Milk Proteins: Relationship to Bubble Stability. *J. Agric. Food Chem.* **2013,** *61* (7), 1554-1562.

77.   Crilly, J. F.; Russell, A. B.; Cox, A. R.; Cebula, D. J., Designing Multiscale Structures for Desired Properties of Ice Cream. *Industrial & Engineering Chemistry Research* **2008,** *47* (17), 6362-6367.

78.   Sarlin, T.; Nakari-Setälä, T.; Linder, M.; Penttilä, M.; Haikara, A., Fungal Hydrophobins as Predictors of the Gushing Activity of Malt. *Journal of the Institute of Brewing* **2005,** *111* (2), 105-111.

79.   Christian, M.; Titze, J.; Ilberg, V.; Jacob, F., Novel Perspectives in Gushing Analysis: A Review. *Journal of the Institute of Brewing* **2011,** *117* (3), 295-313.

80.   Khalesi, M.; Deckers, S. M.; Gebruers, K.; Vissers, L.; Verachtert, H.; Derdelinckx, G., Hydrophobins: Exceptional proteins for many applications in brewery environment and other bio-industries. *Cerevisia* **2012,** *37* (1), 3-9.

81.   Valo, H.; Arola, S.; Laaksonen, P.; Torkkeli, M.; Peltonen, L.; Linder, M. B.; Serimaa, R.; Kuga, S.; Hirvonen, J.; Laaksonen, T., Drug release from nanoparticles embedded in four different nanofibrillar cellulose aerogels. *Eur. J. Pharm. Sci.* **2013,** *50* (1), 69-77.

82.   Valo, H. K.; Laaksonen, P. H.; Peltonen, L. J.; Linder, M. B.; Hirvonen, J. T.; Laaksonen, T. J., Multifunctional Hydrophobin: Toward Functional Coatings for Drug Nanoparticles. *ACS Nano* **2010,** *4* (3), 1750-1758.

83.   Haas Jimoh Akanbi, M.; Post, E.; Meter-Arkema, A.; Rink, R.; Robillard, G. T.; Wang, X.; Wösten, H. A. B.; Scholtmeijer, K., Use of hydrophobins in formulation of water insoluble drugs for oral administration. *Colloids Surf. B. Biointerfaces* **2010,** *75* (2), 526-531.

84.   Sarparanta, M.; Bimbo, L. M.; Rytkönen, J.; Mäkilä, E.; Laaksonen, T. J.; Laaksonen, P.; Nyman, M.; Salonen, J.; Linder, M. B.; Hirvonen, J.; Santos, H. A.; Airaksinen, A. J., Intravenous Delivery of Hydrophobin-Functionalized Porous Silicon Nanoparticles: Stability, Plasma Protein Adsorption and Biodistribution. *Mol. Pharm.* **2012,** *9* (3), 654-663.

85.   Richards, W. C.; Takai, S., Novel Technique for Isolating Microstructures Present in Shake Cultures of the Fungus Ceratocystis ulmi. *Applied Microbiology* **1973,** *26* (3), 443-444.

86.   Takai, S.; Richards, W. C., Cerato-ulmin, a Wilting Toxin of Ceratocystis ulmi: Isolation and some Properties of Cerato-ulmin from the Culture of C. ulmi. *J. Phytopathol.* **1978,** *91* (2), 129-146.

87.   Stevenson, K. J.; Slater, J. A.; Takai, S., Cerato-ulmin—a wilting toxin of Dutch elm disease fungus. *Phytochemistry* **1979,** *18* (2), 235-238.

88.   Takai, S.; Richards, W. C.; Stevenson, K. J., Evidence for the involvement of cerato-ulmin, the Ceratocystis ulmi toxin, in the development of Dutch elm disease. *Physiol. Plant Pathol.* **1983,** *23* (2), 275-280.

89.   Richards, W. C.; Takai, S., Characterization of the toxicity of cerato-ulmin, the toxin of Dutch elm disease. *Canadian Journal of Plant Pathology* **1984,** *6* (4), 291-298.

90.   Richards, W. C.; Takai, S., Production of cerato-ulmin in white elm following artificial inoculation with Ceratocystis ulmi. *Physiol. Mol. Plant Pathol.* **1988,** *33* (2), 279-285.

91.   Yaguchi, M.; Pusztai-Carey, M.; Roy, C.; Surewicz, W. K.; Carey, P. R.; Stevenson, K. J.; Richards, W. C.; Takai, S., Amino Acid Sequence and Spectroscopic Studies of Dutch Elm Disease Toxin, Cerato-ulmin. In *Dutch Elm Disease Research*, Sticklen, M.; Sherald, J., Eds. Springer New York: 1993; pp 152-170.

92.   Temple, B.; Horgen, P. A.; Bernier, L.; Hintz, W. E., Cerato-ulmin, a Hydrophobin Secreted by the Causal Agents of Dutch Elm Disease, Is a Parasitic Fitness Factor. *Fungal Genet. Biol.* **1997,** *22* (1), 39-53.

93.   Temple, B.; Horgen, P. A., Biological Roles for Cerato-Ulmin, a Hydrophobin Secreted by the Elm Pathogens, Ophiostoma ulmi and O. novo-ulmi. *Mycologia* **2000,** *92* (1), 1-9.

94.   Takai, S., Relationship of the production of the toxin, cerato-ulmin, to synnemata formation, pathogenicity, mycelial habit, and growth of Ceratocystis ulmi isolates. *Can. J. Bot.* **1980,** *58* (6), 658-662.

95.   Murray, B. S., Stabilization of bubbles and foams. *Curr. Opin. Colloid Interface Sci.* **2007,** *12* (4–5), 232-241.

96.   Cooper, A.; Kennedy, M. W., Biofoams and natural protein surfactants. *Biophys. Chem.* **2010,** *151* (3), 96-104.

97.   Hoffmann, H.; Reger, M., Emulsions with unique properties from proteins as emulsifiers. *Adv. Colloid Interface Sci.* **2013**.

98.   Lugones, L. G.; Bosscher, J. S.; Scholtmeyer, K.; de Vries, O. M. H.; Wessels, J. G. H., An abundant hydrophobin (ABH1) forms hydrophobic rodlet layers in Agaricus bisporus fruiting bodies. *Microbiology* **1996,** *142* (5), 1321-1329.

99.   Bantchev, G. B.; Russo, P. S.; McCarley, R. L.; Hammer, R. P., Simple multiangle, multicorrelator depolarized dynamic light scattering apparatus. *Rev. Sci. Instrum.* **2006,** *77* (4), 043902.

100.   Kaufman, G.; Liu, W.; Williams, D. M.; Choo, Y.; Gopinadhan, M.; Samudrala, N.; Sarfati, R.; Yan, E. C. Y.; Regan, L.; Osuji, C. O., Flat Drops, Elastic Sheets, and Microcapsules by Interfacial Assembly of a Bacterial Biofilm Protein, BslA. *Langmuir* **2017,** *33* (47), 13590-13597.

101.   Yamasaki, R.; Takatsuji, Y.; Asakawa, H.; Fukuma, T.; Haruyama, T., Flattened-Top Domical Water Drops Formed through Self-Organization of Hydrophobin Membranes: A Structural and Mechanistic Study Using Atomic Force Microscopy. *ACS Nano* **2016,** *10* (1), 81-87.

102.   Kirby, S. M.; Zhang, X.; Russo, P. S.; Anna, S. L.; Walker, L. M., Formation of a Rigid Hydrophobin Film and Disruption by an Anionic Surfactant at an Air/Water Interface. *Langmuir* **2016,** *32* (22), 5542-5551.

103.   Deckers, S. M.; Gebruers, K.; Baggerman, G.; Lorgouilloux, Y.; Delcour, J. A.; Michiels, C.; Derdelinckx, G.; Martens, J.; Neven, H., CO_2-hydrophobin structures acting as nanobombs in beer. *BrewingScience* **2010,** *63* (3-4), 54-61.

104.   Deckers, S. M.; Venken, T.; Khalesi, M.; Gebruers, K.; Baggerman, G.; Lorgouilloux, Y.; Shokribousjein, Z.; Ilberg, V.; Schönberger, C.; Titze, J.; Verachtert, H.; Michiels, C.; Neven, H.; Delcour, J.; Martens, J.; Derdelinckx, G.; De Maeyer, M., Combined modeling and biophysical characterisation of co2 interaction with class ii hydrophobins: New insight into the mechanism underpinning primary gushing. *J. Am. Soc. Brew. Chem.* **2012,** *70* (4), 249-256.

105.   Deckers, S. M.; Lorgouilloux, Y.; BAGGERMAN, G.; NEVEN, H.; MICHIELS, C.; DERDELINCKX, G.; DELCOUR, J. A.; MARTENS, J., Dynamic light scattering (DLS) as a tool to detect CO2-hydrophobin structures and study the primary gushing potential of beer. *J. Am. Soc. Brew. Chem.* **2011,** *69* (3), 144-149.

106.   Boys, C. V., *Soap Bubbles, Their Colours and the Forces which Mould Them*. Dover Publication: New York, 1958.

107.   Lindner, J. R., Microbubbles in medical imaging: current applications and future directions. *Nat. Rev. Drug Discov.* **2004,** *3* (6), 527-533.

108.   Teh, S.-Y.; Lin, R.; Hung, L.-H.; Lee, A. P., Droplet microfluidics. *Lab on a Chip* **2008,** *8* (2), 198-220.

109.   Bala Subramaniam, A.; Abkarian, M.; Mahadevan, L.; Stone, H. A., Colloid science: Non-spherical bubbles. *Nature* **2005,** *438* (7070), 930-930.

110.   Cui, M.; Emrick, T.; Russell, T. P., Stabilizing Liquid Drops in Nonequilibrium Shapes by the Interfacial Jamming of Nanoparticles. *Science* **2013,** *342* (6157), 460.

111.   Pairam, E.; Fernández-Nieves, A., Generation and stability of toroidal droplets in a viscous liquid. *Phys. Rev. Lett.* **2009,** *102* (23), 234501.

112.   An, D.; Warning, A.; Yancey, K. G.; Chang, C.-T.; Kern, V. R.; Datta, A. K.; Steen, P. H.; Luo, D.; Ma, M., Mass production of shaped particles through vortex ring freezing. *Nature Communications* **2016,** *7*, 12401.

113.   Bloomfield, V. A., DNA condensation. *Curr. Opin. Struct. Biol.* **1996,** *6* (3), 334-341.

114.   Bloomfield, V. A., DNA condensation by multivalent cations. *Biopolymers* **1997,** *44* (3), 269-282.

115.   Pochan, D. J.; Chen, Z.; Cui, H.; Hales, K.; Qi, K.; Wooley, K. L., Toroidal Triblock Copolymer Assemblies. *Science* **2004,** *306* (5693), 94-97.

116.   Chen, Z.; Cui, H.; Hales, K.; Li, Z.; Qi, K.; Pochan, D. J.; Wooley, K. L., Unique Toroidal Morphology from Composition and Sequence Control of Triblock Copolymers. *J. Am. Chem. Soc.* **2005,** *127* (24), 8592-8593.

117.   Cui, H.; Chen, Z.; Wooley, K. L.; Pochan, D. J., Origins of toroidal micelle formation through charged triblock copolymer self-assembly. *Soft Matter* **2009,** *5* (6), 1269-1278.

118.   Johnson, B. D.; Cooke, R. C., Generation of Stabilized Microbubbles in Seawater. *Science* **1981,** *213* (4504), 209-211.

119.   Tchuenbou-Magaia, F. L.; Norton, I. T.; Cox, P. W., Hydrophobins stabilised air-filled emulsions for the food industry. *Food Hydrocoll* **2009,** *23* (7), 1877-1885.

120.   Kirby, S. M.; Anna, S. L.; Walker, L. M., Sequential Adsorption of an Irreversibly Adsorbed Nonionic Surfactant and an Anionic Surfactant at an Oil/Aqueous Interface. *Langmuir* **2015,** *31* (14), 4063-4071.

121.   Alexandrov, N. A.; Marinova, K. G.; Gurkov, T. D.; Danov, K. D.; Kralchevsky, P. A.; Stoyanov, S. D.; Blijdenstein, T. B. J.; Arnaudov, L. N.; Pelan, E. G.; Lips, A.,

Interfacial layers from the protein HFBII hydrophobin: Dynamic surface tension, dilatational elasticity and relaxation times. *J. Colloid Interface Sci.* **2012,** *376* (1), 296-306.

122.   Blijdenstein, T. B. J.; de Groot, P. W. N.; Stoyanov, S. D., On the link between foam coarsening and surface rheology: why hydrophobins are so different. *Soft Matter* **2010,** *6* (8), 1799-1808.

123.   Lim, K. Y.; Quinto-Su, P. A.; Klaseboer, E.; Khoo, B. C.; Venugopalan, V.; Ohl, C.-D., Nonspherical laser-induced cavitation bubbles. *Phys. Rev. E* **2010,** *81* (1), 016308.

124.   Chen, J.; Zhang, H.-C.; Shen, Z.-H.; Lu, J.; Ni, X.-W., Formation and dynamics of a toroidal bubble during laser propelling a cavity object in water. *Opt. Lett.* **2013,** *38* (19), 3803-3806.

125.   Walters, J. K.; Davidson, J. F., The initial motion of a gas bubble formed in an inviscid liquid. *J. Fluid Mech.* **1963,** *17* (3), 321-336.

126.   Pedley, T. J., The toroidal bubble. *J. Fluid Mech.* **1968,** *32* (1), 97-112.

127.   Russo, P. S.; Blum, F. D.; Ipsen, J. D.; Abulhajj, Y. J.; Miller, W. G., The Surface-Activity of the Phytotoxin Cerato-Ulmin. *Can. J. Bot.* **1982,** *60* (8), 1414-1422.

128.   Zhang, X. L.; Penfold, J.; Thomas, R. K.; Tucker, I. M.; Petkov, J. T.; Bent, J.; Cox, A.; Campbell, R. A., Adsorption Behavior of Hydrophobin and Hydrophobin/Surfactant Mixtures at the Air–Water Interface. *Langmuir* **2011,** *27* (18), 11316-11323.

129.   Stanimirova, R. D.; Gurkov, T. D.; Kralchevsky, P. A.; Balashev, K. T.; Stoyanov, S. D.; Pelan, E. G., Surface Pressure and Elasticity of Hydrophobin HFBII Layers on the Air–Water Interface: Rheology Versus Structure Detected by AFM Imaging. *Langmuir* **2013,** *29* (20), 6053-6067.

130.   Yin, W.-L., Non-uniform inflation of a cylindrical elastic membrane and direct determination of the strain energy function. *Journal of Elasticity* **1977,** *7* (3), 265-282.

131.   Prabhudesai, G.; Bihi, I.; Zoueshtiagh, F.; Jose, J.; Baudoin, M., Nonspherical armoured bubble vibration. *Soft Matter* **2017,** *13* (21), 3879-3884.

132.   Käs, J.; Sackmann, E., Shape transitions and shape stability of giant phospholipid vesicles in pure water induced by area-to-volume changes. *Biophys. J.* **1991,** *60* (4), 825-844.

133.   Deuling, H. J.; Helfrich, W., Red blood cell shapes as explained on the basis of curvature elasticity. *Biophys. J.* **1976,** *16* (8), 861-868.

134.   Lipowsky, R., The conformation of membranes. *Nature* **1991,** *349*, 475.

135.   Angelov, B.; Mladenov, I., *On the Geometry of Red Blood Cell*. Coral Press: Sofia, 2000; Vol. 1, p 27-46.

136.   Jülicher, F.; Seifert, U.; Lipowsky, R., Conformal degeneracy and conformal diffusion of vesicles. *Phys. Rev. Lett.* **1993,** *71* (3), 452-455.

137.   Canham, P. B., The minimum energy of bending as a possible explanation of the biconcave shape of the human red blood cell. *J. Theor. Biol.* **1970,** *26* (1), 61-81.

138.   Helfrich, W., Elastic Properties of Lipid Bilayers: Theory and Possible Experiments. In *Zeitschrift für Naturforschung C*, 1973; Vol. 28, p 693.

139.   Sackmann, E., Membrane bending energy concept of vesicle- and cell-shapes and shape-transitions. *FEBS Lett.* **1994,** *346* (1), 3-16.

140.   Evans, E. A., Bending Resistance and Chemically Induced Moments in Membrane Bilayers. *Biophys. J.* **1974,** *14* (12), 923-931.

141.   Rand, R. P., Mechanical Properties of the Red Cell Membrane: II. Viscoelastic Breakdown of the Membrane. *Biophys. J.* **1964,** *4* (4), 303-316.

142.   Rand, R. P.; Burton, A. C., Mechanical Properties of the Red Cell Membrane: I. Membrane Stiffness and Intracellular Pressure. *Biophys. J.* **1964,** *4* (2), 115-135.

143.   Mutz, M.; Bensimon, D., Observation of toroidal vesicles. *Phys. Rev. A* **1991,** *43* (8), 4525-4527.

144.   Ou-Yang, Z.-c., Anchor ring-vesicle membranes. *Phys. Rev. A* **1990,** *41* (8), 4517-4520.

145.   Seifert, U., Vesicles of toroidal topology. *Phys. Rev. Lett.* **1991,** *66* (18), 2404-2407.

146.   Fourcade, B.; Mutz, M.; Bensimon, D., Experimental and theoretical-study of toroidal vesicles. *Phys. Rev. Lett.* **1992,** *68* (16), 2551-2554.

147.   Jülicher, F.; Seifert, U.; Lipowsky, R., Phase diagrams and shape transformations of toroidal vesicles. *J. Phys. II France* **1993,** *3* (11), 1681-1705.

148.   Michalet, X.; Bensimon, D., Vesicles of Toroidal Topology: Observed Morphology and Shape Transformations. *J. Phys. II France* **1995,** *5* (2), 263-287.

149.   Pairam, E.; Vallamkondu, J.; Koning, V.; van Zuiden, B. C.; Ellis, P. W.; Bates, M. A.; Vitelli, V.; Fernandez-Nieves, A., Stable nematic droplets with handles. *Proceedings of the National Academy of Sciences* **2013,** *110* (23), 9295-9300.

150.   Pairam, E.; Le, H.; Fernández-Nieves, A., Stability of toroidal droplets inside yield stress materials. *Phys. Rev. E* **2014,** *90* (2), 021002.

151.   Zhong-can, O.-Y., Selection of toroidal shape of partially polymerized membranes. *Phys. Rev. E* **1993,** *47* (1), 747-749.

152.	Yuan, F.; Zhang, X.; Yang, M.; Wang, W.; Minch, B.; Lieser, G.; Wegner, G., Topological transformation of aggregates formed by an amphiphilic and truncated-cone-shaped codendrimer. *Soft Matter* **2007,** *3* (11), 1372-1376.

153.	Michalet, X.; Bensimon, D.; Fourcade, B., Fluctuating vesicles of nonspherical topology. *Phys. Rev. Lett.* **1994,** *72* (1), 168-171.

154.	Cardiel, J. J.; Tonggu, L.; Dohnalkova, A. C.; de la Iglesia, P.; Pozzo, D. C.; Wang, L.; Shen, A. Q., Worming Their Way into Shape: Toroidal Formations in Micellar Solutions. *ACS Nano* **2013,** *7* (11), 9704-9713.

155.	Noguchi, H., Construction of Nuclear Envelope Shape by a High-Genus Vesicle with Pore-Size Constraint. *Biophys. J.* **2016,** *111* (4), 824-831.

156.	Chen, L.; Jiang, T.; Lin, J.; Cai, C., Toroid Formation through Self-Assembly of Graft Copolymer and Homopolymer Mixtures: Experimental Studies and Dissipative Particle Dynamics Simulations. *Langmuir* **2013,** *29* (26), 8417-8426.

157.	Noguchi, H., Fusion and toroidal formation of vesicles by mechanical forces: A Brownian dynamics simulation. *J Chem Phys* **2002,** *117* (17), 8130-8137.

158.	Walther, A.; Muller, A. H. E., Janus particles. *Soft Matter* **2008,** *4* (4), 663-668.

159.	Walther, A.; Müller, A. H. E., Janus Particles: Synthesis, Self-Assembly, Physical Properties, and Applications. *Chem. Rev.* **2013,** *113* (7), 5194-5261.

160.	Kam, S. I.; Rossen, W. R., Anomalous Capillary Pressure, Stress, and Stability of Solids-Coated Bubbles. *J. Colloid Interface Sci.* **1999,** *213* (2), 329-339.

161.	A. Bos, M.; van Vliet, T., Interfacial rheological properties of adsorbed protein layers and surfactants: a review. *Adv. Colloid Interface Sci.* **2001,** *91* (3), 437-471.

162.	Wilde, P.; Mackie, A.; Husband, F.; Gunning, P.; Morris, V., Proteins and emulsifiers at liquid interfaces. *Adv. Colloid Interface Sci.* **2004,** *108–109* (0), 63-71.

163.	de Jongh, H. H. J.; Kosters, H. A.; Kudryashova, E.; Meinders, M. B. J.; Trofimova, D.; Wierenga, P. A., Protein adsorption at air–water interfaces: A combination of details. *Biopolymers* **2004,** *74* (1-2), 131-135.

164.	Zhai, J. l.; Day, L.; Aguilar, M.-I.; Wooster, T. J., Protein folding at emulsion oil/water interfaces. *Curr. Opin. Colloid Interface Sci.* **2013,** *18* (4), 257-271.

165.	Day, L.; Zhai, J.; Xu, M.; Jones, N. C.; Hoffmann, S. V.; Wooster, T. J., Conformational changes of globular proteins adsorbed at oil-in-water emulsion interfaces examined by Synchrotron Radiation Circular Dichroism. *Food Hydrocoll* **2014,** *34* (Supplement C), 78-87.

166.   Beverung, C. J.; Radke, C. J.; Blanch, H. W., Protein adsorption at the oil/water interface: characterization of adsorption kinetics by dynamic interfacial tension measurements. *Biophys. Chem.* **1999,** *81* (1), 59-80.

167.   Kisko, K.; Szilvay, G. z. R.; Vuorimaa, E.; Lemmetyinen, H.; Linder, M. B.; Torkkeli, M.; Serimaa, R., Self-Assembled Films of Hydrophobin Proteins HFBI and HFBII Studied in Situ at the Air/Water Interface. *Langmuir* **2008,** *25* (3), 1612-1619.

168.   Aumaitre, E.; Vella, D.; Cicuta, P., On the measurement of the surface pressure in Langmuir films with finite shear elasticity. *Soft Matter* **2011,** *7* (6), 2530-2537.

169.   Ravera, F.; Loglio, G.; Kovalchuk, V. I., Interfacial dilational rheology by oscillating bubble/drop methods. *Curr. Opin. Colloid Interface Sci.* **2010,** *15* (4), 217-228.

170.   Karbaschi, M.; Lotfi, M.; Krägel, J.; Javadi, A.; Bastani, D.; Miller, R., Rheology of interfacial layers. *Curr. Opin. Colloid Interface Sci.* **2014,** *19* (6), 514-519.

171.   Hard, S.; Neuman, R. D., Laser light-scattering measurements of viscoelastic monomolecular films. *J. Colloid Interface Sci.* **1981,** *83* (2), 315-334.

172.   Kisko, K.; Torkkeli, M.; Vuorimaa, E.; Lemmetyinen, H.; Seeck, O. H.; Linder, M.; Serimaa, R., Langmuir–Blodgett films of hydrophobins HFBI and HFBII. *Surf. Sci.* **2005,** *584* (1), 35-40.

173.   Lumsdon, S. O.; Green, J.; Stieglitz, B., Adsorption of hydrophobin proteins at hydrophobic and hydrophilic interfaces. *Colloids Surf. B. Biointerfaces* **2005,** *44* (4), 172-178.

174.   Szilvay, G. R.; Kisko, K.; Serimaa, R.; Linder, M. B., The relation between solution association and surface activity of the hydrophobin HFBI from Trichoderma reesei. *FEBS Lett.* **2007,** *581* (14), 2721-2726.

175.   Mackie, A. R.; Gunning, A. P.; Ridout, M. J.; Wilde, P. J.; Morris, V. J., Orogenic Displacement in Mixed β-Lactoglobulin/β-Casein Films at the Air/Water Interface. *Langmuir* **2001,** *17* (21), 6593-6598.

176.   Szilvay, G. R.; Paananen, A.; Laurikainen, K.; Vuorimaa, E.; Lemmetyinen, H.; Peltonen, J.; Linder, M. B., Self-Assembled Hydrophobin Protein Films at the Air−Water Interface: Structural Analysis and Molecular Engineering†. *Biochemistry* **2007,** *46* (9), 2345-2354.

177.   Knoche, S.; Vella, D.; Aumaitre, E.; Degen, P.; Rehage, H.; Cicuta, P.; Kierfeld, J., Elastometry of Deflated Capsules: Elastic Moduli from Shape and Wrinkle Analysis. *Langmuir* **2013,** *29* (40), 12463-12471.

178.   Aumaitre, E.; Wongsuwarn, S.; Rossetti, D.; Hedges, N. D.; Cox, A. R.; Vella, D.; Cicuta, P., A viscoelastic regime in dilute hydrophobin monolayers. *Soft Matter* **2012,** *8* (4), 1175-1183.

179.	Aumaitre, E.; Knoche, S.; Cicuta, P.; Vella, D., Wrinkling in the deflation of elastic bubbles. *The European Physical Journal E* **2013,** *36* (3), 1-5.

180.	Radulova, G. M.; Danov, K. D.; Kralchevsky, P. A.; Petkov, J. T.; Stoyanov, S. D., Shear rheology of hydrophobin adsorption layers at oil/water interfaces and data interpretation in terms of a viscoelastic thixotropic model. *Soft Matter* **2014,** *10* (31), 5777-5786.

181.	Richter, M. J.; Schulz, A.; Subkowski, T.; Böker, A., Adsorption and rheological behavior of an amphiphilic protein at oil/water interfaces. *J. Colloid Interface Sci.* **2016,** *479*, 199-206.

182.	Radulova, G. M.; Golemanov, K.; Danov, K. D.; Kralchevsky, P. A.; Stoyanov, S. D.; Arnaudov, L. N.; Blijdenstein, T. B. J.; Pelan, E. G.; Lips, A., Surface Shear Rheology of Adsorption Layers from the Protein HFBII Hydrophobin: Effect of Added β-Casein. *Langmuir* **2012,** *28* (9), 4168-4177.

183.	Blijdenstein, T. B. J.; Ganzevles, R. A.; de Groot, P. W. N.; Stoyanov, S. D., On the link between surface rheology and foam disproportionation in mixed hydrophobin HFBII and whey protein systems. *Colloids Surf. Physicochem. Eng. Aspects* **2013,** *438* (0), 13-20.

184.	Alvarez, N. J.; Walker, L. M.; Anna, S. L., A Microtensiometer To Probe the Effect of Radius of Curvature on Surfactant Transport to a Spherical Interface. *Langmuir* **2010,** *26* (16), 13310-13319.

185.	Alvarez, N. J.; Walker, L. M.; Anna, S. L., Diffusion-limited adsorption to a spherical geometry: The impact of curvature and competitive time scales. *Phys. Rev. E* **2010,** *82* (1), 011604.

186.	Reichert, M. D.; Alvarez, N. J.; Brooks, C. F.; Grillet, A. M.; Mondy, L. A.; Anna, S. L.; Walker, L. M., The importance of experimental design on measurement of dynamic interfacial tension and interfacial rheology in diffusion-limited surfactant systems. *Colloids Surf. Physicochem. Eng. Aspects* **2015,** *467*, 135-142.

187.	Alvarez, N. J.; Vogus, D. R.; Walker, L. M.; Anna, S. L., Using bulk convection in a microtensiometer to approach kinetic-limited surfactant dynamics at fluid–fluid interfaces. *J. Colloid Interface Sci.* **2012,** *372* (1), 183-191.

188.	Reichert, M. D.; Walker, L. M., Interfacial Tension Dynamics, Interfacial Mechanics, and Response to Rapid Dilution of Bulk Surfactant of a Model Oil–Water-Dispersant System. *Langmuir* **2013,** *29* (6), 1857-1867.

189.	Reichert, M. D.; Walker, L. M., Coalescence behavior of oil droplets coated in irreversibly-adsorbed surfactant layers. *J. Colloid Interface Sci.* **2015,** *449*, 480-487.

190.   Alvarez, N. J.; Anna, S. L.; Saigal, T.; Tilton, R. D.; Walker, L. M., Interfacial Dynamics and Rheology of Polymer-Grafted Nanoparticles at Air–Water and Xylene–Water Interfaces. *Langmuir* **2012,** *28* (21), 8052-8063.

191.   Manga, M. S.; Hunter, T. N.; Cayre, O. J.; York, D. W.; Reichert, M. D.; Anna, S. L.; Walker, L. M.; Williams, R. A.; Biggs, S. R., Measurements of Submicron Particle Adsorption and Particle Film Elasticity at Oil–Water Interfaces. *Langmuir* **2016,** *32* (17), 4125-4133.

192.   Kirby, S. M.; Anna, S. L.; Walker, L. M., Effect of surfactant tail length and ionic strength on the interfacial properties of nanoparticle-surfactant complexes. *Soft Matter* **2018,** *14* (1), 112-123.

193.   Rosu, C.; Kleinhenz, N.; Choi, D.; Tassone, C. J.; Zhang, X.; Park, J. O.; Srinivasarao, M.; Russo, P. S.; Reichmanis, E., Protein-Assisted Assembly of π-Conjugated Polymers. *Chem. Mater.* **2016,** *28* (2), 573-582.

194.   Kotula, A. P.; Anna, S. L., Regular perturbation analysis of small amplitude oscillatory dilatation of an interface in a capillary pressure tensiometer. *J. Rheol.* **2015,** *59* (1), 85-117.

195.   Cheung, D. L., Molecular Simulation of Hydrophobin Adsorption at an Oil–Water Interface. *Langmuir* **2012,** *28* (23), 8730-8736.

196.   Lee, S.; Ron, T.; Pakkanen, K. I.; Linder, M., Hydrophobins as aqueous lubricant additive for a soft sliding contact. *Colloids Surf. B. Biointerfaces* **2015,** *125* (0), 264-9.

197.   Morris, V. K.; Ren, Q.; Macindoe, I.; Kwan, A. H.; Byrne, N.; Sunde, M., Recruitment of Class I Hydrophobins to the Air:Water Interface Initiates a Multi-step Process of Functional Amyloid Formation. *J. Biol. Chem.* **2011,** *286* (18), 15955-15963.

198.   Chandler, D., Interfaces and the driving force of hydrophobic assembly. *Nature* **2005,** *437* (7059), 640-647.

199.   Knoche, S.; Kierfeld, J., Elasticity of Interfacial Rafts of Hard Particles with Soft Shells. *Langmuir* **2015,** *31* (19), 5364-5376.

200.   Tucker, I. M.; Petkov, J. T.; Penfold, J.; Thomas, R. K.; Li, P.; Cox, A. R.; Hedges, N.; Webster, J. R. P., Spontaneous Surface Self-Assembly in Protein–Surfactant Mixtures: Interactions between Hydrophobin and Ethoxylated Polysorbate Surfactants. *The Journal of Physical Chemistry B* **2014,** *118* (18), 4867-4875.

201.   Wang, Z.; Morales-Acosta, M. D.; Li, S.; Liu, W.; Kanai, T.; Liu, Y.; Chen, Y.-N.; Walker, F. J.; Ahn, C. H.; Leblanc, R. M.; Yan, E. C. Y., A narrow amide I vibrational band observed by sum frequency generation spectroscopy reveals highly ordered structures of a biofilm protein at the air/water interface. *Chem. Commun.* **2016,** *52* (14), 2956-2959.

202.   Meister, K.; Bäumer, A.; Szilvay, G. R.; Paananen, A.; Bakker, H. J., Self-Assembly and Conformational Changes of Hydrophobin Classes at the Air–Water Interface. *The Journal of Physical Chemistry Letters* **2016,** *7*, 4067-4071.

203.   Milani, R.; Monogioudi, E.; Baldrighi, M.; Cavallo, G.; Arima, V.; Marra, L.; Zizzari, A.; Rinaldi, R.; Linder, M.; Resnati, G.; Metrangolo, P., Hydrophobin: fluorosurfactant-like properties without fluorine. *Soft Matter* **2013,** *9* (28), 6505.

204.   Lienemann, M.; Grunér, M. S.; Paananen, A.; Siika-aho, M.; Linder, M. B., Charge-Based Engineering of Hydrophobin HFBI: Effect on Interfacial Assembly and Interactions. *Biomacromolecules* **2015,** *16* (4), 1283-1292.

205.   Zhang, X.; Kirby, S. M.; Chen, Y.; Anna, S. L.; Walker, L. M.; Hung, F. R.; Russo, P. S., Formation and elasticity of membranes of the class II hydrophobin Cerato-ulmin at oil-water interfaces. *Colloids Surf. B. Biointerfaces* **2018,** *164*, 98-106.

206.   Chow, E.; Skolnick, J., Effects of confinement on models of intracellular macromolecular dynamics. *Proceedings of the National Academy of Sciences* **2015,** *112* (48), 14846-14851.

207.   Graham, M. D., Fluid Dynamics of Dissolved Polymer Molecules in Confined Geometries. *Annual Review of Fluid Mechanics* **2011,** *43* (1), 273-298.

208.   Al-Obaidi, H.; Florence, A. T., Nanoparticle delivery and particle diffusion in confined and complex environments. *J. Drug Deliv. Sci. Technol.* **2015,** *30, Part B*, 266-277.

209.   Brown, R., XXVII. A brief account of microscopical observations made in the months of June, July and August 1827, on the particles contained in the pollen of plants; and on the general existence of active molecules in organic and inorganic bodies. *Philosophical Magazine Series 2* **1828,** *4* (21), 161-173.

210.   Einstein, A., Über die von der molekularkinetischen Theorie der Wärme geforderte Bewegung von in ruhenden Flüssigkeiten suspendierten Teilchen. *Annalen der Physik* **1905,** *322* (8), 549-560.

211.   Cerbino, R.; Trappe, V., Differential Dynamic Microscopy: Probing Wave Vector Dependent Dynamics with a Microscope. *Phys. Rev. Lett.* **2008,** *100* (18), 188102.

212.   Giavazzi, F.; Cerbino, R., Digital Fourier microscopy for soft matter dynamics. *J. Opt.* **2014,** *16* (8).

213.   Ferri, F.; D'Angelo, A.; Lee, M.; Lotti, A.; Pigazzini, M. C.; Singh, K.; Cerbino, R., Kinetics of colloidal fractal aggregation by differential dynamic microscopy. *Eur Phys J Spec Top* **2011,** *199* (1), 139-148.

214.   Wilson, L. G.; Martinez, V. A.; Schwarz-Linek, J.; Tailleur, J.; Bryant, G.; Pusey, P. N.; Poon, W. C. K., Differential Dynamic Microscopy of Bacterial Motility. *Phys. Rev. Lett.* **2011,** *106* (1).

215.   Martinez, V. A.; Besseling, R.; Croze, O. A.; Tailleur, J.; Reufer, M.; Schwarz-Linek, J.; Wilson, L. G.; Bees, M. A.; Poon, W. C. K., Differential Dynamic Microscopy: A High-Throughput Method for Characterizing the Motility of Microorganisms. *Biophys. J.* **2012,** *103* (8), 1637-1647.

216.   He, K.; Spannuth, M.; Conrad, J. C.; Krishnamoorti, R., Diffusive dynamics of nanoparticles in aqueous dispersions. *Soft Matter* **2012,** *8* (47), 11933-11938.

217.   Lu, P. J.; Giavazzi, F.; Angelini, T. E.; Zaccarelli, E.; Jargstorff, F.; Schofield, A. B.; Wilking, J. N.; Romanowsky, M. B.; Weitz, D. A.; Cerbino, R., Characterizing Concentrated, Multiply Scattering, and Actively Driven Fluorescent Systems with Confocal Differential Dynamic Microscopy. *Phys. Rev. Lett.* **2012,** *108* (21).

218.   Giavazzi, F.; Crotti, S.; Speciale, A.; Serra, F.; Zanchetta, G.; Trappe, V.; Buscaglia, M.; Bellini, T.; Cerbino, R., Viscoelasticity of nematic liquid crystals at a glance. *Soft Matter* **2014,** *10* (22), 3938-3949.

219.   Reufer, M.; Martinez, V. A.; Schurtenberger, P.; Poon, W. C. K., Differential Dynamic Microscopy for Anisotropic Colloidal Dynamics. *Langmuir* **2012,** *28* (10), 4618-4624.

220.   Wittmeier, A.; Leeth Holterhoff, A.; Johnson, J.; Gibbs, J. G., Rotational Analysis of Spherical, Optically Anisotropic Janus Particles by Dynamic Microscopy. *Langmuir* **2015,** *31* (38), 10402-10410.

221.   Dienerowitz, M.; Lee, M.; Gibson, G.; Padgett, M., Measuring nanoparticle flow with the image structure function. *Lab on a Chip* **2013,** *13* (12), 2359-2363.

222.   Douglass, K. M.; Sparrow, N. A.; Bott, M.; Fernandez-Valle, C.; Dogariu, A., Measuring anisotropic cell motility on curved substrates. *Journal of Biophotonics* **2013,** *6* (5), 387-392.

223.   He, K.; Babaye Khorasani, F.; Retterer, S. T.; Thomas, D. K.; Conrad, J. C.; Krishnamoorti, R., Diffusive Dynamics of Nanoparticles in Arrays of Nanoposts. *ACS Nano* **2013,** *7* (6), 5122-5130.

224.   He, K.; Retterer, S. T.; Srijanto, B. R.; Conrad, J. C.; Krishnamoorti, R., Transport and Dispersion of Nanoparticles in Periodic Nanopost Arrays. *ACS Nano* **2014,** *8* (5), 4221-4227.

225.   Jacob, J. D. C.; He, K.; Retterer, S. T.; Krishnamoorti, R.; Conrad, J. C., Diffusive dynamics of nanoparticles in ultra-confined media. *Soft Matter* **2015,** *11* (38), 7515-7524.

226.   Sentjabrskaja, T.; Zaccarelli, E.; De Michele, C.; Sciortino, F.; Tartaglia, P.; Voigtmann, T.; Egelhaaf, S. U.; Laurati, M., Anomalous dynamics of intruders in a crowded environment of mobile obstacles. *Nat Commun* **2016,** *7.*

227.   Hsu, M. F.; Nikolaides, M. G.; Dinsmore, A. D.; Bausch, A. R.; Gordon, V. D.; Chen, X.; Hutchinson, J. W.; Weitz, D. A.; Marquez, M., Self-assembled shells composed of colloidal particles: fabrication and characterization. *Langmuir* **2005,** *21* (7), 2963-2970.

228.   Cerbino, R.; Cicuta, P., Perspective: Differential dynamic microscopy extracts multi-scale activity in complex fluids and biological systems. *J Chem Phys* **2017,** *147* (11), 110901.

229.   Safari, M. S.; Poling-Skutvik, R.; Vekilov, P. G.; Conrad, J. C., Differential dynamic microscopy of bidisperse colloidal suspensions. *npj Microgravity* **2017,** *3* (1), 21.

230.   Germain, D.; Leocmach, M.; Gibaud, T., Differential dynamic microscopy to characterize Brownian motion and bacteria motility. *Am. J. Phys.* **2016,** *84* (3), 202-210.